Master's thesis

NTNU
Norwegian University of Science and Technology
Faculty of Engineering
Department of Civil and Environmental Engineering

Parasmani Tripathi

Design and Analysis of a Geosynthetically Reinforced Soil Bridge Abutment

Static and Seismic Approach

Master's thesis in Geotechnics and Geohazards
Supervisor: Professor Gudmund Reidar Eiksund
January 2020

NTNU
Norwegian University of Science and Technology

Parasmani Tripathi

Design and Analysis of a Geosynthetically Reinforced Soil Bridge Abutment

Static and Seismic Approach

Trondheim, January 29, 2020

MASTER'S THESIS: TBA4900

Main supervisor: Professor Gudmund Reidar Eiksund (NTNU)

Co-supervisor: Arnstein Watn (NTNU)

Department of Civil and Environmental Engineering

Norwegian University of Science and Technology, NTNU

NTNU – Trondheim
Norwegian University of
Science and Technology

Preface

This Master's thesis was conducted as a part of MSc. in Geotechnics and Geohazards at the Department of Civil and Environmental Engineering, at the Norwegian University of Science and Technology (NTNU) during the fall semester of 2019. The thesis involves design and analysis for static and seismic conditions of a geosynthetically reinforced soil bridge abutment. The topic is an outcome of suggestion of my main supervisor Professor Gudmund Reidar Eiksund.

Trondheim, 2020-01-29

Parasmani Tripathi

Acknowledgment

I would like to take this opportunity to express my sincere gratitude towards my supervisors Professor Gudmund Reidar Eiksund and Arnstein Watn, Department of Civil and Environmental Engineering at NTNU for their continuous guidance, support and valuable suggestions throughout the thesis. I also would like to thank everyone at the geotechnical division, NTNU for all the help and motivation during the entire duration.

I am most thankful to all known and unknown helping hands and minds that guided me through the thesis.

Parasmani Tripathi

Trondheim, 29 January 2020

Abstract

Reinforced soil bridge abutments are a combination of compacted soil and reinforcements (in this case geosynthetics), which supports and distributes the loads from the bridge superstructure. The structure works on the principle of development of strength from induced strain in the reinforcements during compaction and pre-loading. The design and analysis of the abutment in this thesis is assumed for soil conditions of Skedsmo, Oslo. The design and analysis is performed for static and dynamic conditions.

The thesis conducts a limit state design for calculating the dimensions of a reinforced soil bridge abutment with spread footing at the top. It obtains dimensions and details for the components involved in the bridge abutment. It is also determined in this portion, that the most critical failure mode for external stability of the abutment is eccentricity in overturning, and mode of failure for internal stability is pullout failure of the reinforcements.

A static finite element analysis is then performed for the designed bridge abutment and shortcomings of the limit state design are identified and rectified with a modified design involving additional geogrids behind the spread footing. Critical failure modes according to the limit state design are also verified in this portion.

The thesis then conducts an analytical seismic analysis for evaluating and comparing static and dynamic loads upon the bridge abutment. It is found that the reinforced soil bridge abutment works within safety requirements for the considered simplified loading conditions and applied vibration.

The thesis then conducts a dynamic finite element analysis for a simplified model. First a sinusoidal harmonic wave of varying amplitudes (0.05g, 0.1g and 0.5g peak amplitudes) is applied to a simplified model, for determining the right boundary conditions for the analysis. A free field boundary resembling propagation of earthquake in real life is selected for the analysis. A real earthquake acceleration time history scaled to a 0.5g peak acceleration amplitude is then applied for the model - with and without geogrids, using a soil model that simulates reduction of shear modulus according to increasing shear strain. A significant reduction upon displacement in the abutment is observed with the use of reinforcements. Variation of resultant acceleration, displacements and dominant frequencies are analysed and it is found that the use of geogrids significantly improves the stability of the model under the applied earthquake vibration.

The thesis concludes with two main statements. First is that the reinforcements added in the

rectified limit state design has high significance in terms of stability, performance of connecting road, anchoring of the reinforced section with the backfill and on internal plastic deformation and friction mobilization behind the reinforced section. Second is that the use of geosynthetics significantly reduces displacement under seismic loads. Change of the resultant frequency ranges and dominant frequencies indicate a change in eigen-frequency of the system. The thesis concludes with the remark that this behaviour should be studied more closely with the perspective of change in shear wave velocity and eigen-frequency of the system with the use of geosynthetical reinforcements.

Sammendrag

Forsterkede jordbroforankringer er en kombinasjon av komprimert jord og forsterkninger (i dette tilfellet geosyntetikk), som støtter og fordeler belastningen fra brooverbygget. Strukturen fungerer etter prinsippet om å utvikle styrke fra indusert belastning i forsterkningene under komprimering og forbelastning. Utformingen og analysen av distansen i denne oppgaven er antatt for jordforholdene til Skedsmo, Oslo. Utformingen og analysen utføres for statiske og dynamiske forhold.

Oppgaven gjennomfører en grensetilstandsdesign for å beregne dimensjonene til en armert jordbroanlegg med spredt fotfeste i toppen. Den oppnår dimensjoner og detaljer for komponentene som er involvert i broanlegget. Det bestemmes også i denne delen at den mest kritiske feilmodus for ytre stabilitet av anlegget er eksentrisitet ved velting, og modus for svikt for indre stabilitet er uttrekkssvikt i forsterkningene.

En statisk endelig elementanalyse blir deretter utført for den konstruerte broavstanden og mangler ved grensetilstandens design blir identifisert og utbedret med en modifisert utforming som involverer ytterligere geogrider bak spredningsfoten. Kritiske feilmodus i henhold til grensetilstandens utforming er også verifisert i denne delen.

Avhandlingen gjennomfører deretter en analytisk seismisk analyse for å evaluere og sammenligne statiske og dynamiske belastninger på broanlegget. Det er funnet at det armerte jordbruet ligger innenfor sikkerhetskrav for de betraktede forenklede belastningsforhold og påført vibrasjon.

Oppgaven gjennomfører deretter en dynamisk endelig elementanalyse for en forenklet modell. Først blir en sinusformet harmonisk bølge av varierende amplituder (0,05 g, 0,1 g og 0,5 g toppamplituder) brukt til en forenklet modell for å bestemme de rette grensebetingelsene for analysen. En frie feltgrense som ligner forplantning av jordskjelv i det virkelige liv er valgt for analysen. Deretter brukes en ekte akselasjonstidshistorie for jordskjelv, skalert til en 0,5g topp akselerasjonsamplitude for modellen - med og uten geogrider, ved bruk av en jordmodell som simulerer reduksjon av skjærmodul i henhold til økende skjærbelastning. Ved bruk av forsterkninger observeres en betydelig reduksjon ved forskyvning i anlegget. Variasjon av resulterende akselerasjon, forskyvninger og dominerende frekvenser blir analysert, og det er funnet at bruk av geogrider betydelig forbedrer stabiliteten til modellen under den påførte jordskjelvvibrasjonen.

Oppgaven avsluttes med to hoveduttalelser. Det første er at forsterkningene som er lagt til i den utbedrede grensetilstandens utforming har stor betydning når det gjelder stabilitet, ytelse av forbindelsesvei, forankring av det forsterkede partiet med tilbakefyllingen og for innvendig plastisk deformasjon og friksjonsmobilisering bak den forsterkede seksjonen. Det andre er at bruk av geosyntetikk reduserer forskyvningen betydelig under seismiske belastninger. Endring av de resulterende frekvensområdene og dominerende frekvenser indikerer en endring i egenfrekvensen til systemet. Oppgaven avsluttes med bemerkningen om at denne atferden bør studeres nærmere med perspektivet på endring i skjærbølgehastighet og egenfrekvens av systemet ved bruk av geosyntetiske forsterkninger.

Contents

List of Symbols

Description of symbol unless otherwise stated for specific cases

α	Rayleigh damping parameter for mass influence
β	Rayleigh damping parameter for stiffness influence
γ_b	Unit weight of backfill soil
γ_r	Unit weight of reinforced soil section
$\gamma_{0.7}$	Shear strain at which $G_s = 0.72\ G_o$
ϕ	Angle of friction
ϕ_b	Friction angle for backfill soil
ϕ_r	Friction angle for reinforced soil section
ζ	Dampening ratio
a_{gR}	Reference peak ground acceleration
c	Cohesion
E_{50}^{ref}	Secant stiffness in standard drained triaxial test
E_{oed}^{ref}	Tangent stiffness for primary oedometer loading
E_{ur}^{ref}	Unloading / reloading stiffness
F_{pull}	Pullout resistance factor
g	Acceleration due to gravity
G_{max}	Maximum shear modulus

G_o^{ref}	Reference shear modulus at very small shear strains ($\epsilon < 10^{-6}$)
G_s	Secant shear modulus
K_a	Active lateral earth pressure coefficient
K_o	Lateral earth pressure coefficient at rest
K_p	Passive lateral earth pressure coefficient
K_r	Lateral stress coefficient for reinforcements
K_{AE}	Dynamic earth pressure coefficient
K_o^{nc}	K_o value for normal consolidation
P_{IR}	Pseudo-static inertial force
v_s	Shear wave velocity
v_{ur}	Poisson's ratio for unloading / reloading
m	Power for stress level dependency of stiffness

List of Drawings and Figures

List of Tables

Chapter 1

Introduction

.

1.1 Reinforced Soil and Geosynthetics

Soil as it exists in its natural conditions, can be seen held together by roots - which in turn can support an enormous weight of the tree. Soil can most confidently be termed as one of the oldest construction material available to mankind. It can also be reasonably assumed that attempts to stabilize swamps and marshes were made before attempts to first historical records were made. Historical documents suggest that, soil together with wood and straws were used in the earliest forms of wall and roof construction. As construction practices developed with the use of materials that were available locally, reinforced soil were seen to be used in many different ways - in different eras and regions.

The term reinforced soil indicates that certain tensile resisting material is being used along with the soil to increase its strength. Historical use of reinforced soil can be traced back to ancient civilizations, when naturally existing fibres were used along with compacted soil for creating a stronger composite construction material. Compacted soil reinforced with reed was used to construct habitats on the Iranian plateau since fifth millenium BC. During first millenium BC, reinforced soil saw its presence in construction of Tower of Babel. Ziggurat Aqar Quf, a monument located close to present day Baghdad (constructed between 1595-1171 BC), stands 54 meters high till today. The structure was built using reinforced blocks of 400 mm cubes of compact soil - reinforced with river reeds. Reinforced soil was also widely used in river training works

since third millennium BC, when clay fills reinforced with reeds were used along the banks of Tigris and euphrates (Ingold, 1994, Chap. 1). Reinforced soil is found to be used in numerous river training works since then. Some parts of the "Great wall of China" in Gobi desert used compacted sand and gravel reinforced with branches and reeds, where reinforcements were vertically spaced at 0.2 to 0.3 meters in segments where stone blocks and other conventional construction materials of the time - were scarce (Jones, 1986, Chap. 1).

In recent history, crushed aggregates inside steel mesh boxes tied together were used as "gabion walls". Wooden reinforcements were used for stabilizing slopes, building stable grounds and river training works. First use of designed soil reinforcement is often accredited to Henry Vidal of France during 1963 AD. Since then, use of reinforced soil has found its application in many forms - in a diverse range of geotechnical situations. More recently, soil reinforcement materials majorly converge in form of polymeric materials. Natural fibres and steel reinforcements are also used in situations with specific requirements. Popularity of polymers is due to their high resistance to biological and chemical degradation. Polymeric materials are also popular because they can be specifically designed and manufactured according to functional need.

In Skedsmo (25 km northeast to Oslo, Norway), a reinforced soil structure was constructed by Norwegian Geotechnical Institute (NGI) using polymeric geosynthetics about 32 years ago in July of 1987 AD. Tests and research are still ongoing on behaviour of the structure and the reinforcements. A considerable amount of long term data and analysis for long/short term performance of geosynthetically reinforced structures has been performed at the site (Quinteros (2014)).

The term "geosynthetic" was first used by Giroud and Perfetti in 1977 AD. ASTM D4439 defines a geosynthetic as:

> **geosynthetic,** *n*—a planar product manufactured from polymeric material used with soil, rock, earth, or other geotechnical engineering related material as an integral part of a man-made project, structure, or system.

Figure 1.1: Definition of geosynthetic from ASTM D4439

Application of geosynthetics surmises four major functions that they can perform: reinforcement, separation, filtration and drainage. Different types of geosynthetics are used for performing these different functions. According to Koerner (2005), there are eight different types of

geosynthetics which he listed as : geotextiles, geogrids, geonets, geomembranes, geosynthetic clay liners, geopipe, geofoam and geocomposites. The last item "geocomposites" accommodates for geosynthetics formed by combination of two or more type of aforementioned geosynthetics. Drainage and filtration properties are of primary consideration while classifying geosynthetics and they majorly influence performance and strength of the final reinforced soil structure.

Geosynthetically reinforced soil structures are cost-effective alternatives to conventional (steel and concrete) structures used for slope stability, erosion control, embankments, roadway elements, subsurface drainage systems, retaining walls and abutments among many others. It is suitable for construction over soft foundation, has a higher seismic resilience and uses soil as primary construction material. It can be significantly more aesthetic and economic option to available methods. It incorporates soil as a structural component; which in turn can have many advantages.

This thesis report concerns about design of bridge abutments using geosynthetically reinforced soil.

1.2 Geosynthetically Reinforced Soil Bridge Abutments

Application of geosynthetically reinforced soil retaining structures as bridge abutments dates back to 1994 AD when the Japan Railway constructed several bridge abutments and piers using this method. According to field measurements, those first bridge abutments have performed well within settlement limits and have out-performed conventional steel and concrete abutments during Great Hansin Earthquake of Japan in 1995 AD; which measured 7.2 on Richter scale (Tatsuoka et al., 1997). Considerable amount of research and practice has been done since; which has led to a significant development in research and development of design principles and widespread use of the method in practical applications. Some of the early successful applications worldwide include: Black Hawk bridge abutments in Colorado, US (Wu et al., 2001), New South Wales GRS bridge abutments in Australia (Won et al., 1996), Vienna railroad embankments in Austria (Mannsbart and Kropik, 1996), among many others. Most of the design approaches for reinforced soil bridge abutments originates from design of reinforced soil retaining walls.

A schematic drawing of a reinforced soil bridge abutment with flexible wrapped facing and its major components are shown in Figure 1.2. A typical reinforced soil bridge abutment has four distinct functional components: (1) a load bearing wall (lower wall below abutment seat), (2) Back wall (upper wall behind abutment seat), (3) Abutment seat (or sill) and (4) Abutment facing. Additionally, a rock-fill at the bottom of the abutment and an alternative vertical facing is also shown in Figure 1.2. Back wall behind the abutment seat may not necessarily be a reinforced soil wall, as it will not directly carry vertical loads from the bridge. The facing itself is a non-load bearing component of the structure, but the design is heavily influenced by the type of facing considered. The immediate portion below the loading area (below abutment seat) is specially reinforced (denser geosynthetics/gravel base) for better load distribution; depending upon requirements.

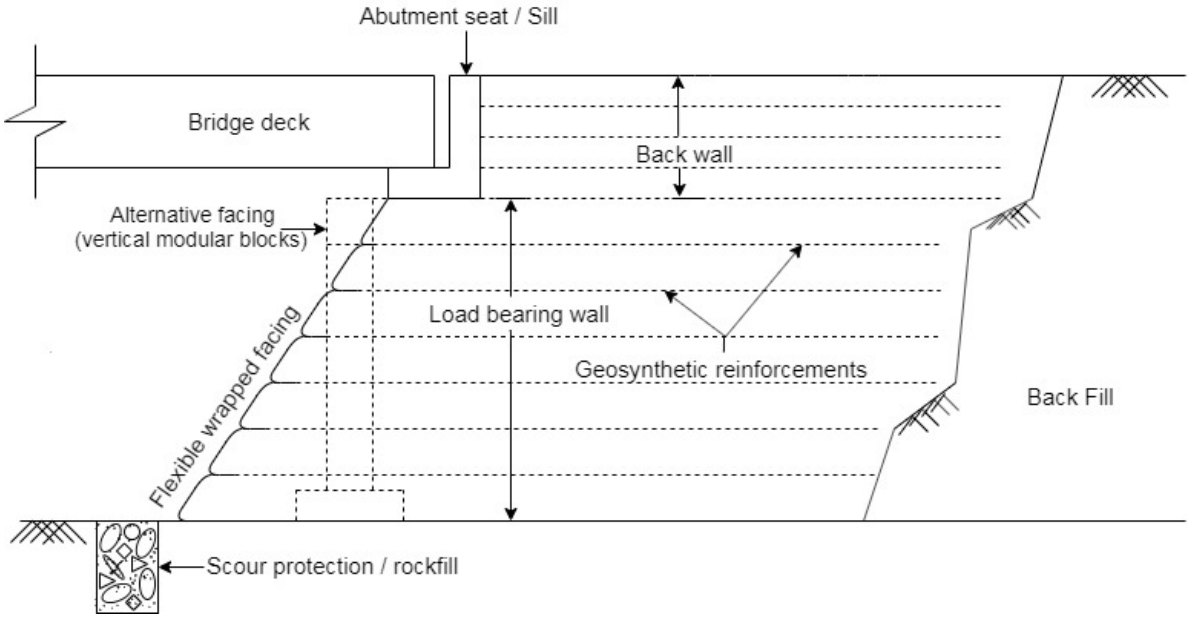

Figure 1.2: Schematic components of a reinforced soil bridge abutment

Reinforced soil bridge abutments are flexible structures and several advantages and disadvantages are associated with its use. General advantages of these structures according to Elias et al. (2001) and Wu et al. (2006) are:

- They are more tolerant towards foundation settlement and seismic loading.
- Construction process is rapid, requires less construction equipment, requires less site preparation and does not require specially skilled craftsmen for construction.

- Reinforced soil birdge abutments do not require embedment into foundation soil for stability and this can be specially advantageous while constructing over soil that should not be excavated due to environmental reasons.
- They are cost effective, ductile, recyclable and they have higher tolerance towards differential settlements.

Generic drawbacks associated with all reinforced soil structures also applies to reinforced soil bridge abutments; such as (Elias et al. (2001)):

- Requires relatively large space behind the wall for obtaining adequate wall size to fulfill external and internal stability.
- Suitable design criteria for corrosion and deterioration of facing elements and reinforcements are required.
- Due to continuously evolving design and construction practice, specifications and construction practices need similar paced standardization.

Increasing laboratory tests, field measurements, post event observations and researches have led to significant change in how these structures are viewed over the years. Substantial increase in design modifications and extended usage in varied situations has been observed in the past; which can only be expected to grow further.

1.3 Objectives

The main objective of this thesis is to obtain a design of a reinforced soil bridge abutment from limit equilibrium calculations and analyse its performance under static and dynamic conditions. Behaviour of the reinforced soil bridge abutment in static and dynamic conditions are of a peculiar interest because the construction mechanism of the reinforced soil bridge abutment is different from conventional concrete and steel bridge abutments.

The motive of the thesis is to find an appropriate design for the considered reinforced soil bridge abutment by analysing it analytically and seismically. The difference in results obtained from analytic calculations and finite element calculations are also of major interest. Interaction of soil and geosynthetics and the gain of strength with induced strain in reinforcements, along with the variation of this interaction under seismic condition is a very interesting phenomenon and it is the objective of this thesis to study and compare these phenomenon for a specific designed reinforced soil bridge abutment.

1.4 Approach

The initial design of the bridge abutment is a limit state design. Numerical calculations are performed with the finite element program PLAXIS 2D.

Firstly, a design is obtained using limit state method and it forms as a base of this thesis. A numerical analysis for static condition is done with the obtained design using PLAXIS 2D. A modification is made for rectifying the base design and reasons and advantages of the rectification is discussed.

Further, a pseudostatic analytic internal design is performed for comparing static and pseudostatic loads. Internal and external stability analysis is performed analytically and the results are compared and discussed.

A dynamic analysis for a simplified model of the designed abutment is then performed with PLAXIS 2D (dynamics). Prior to this analysis, a boundary condition selection test is performed. A dynamic analysis is then performed for the simplified model for the cases with and without geosynthetic reinforcements. The results from the different analyses are compared in terms of stability and performance of the bridge abutment model. The thesis then combines and compares all acquired information in a summary and concludes with recommendation of further

works.

(It is mentioned here that all drawings in Chapter 2 and Chapter 3 are self-made for creating a homogeneity in figures, and hence are not cited in the figure description. The figures however originated from the ideas mentioned in the respective texts it belongs to - where all the citations are performed.)

1.5 Structure of the Report

This thesis is divided into following eight chapters:

- Chapter 1: Introduction

  This chapter gives brief introduction to reinforced soil and geosynthetics, and their application as a bridge abutment. Objectives and approach of this thesis is stated in this chapter.

- Chapter 2: Design Theory and Approaches (Literature Review)

  This chapter discusses the design theories involved in design of reinforced soil bridge abutment. Different types of stability conditions considered in the design, and the most relevant design methods are discussed.

- Chapter 3: Limit Equilibrium Design

  In this chapter, a design for the reinforced soil bridge abutment considered in this thesis is obtained by applying limit equilibrium method for internal and external stability conditions.

- Chapter 4: Numerical Modeling and Safety Analysis

  The design obtained from limit equilibrium method is turned into an abutment model in PLAXIS 2D in this chapter. Soil model selected for the design are briefly discussed and the results are discussed and compared. A modified rectification of the design is reached in this chapter. The chapter concludes with a safety analysis for different stages involved in the calculation.

- Chapter 5: Analytical Seismic Design

  Mononobe-Okabe method and Eurocode 8 are used for a simplified loading condition of the designed bridge abutment for a pseudostatic design. A comparison of the static and

pseudo-static design is done in this chapter.

- Chapter 6: Seismic Modeling and Dynamic Analysis

  A brief mention of mechanism of shear waves and the soil model used is made. The chapter then performs a test for the selection of boundary condition using a simplified model of the designed bridge abutment. Dynamic calculations with and without geogrids are performed in PLAXIS 2D (dynamic mode). Results from the calculations with and without geogrids are then compared in this chapter.

- Chapter 7: Summary and Conclusions

  Results from all design and analyses are discussed in this chapter.

- Chapter 8: Recommendations and Further Works

Chapter 2

Design Theory and Approaches

2.1 Mechanism of Reinforcement

Geosynthetic reinforcements are placed laterally at designed intervals between compacted granular fills in a reinforced soil retaining structure. When observing a single reinforcement, the reinforcement is embedded into soil structure up to a designed length of embedment beyond failure zone, as shown in Figure 2.1

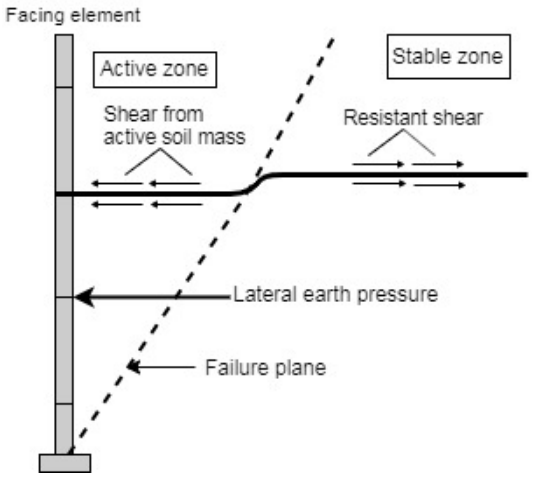

Figure 2.1: Shear distribution on an isolated reinforcement

As additional shear stress develops at shear failure plane of a soil mass, it is transferred into reinforcement-soil interface in terms of friction and adhesion (Hausmann (1990)). Friction develops relative to normal stress and adhesion depends upon material properties of soil and reinforcements. As a result of this shear distribution from active soil mass to reinforcement and

the resisting shear from stable zone; soil mass gains internal equilibrium and is stabilized.

When observing the reinforced soil retaining structure as a whole, the mechanism can be expressed with the help of Mohr-Coulomb failure envelope as shown in Figure 2.2

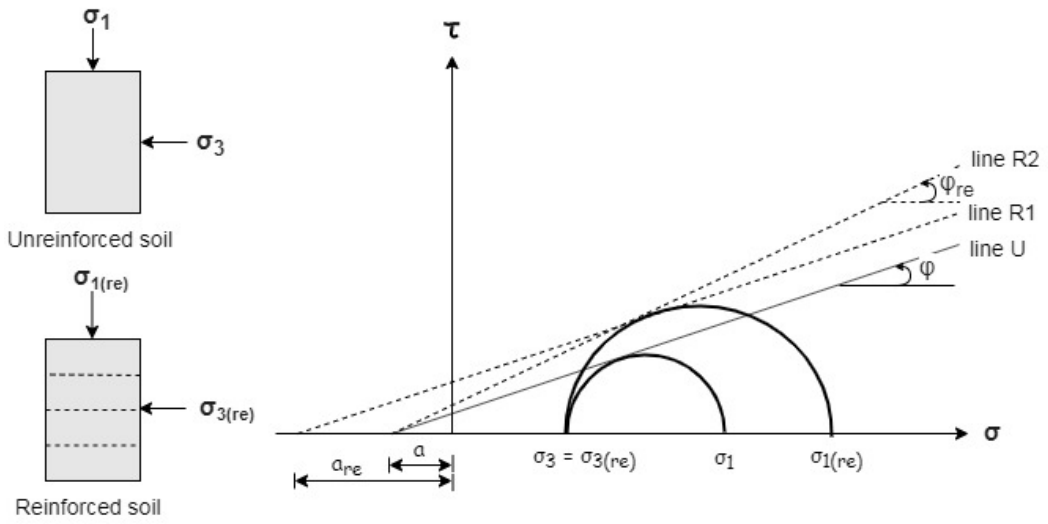

Figure 2.2: Mohr-Coulomb failure envelope and principal stresses in reinforced soil

As depicted in Figure 2.2, reinforced and unreinforced soil masses are considered together; where both are loaded to failure at a constant confining stress. 'Line U' represents failure envelope of unreinforced soil. 'Lines R1 and R2' represent failure envelope of reinforced soil with assumed increase in attraction and friction angle respectively. The subscript 're' denotes that those particular parameters are of reinforced soil context.

Both theories presented by lines R1 and R2 provides us with same shear stress value at failure . Theories depicted by lines R1 and R2 can be expressed as equations 2.1 and 2.2 respectively.

$$\tau_f = (\sigma_f + a_{re}).\tan\phi \tag{2.1}$$

$$\tau_f = (\sigma_f + a).\tan\phi_{re} \tag{2.2}$$

This way of observing 'soil-reinforcement system' as a whole can be helpful in making stress-strain model to describe behaviour of reinforcements in soil at different confining pressures. The single reinforcement behaviour as shown in Figure 2.1 is used generally for analyzing failures due to slippage or rupture of reinforcement. It is shown by Gray and Ohasi (1983), that

failure by slippage is more common for low confining stress and failure by rupture is more likely for higher confining stress. These conditions of failure depend upon properties of the reinforcement and soil-reinforcement interface; but it emphasizes the concept of shear distribution in forms of friction and adhesion as illustrated in Figure 2.1.

2.2 Stability of Reinforced Soil Bridge Abutments

When designing reinforced soil bridge abutments, stability is analysed in one of (or combination of) the modes of stability which are: (1)External stability and (2)Internal stability.

2.2.1 External Stability

External stability describes stability of the abutment when viewed as a singular unit and is responsible for defining the overall geometry of the abutment. External stability is established by treating the whole reinforced soil abutment as a rigid gravity structure and then applying classical geotechnical analysis for safety against sliding, overturning and bearing capacity failure. Factor of safety is calculated as a ratio of resisting forces to driving forces and checked against minimum required factor of safety in codes and specifications.

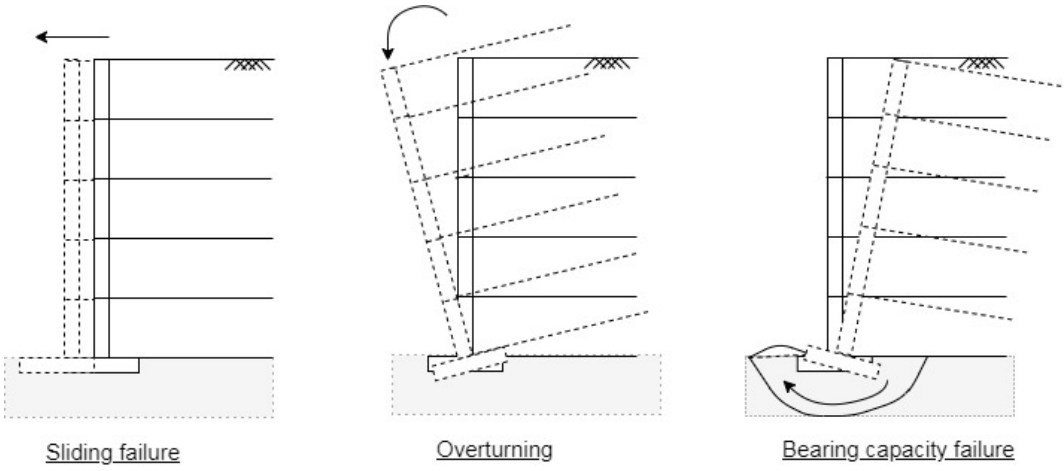

Figure 2.3: Modes of external failure of a reinforced soil abutment

As shown in Figure 2.3, three modes of failure generic to external stability are shown . Slope stability might also be considered when the abutments are to be constructed on steep slopes (Koerner (2005)). Check for overall settlements also fall under external stability conditions. Overall width and height of the abutment is obtained from these stability checks and further

design is done by internal stability analysis, which is considered particularly vital with respect to soil and reinforcement interactive behaviour.

2.2.2 Internal Stability

Internal stability of a reinforced soil abutment depends upon properties of geosynthetics and soil- geosynthetics interface. The geosynthetic reinforcements can either fail by excessive tensile strain and rupture or excessive slippage and pullout. Both of these geosynthetic failures occur due to excessive tensile stress at points where reinforcements meet critical slip surface. Definition of critical slip surface hence becomes important in design. Different approaches have different ways of agreeing upon critical slip surface. Length of reinforcement extending beyond this assumed surface provides resistance towards pullout, and is called embedment length of the reinforcement. Typical modes of internal failure for reinforced soil abutments are shown in Figure 2.4

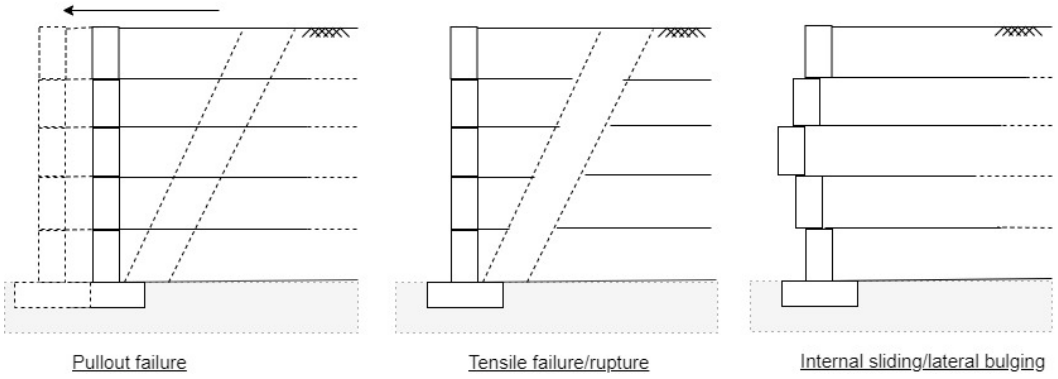

Figure 2.4: Modes of internal failure of a reinforced soil abutment

Several other factors contribute to external and internal stability due to the nature of construction of reinforced soil abutments, such as: abutment geometry, grain size and pore size distribution, foundation situation and adjacent structures/loading . Combination of failure planes inside and outside the wall geometry is analysed in 'Internal Compound Stability', which is integrated in some design approaches and done separately in others (NCMA (2012)).

For estimating soil-reinforcement friction angle and attraction, direct shear tests for geosynthetically reinforced soil can be performed as in ASTMD5321 (2019). Pullout tests are effective in modeling anchorage resistance of soil reinforcements. During pullout tests, soil reinforcement is pulled out at controlled displacement for measuring maximum pullout resistance. The con-

trolled displacement being a result of mobilization of shear strength on surfaces of the geosynthetic reinforcement in both active and stable zone separated by failure plane (as shown in Figure 1.2), the test provides a model of interface behaviour in a particular stress condition. Standard procedure for pullout test for geosynthetics can be performed as in (ASTMD6706 (2013)).

Allowable tensile stresses in geosynthetics should be less than ultimate tensile strength of geosynthetics and similarly, allowable pullout force should be less than than the anchorage resistance for internal stability to be fulfilled. Allowable tensile resistance and allowable pullout force as given by Gofar (2008) states:

$$T_{all} = \frac{T_{ult}.(CRF)}{F_D.F_C.F_S} \tag{2.3}$$

$$P_a \leq \frac{P_r.R_c}{FS_{po}} \tag{2.4}$$

Where in equation 2.3, 'T_{all}' and 'T_{ult}' are allowable and ultimate tensile stresses in geosynthetics. 'CRF' is creep reduction factor. 'F_D, F_C and F_S' are reduction factors for chemical/ biological durability, construction damage and uncertainty for determination of reinforcement strength respectively. Likewise in equation 2.4, 'P_a' and 'P_r' are allowable pullout force and allowable pullout resistance respectively. 'R_c' is coverage ratio and 'FS_{po}' is factor of safety against pullout (Gofar (2008)).

2.3 Modified Limit State and other Approaches of Design

External stability design is performed in conventional geotechnical approach by assuming the geosynhetically reinforced structure as gravity structure. Failure conditions as mentioned in Figure 2.3 are considered for ultimate or serviceability limit state for analysing stability of the wall against different forces.

For internal stability analysis however, many methods have been developed in the past with: modified approach to limit state analysis, internal stress-strain behaviour, numerical models and finite element approaches, case specific and laboratory/field based approaches, or combination of one or more of these approaches. Prominent design approaches for internal stability design adopted by most of the codes and specifications are discussed in the following sub-sections.

2.3.1 Tie - Back Wedge Method

Tie-back wedge method is the most commonly used method and was for the first time used with 'at rest' lateral coefficient (K_o) condition for in-extensible reinforcements by (Steward et al. (1977)) and modified to active earth pressure (K_a) condition by (Murray (1980)). The method assumes an active Rankine earth pressure (K_a) throughout the reinforced zone, with tensile resistant tie-backs extending up to a certain embedment length beyond the failure line.

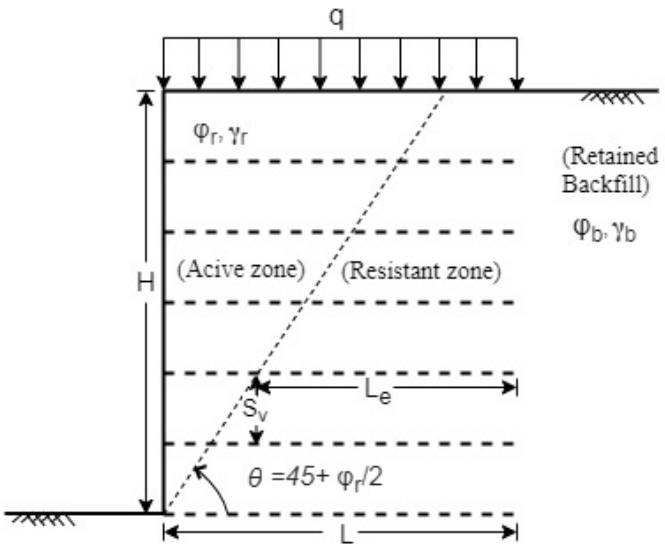

Figure 2.5: Schematic representation of Tie-back wedge method

As shown in Figure 2.5, a simplified vertical abutment with surcharge 'q' throughout the abutment length 'L' is shown. The abutment has a height 'H' and friction angle 'ϕ'. Angle of Rankine failure plane originating from toe of the abutment is 'θ', 'γ' is unit weight of the soil and subscripts 'r' and 'b' denote reinforced soil and backfill soil parameters respectively.

Length and height of the wall is obtained by checking external stability conditions against minimum factor of safety according to the code followed. According to Holtz et al. (1997), minimum factor of safety of: 1.5 for sliding, 2 for Bearing capacity, 2 for overturning and 1.5 for internal stability (tensile rupture and pullout) can be considered. Check against sliding defines the wall width - which in turn is deterministic for length of embedment. For calculating geosynthetic spacing (S_v) and checking embedment length (L_e) of the geosynthetic reinforcements, a maximum spacing of 0.5 meters and minimum embedment of 1 meter is recommended by Holtz et al. (1997).

$$T_n = S_v.\sigma_h \tag{2.5}$$

Horizontal stress at each reinforcement level (σ_h) is then calculated along the assumed active Rankine failure line using moist unit weight of reinforced backfill and all present surcharge loads assuming an equivalent Meyerhof-type distribution. Required tensile strength at n^{th} layer (T_n) of the geosynthetic reinforcement then depends upon vertical spacing of the reinforcements (S_v) and horizontal earth pressure at middle of that particular layer (σ_h) as shown in equation 2.5.

2.3.2 Coherent Gravity Method

Coherent gravity method was originally developed for steel grid reinforcements and assumes high pullout resistance for internal stability (Anderson et al. (2010)). According to laboratory results from Laboratoire Central des Ponts et Chaussees (LCPC) of France; conducted for reinforced soil models, locus of maximum tensile stresses differed from Rankine's failure plane and followed a bi-linear curve (Schlosser and Long (1974)). Coefficient of lateral earth pressures too varied from 'K_o' at top of the wall to 'K_a' below a depth of 6 meters (Craig (2004)). At failure, movement start at the toe of the wall and rotation is observed at the top.

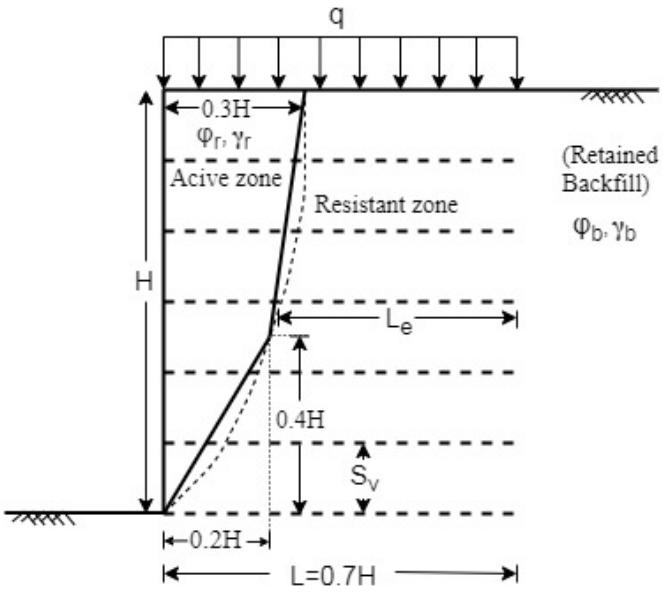

Figure 2.6: Schematic representation of Coherent gravity method

As shown in Figure 2.6, locus of maximum tensile stress is shown and the straight lines join-

ing a point '0.4H' with the abutment extremities represents the binomial approximation of the curve for simplification (Craig (2004)). Internal stability analysis follows similar approach of calculating lateral stress and subsequently calculates tensile forces for each layer as in equation 2.5. Earth pressure coefficient however, differs along with depth. Meyerhof-type bearing pressure is assumed at the base and eccentric loading is assumed due to vertical and horizontal loads (Anderson et al. (2010))

2.3.3 Two-Part Wedge Method

Method of two part wedge is also a limiting equilibrium method, but it considers all failure mechanisms and forces associated with it. The method requires very few assumptions to reach the solution, as large number of combination of wedges are analysed for critical behaviour.

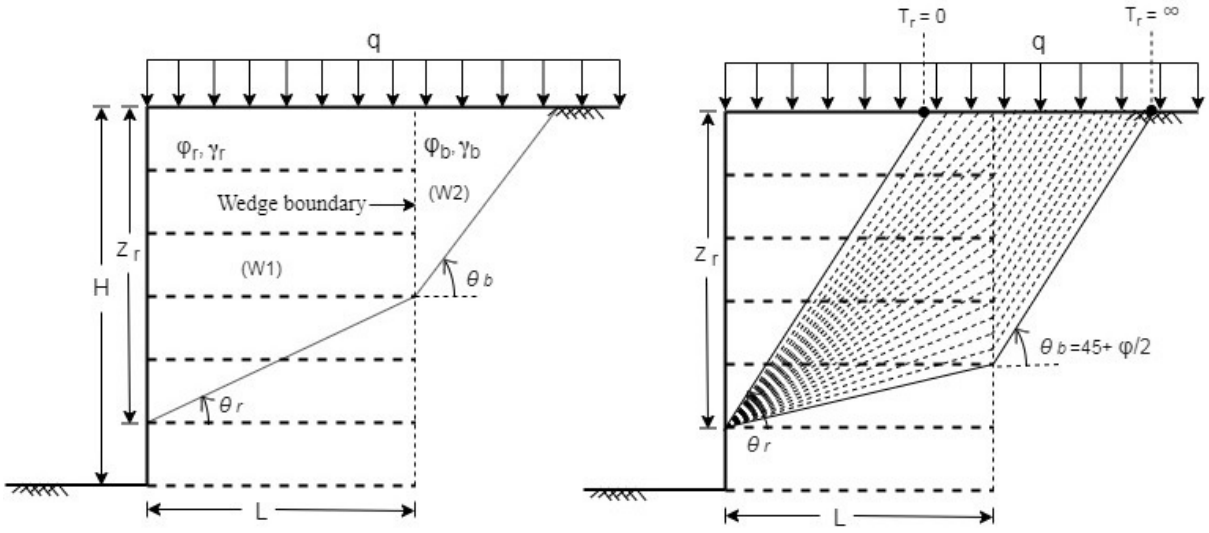

Figure 2.7: Schematic representation of Two-part wedge method

As shown in Figure 2.7, the method assumes combination of two wedges originating beyond reinforced soil region for analysis of internal stability. The load 'q' is shown to extend beyond reinforced zone as the analysis includes that part (Dobie (2015)). 'θ_r' and 'θ_b' represents angle of inclination of failure wedges 'W1' and 'W2' respectively. Wedge 'W1' lies in reinforced soil zone and 'W2' lies in backfill soil zone, connected by the 'wedge boundary'. 'T_r' represents tensile strength of reinforcement in this case.

Figure 2.7 (left) shows the two wedges as 'W1' and 'W2' inclined at angles 'θ_r' and 'θ_b' respectively, below a depth 'Z_r' from top of the abutment. The depth 'Z_r' varies from 'Z_r=H' at bottom

of the abutment to zero at the top. 'Z_r' is considered for each layer of geosynthetic reinforcement. As shown in Figure 2.7 (right), all possible failure planes from height 'Z_r' is considered. 'θ_r' changes with each possibility of failure plane but 'θ_b' remains same (Rankine failure plane can be assumed for 'θ_b' as it lies outside reinforcement zone). The analysis covers failure planes obtained from '$T_r = 0$' to '$T_r = \infty$' and is repeated for new 'Z_r' at each layer (Xu and Hatami (2019)). The design is based on principle that resistance provided by the reinforcement needs to stabilize the forces due to both wedges - at all considered failure plane combination.

2.3.4 Stiffness Methods

Stiffness based method was first proposed by Bathurst et al. (2005). The methods are empirically developed working stress methods, based on case studies of geosynthetically reinforced vertical walls with a variation of facings. Load on reinforcement is calculated by converting measured strains form case studies to reinforcement loads by using reinforcement stiffness values. The stiffness of reinforcement considered here are in-isolation isochronous creep stiffness which are found to give a more reasonable stiffness values in compared to values provided by a tensile test (Walters et al. (2002)). The database for the empirical method grows continuously and a reinforced geosynthetic wall of height up to 11 meters have been constructed using the design approach (Bathurst and Allen (2014)).

The most recent version of the method as described in Bathurst and Allen (2018) gives the maximum reinforcement load (T_{max}) for vertical wall with cohesionless backfill as:

$$T_{max} = S_v.[H.\gamma_r.D_{max}].K_a.\Phi_g.\Phi_{fs} \tag{2.6}$$

Where 'S_v' is vertical spacing of reinforcements, 'H' is wall height, 'γ_r' is unit weight of backfill soil, 'D_{max}' is distribution factor, 'K_a' is active earth pressure coefficient, 'Φ_g' and 'Φ_{fs}' are influence parameters relating to global safety and facing factor respectively.

The method advocates to predict the loads in reinforcement more accurately and economically. The findings of the emperical method however, is restricted to types of structures and reinforcements that were considered during its development.

2.4 Codes and Standards used

In this thesis, AASHTO (2007) load and resistance factor design (LRFD) manual is referred for load and resistance factors in the limit equilibrium design in Chapter 3. Eurocode 8 (NS-EN 1998-5:2004+NA:2014 (1998)) is followed for analytical seismic analysis in Chapter 5. Holtz et al. (1997) and Berg et al. (2001) have been important sources of data about geosynthetics throughout this report.

Chapter 3

Abutment Design using Limit Equilibrium

Reference for soil data and structural geometry for the design of abutment considered here is based upon the steep slope reinforced wall project of NGI constructed in 1987, near Oslo. Long term and short term performance data since the commencement of the project till recent dates are available, which forms the basis of source of data used in this design. Fannin and Hermann (1990) and Quinteros (2014) among many other papers on the topic illustrate the soil properties at the site. Reinforced soil and backfill soil used are 'Skedsmo sand'. Water table is assumed to be significantly below the structure and does not incur additional forces in the design. The abutment is constructed above the firm ground and has same properties as compacted sand used in rest of the structure. The facing of the abutment is vertical and a concrete spread footing is cast in place for distributing loads from the superstructure to the abutment.

Stability analysis of the spread footing, external stability and internal stability are performed separately for maintaining ease in comparison of modes and stages of failure. Loads and reactions from the bridge to the abutment considered in this design are based upon load and resistance factor design (LRFD) as described in AASHTO (2007) bridge specification. Design guidelines and examples given in Berg et al. (2001) and Holtz et al. (1997) were utilized in accordance with the specification. Assumptions regarding failure modes and load-resistance behaviour present in the specification are hence an integral part of this design.

Preliminary requirements assumed for the abutment defines the context under which the design is considered and is stated in Table 3.1.

Table 3.1: Preliminary requirements assumed for the abutment

Preliminary requirements	
Height of the abutment (H_t=H_a+d)	5 meters
Width of the abutment (W_a)	10 meters
Design Life	100 years
Facing of the abutment	Vertical precast panels
Abutment seat/sill	Cast in place concrete spread footing
Type of reinforcement	Geosynthetic

Side walls for the abutment are assumed to extend at a stable slope from top of the abutment to ground level, and plain strain condition is assumed to be valid. For the requirements mentioned in Table 3.1, an 'in-scale' schematic representation of the abutment components and soil zones are shown in Figure 3.1. Soil of similar properties is assumed for reinforced soil used behind the spread footing, within the abutment and foundation soil.

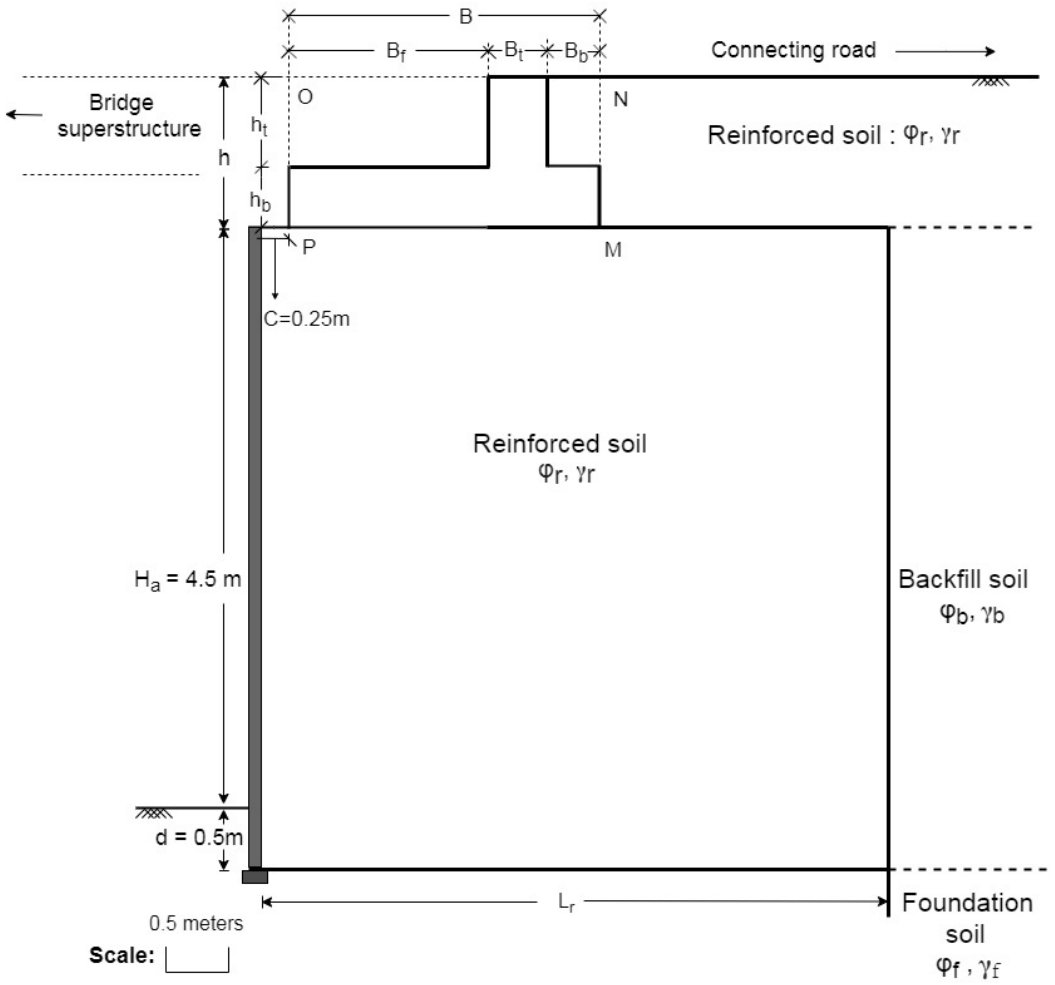

Figure 3.1: Schematic diagram for abutment components and soil zones as in Table 3.1 (in-scale)

For the schematic abutment shown as in Figure 3.1, properties of soil at different portion of the structure, dimension and material properties of spread footing, reaction due to bridge load and bearing capacity of soil for ultimate and serviceability limit states are then defined in Table 3.2.

Table 3.2: Essential parameters defined for design

Essential Design Parameters			
Soil properties	Reinforced soil	γ_r=17 kN/m^3	ϕ_r=33^o
	Backfill soil	γ_b=16 kN/m^3	ϕ_b=30^o
	Foundation soil	γ_f=17 kN/m^3	ϕ_f=33^o
Spread footing	Dimension	B $\leqslant$ H_t h $\leqslant$ 0.5 (H_t)	
	Material properties	γ_c=23.5 kN/m^3	
Bridge loads (unfactored)	Dead load	DL=155 kN/m	
	Live load	LL=83 kN/m	
	Lateral friction	FL=12 kN/m	
Bearing resistance(Factored)	Foundation soil	Ultimate Limit State (ULS)	Q_{fu}=718 kPa
		Serviceability State (SS)	Q_{fs}=335 kPa
	Reinforced soil	Ultimate Limit State (ULS)	Q_{ru}=335 kPa
		Serviceability State (SS)	Q_{rs}=192 kPa

In addition to soil properties mentioned in Table 3.2, 'mean grain size' (d_{50}) of the sand used as reinforced soil is 0.2 mm with 'Coefficient of uniformity' (C_u) as 2.6 in accordance with Fannin and Hermann (1990). A gap of 'C=0.25m' is assumed from toe of spread footing to the beginning of precast facing as shown in Figure 3.1. Depth of embedment (d) below ground level of the abutment according to Holtz et al. (1997) is defined as d = $H_t/10$ = 0.5 meters. Length of reinforced zone is assumed equal to height of the abutment (including embedment depth) for preliminary calculations (i.e., $H_t = L_r$).

Horizontal forces (friction and lateral earth pressure) and vertical forces (self weight and external loads) are calculated as equivalent point loads (PL), uniformly distributed loads (UDL) or uniformly varying loads (UVL) depending upon type of loading. Toe of the spread footing is denoted by 'T' and toe of the abutment is denoted by 'B' as points where limiting moments would be considered for equilibrium. Dead loads and live loads imparted by bridge superstructure onto spread footing are represented by point loads acting at the midpoint of 'B_f' as mentioned in Figure 3.2.

An equivalent soil surcharge is assumed to represent live loads on the connecting road portion of the abutment as per tables 3.11.6.4-1 and 3.11.6.4-2 of AASHTO (2007). According to which, equivalent soil surcharge of 0.6 meters is considered for portion of connecting road be-

hind the spread footing and section above spread footing. The height of the equivalent minimum soil surcharge is considered separately for representing realistic load behaviour onto the abutment, and is denoted by 'h$_{eqs}$' and 'h$_{eqb}$', for portion above and beyond the spread footing respectively. Vertical and horizontal components of the equivalent live surcharge are denoted by 'V$_{sa}$', 'V$_{sb}$', 'F$_{sa}$' and 'F$_{sb}$' depending upon their location of application, as depicted in Figure 3.2.

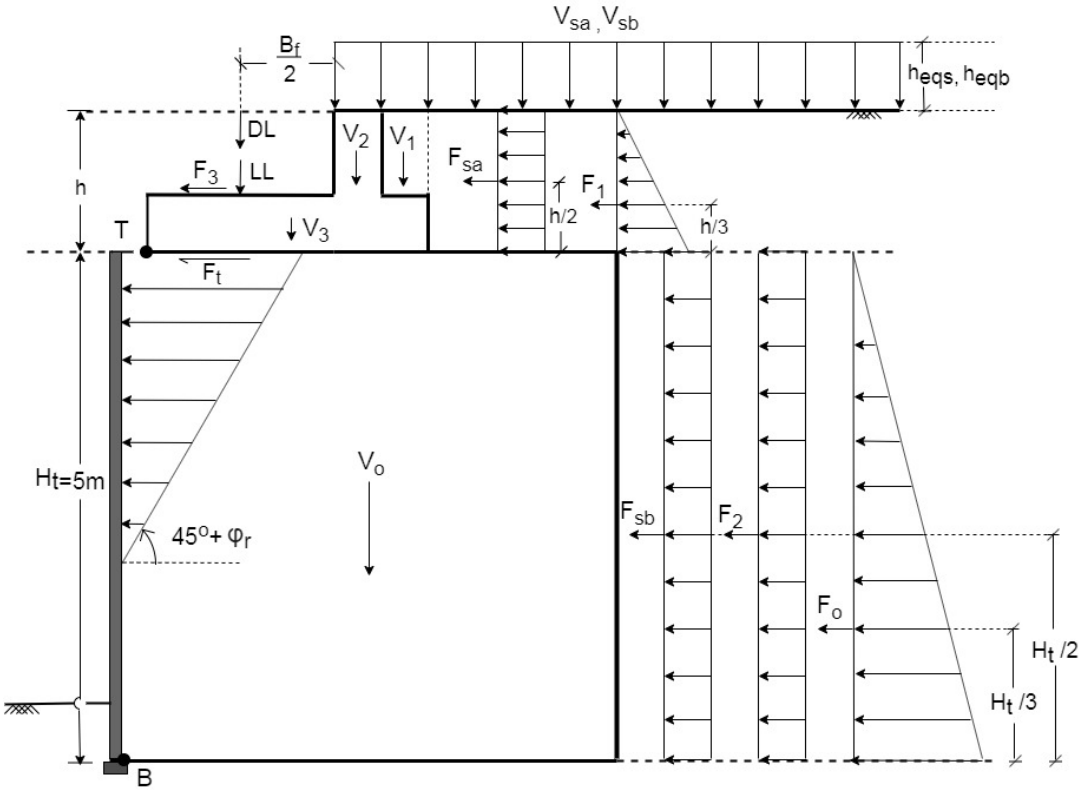

Figure 3.2: Forces involved in the abutment as in 3.1 (not to scale)

Horizontal and vertical forces involved in the abutment are used to calculate moments about points 'T' and 'B' as shown in Figure 3.2. An active state is assumed for lateral earth pressure and is calculated as in Equation 3.1. According to which, 'Active earth pressure coefficient (K$_a$)' for backfill soil (K$_{ab}$) is 0.33 and for reinforced soil (K$_{ar}$) is 0.30 as per soil properties mentioned in Table 3.2.

$$K_a = \frac{1-\sin\phi}{1+\sin\phi} \tag{3.1}$$

Table 3.3 and 3.4 summarises all vertical and horizontal forces along with their moments. Equations involved in calculation of the forces, moment arms and moments are tabulated in Appendix B (Tables B.1, B.2, B.3 and B.4). All forces mentioned are categorized into load types which are given a load factor for strength and serviceability conditions. Stability analyses are performed for failure modes considered in Chapter 2 (i.e., for stability of spread footing and external/internal stability of the abutment). Specific reason behind performing separate stability check is that it allows room for observation in viewing load-resistance equilibrium. It also gives clear overview of factor of safety between failing and resisting forces at each mode of all stability analyses.

Table 3.3: Vertical forces and unfactored moments for forces in Figure 3.2

Vertical forces and unfactored moments about 'T' and 'B'						
Vertical forces (in kN/m)		**Moment-arm (in m)**		**Unfactored moment (in kNm/m)**		
Symbol	**Value**	**About 'T'**	**About 'B'**	**Symbol**	**About 'T'**	**About 'B'**
V_0	425.00	-	2.50	VM_0	-	1062.5
V_1	4.76	2.25	2.50	VM_1	10.71	11.90
V_2	6.58	1.85	2.10	VM_2	12.17	13.82
V_3	28.79	1.23	1.48	VM_3	35.26	42.46
DL	155.00	0.83	1.08	VM_d	127.88	166.63
LL	83.00	0.83	1.08	VM_l	68.48	89.23
V_{sa}	7.68	2.05	2.30	VM_{sa}	15.74	17.66
V_{sb}	22.08	3.60	4.25	VM_{sb}	79.49	93.84

Table 3.4: Horizontal forces and unfactored moments for forces in Figure 3.2

Horizontal forces and unfactored moments about 'T' and 'B'						
Horizontal forces (in kN/m)		**Moment-arm (in m)**		**Unfactored moment (in kNm/m)**		
Symbol	**Value**	**About 'T'**	**About 'B'**	**Symbol**	**About 'T'**	**About 'B'**
F_0	66.00	-	1.67	HM_0	-	110.00
F_1	7.04	0.40	5.40	HM_1	2.82	38.01
F_2	33.66	-	2.50	HM_2	-	84.15
F_3	12.00	0.50	5.50	HM_3	6.00	66.00
F_{sa}	3.46	0.60	5.60	HM_{sa}	2.07	19.35
F_{sb}	15.84	-	2.50	HM_{sb}	-	39.60
F_t	22.49	case-wise	case-wise	HM_t	case-wise	case-wise

Horizontal force 'F_t' mentioned in last row of Table 3.4 is frictional force at the bottom of spread footing (i.e. $F_t = F_1+F_{sa}+F_3$). Reinforced abutment is considered as a singular unit for external stability and spread footing stability analyses. But additional forces come into calculation during internal stability analysis. Due to which, frictional resistance at bottom of the spread footing behaves differently and is hence calculated 'case-wise' as stated in final row of Table 3.4.

Table 3.5: Load factors as per AASHTO (2007) (Table 3.4.1-1 and 3.4.1-2)

Loads as in Table 3.3 and 3.4		**Load factors**		
Loads	**Load type**	**Max. strength (S_{max})**	**Min. Strength (S_{min})**	**Seviceability (S_{erv})**
V_1,V_0	Vertical Earth	1.35	1.00	1.00
V_2,V_3, DL	Dead load	1.25	0.90	1.00
V_{sa}, V_{sb}, F_{sa}, F_{sb}	Earth Surcharge	1.75	1.75	1.00
F_0, F_1, F_2	Lateral Earth	1.50	0.90	1.00
F_3, F_t	Frictional	1.00	1.00	1.00
LL	Live Load	1.75	1.75	1.00

Load factors and load classifications considered in Table 3.5 are as per Table 3.4.1-1 and 3.4.1-2 of AASHTO (2007), which is referenced for limit equilibrium design part of this thesis. Load type 'Earth surcharge' as mentioned in Table 3.5 represents equivalent live loads due to traffic and is given same load factor as live loads.

Table 3.6: Resistance factors as per AASHTO (2007) (Table 10.5.5.2.2-1 and 11.5.6-1)

Failure modes against	**Resistance factors (β)**
Sliding of spread footing	0.80
Sliding of abutment	1.00
Bearing capacity of abutment	0.65
Tensile resistance of reinforcements	0.75
Fullout resistance of reinforcements	0.90

Resistance factors as stated in Table 3.6 are applied against cumulative resisting forces in each failure mode and also is according to AASHTO (2007). Resistance factor is however denoted by 'β' in this case, as the original notion clashed with the notion of friction angle.

3.1 Stability of the Spread Footing

Failure modes analysed for stability of spread footing are similar to external failure modes of abutment (against overturning, sliding and bearing capacity failure). 'S_{max}' and 'S_{min}' represent ultimate limit states considered for the design and 'S_{erv}' represents limit state of serviceability. An extreme case is also evaluated selecting critical values at each step for representing worst case scenario, which is denoted by 'C_r'. Following sub-sections perform separate check for these failure modes.

3.1.1 Overturning Resistance and Limiting Eccentricity of Spread Footing

As shown in Table 3.7, factored overturning moment 'M_o' acting upon the footing is negligible in comparison to resisting moment 'M_r' acting upon it. Dimension of the spread footing however, highly depends upon limiting eccentricity criteria. Limits of eccentricity mentioned in Table 3.7 are based upon assumption that for strength limit, the resultant should lie between middle of the footing width and half of the distance from middle of the footing to the edge (e' = B/2-B/4 = B/4 for strength). Similarly for serviceability, resultant should lie between middle of the footing to center of gravity of an assumed triangular resultant (e'=B/2 - B/3 = B/6 for serviceability).

Table 3.7: Overturning and eccentricity limiting state analysis of spread footing

Description	**Value**	**Unit**	$\mathbf{S}_{max}$	$\mathbf{S}_{min}$	$\mathbf{S}_{erv}$	$\mathbf{C}_r$
Overturning moments about 'T' (M_o=HM_1+HM_{sa}+HM_3)	10.89	kNm/m	13.85	12.16	10.89	13.85
Resisting moments aabout 'T' (Mr=VM_1+VM_2+VM_3+VM_d)	186.02	kNm/m	233.60	168.49	186.02	168.49
Residual moment at point 'T' (M_{res} = M_r-M_o)	175.13	kNm/m	219.75	156.33	175.13	154.64
Cumulative vertical forces in footing (V_{sum}=V_1+V_2+V_3+DL)	195.13	kN/m	244.39	176.09	195.13	176.09
Location of resultant from 'T' (t=M_{res}/V_{sum})	0.90	m	0.90	0.89	0.90	0.88
Eccentricity from center of footing (e=(0.5·B) - t)	0.33	m	0.33	0.34	0.33	0.35
Limit of eccentricity (e'=B/4 for Strength , B/6 for Serviceability)	0.61, 0.41	m	0.61	0.61	0.41	0.61
Fulfillment of eccentricity citeria (e < e')	Yes	-	Yes	Yes	Yes	-
Fulfillment of critical strength criteria (C_v)	Yes	-	-	-	-	Yes

3.1.2 Resistance against Sliding of Spread Footing

Sliding force 'F_t' is negligible in comparison to vertical forces 'V_f' acting upon the footing as shown in Table 3.8.

Live loads are considered only in cases where they act as failing forces. Resisting vertical forces are directly converted into their horizontal component geometrically, by multiplying with 'Tan(ϕ_r)'. The spread footing shows fulfilment of all criteria of comparison for resistance against sliding with a significantly high factor of safety.

Table 3.8: Sliding resistance limiting state analysis of spread footing

Description	Value	Unit	S_{max}	S_{min}	S_{erv}	C_r
Sliding forces at footing base (F_t=F_1+F_{sa}+F_3)	22.49	kN/m	28.61	24.38	22.49	28.61
Resisting vertical forces from footing (V_t=V_1+V_2+V_3+DL)	195.13	kN/m	244.39	176.09	195.13	176.09
Unfactored sliding resistance (V_u=$V_t \cdot \mathrm{Tan}(\phi_r)$)	126.83	kN/m	158.85	114.46	126.83	114.46
Factored sliding resistance ($V_f = \beta_{sliding} \cdot V_u$)	101.47	kN/m	127.08	91.57	101.47	91.57
Fulfillment of sliding resistance criteria ($V_f > F_t$)	-	-	Yes	Yes	Yes	
Fulfillment under critical conditions ($V_{f(min)} > F_{t(max)}$)	-	-	-	-	-	Yes

3.1.3 Resistance against Bearing Capacity Failure of Spread Footing

Bearing stress from the footing to the abutment is calculated as a ratio of vertical forces upon the footing base and its effective width as shown in Table 3.9.

Table 3.9: Bearing resistance limiting state analysis for spread footing

Description	Value	Unit	S_{max}	S_{min}	S_{erv}	C_r
Overturning moments about 'T' (M_o=HM_1+HM_{sa}+HM_3)	10.89	kNm/m	13.85	12.16	10.89	13.85
Resisting moments about 'T' (M_r=VM_1+VM_2+VM_3+VM_d+VM_{sa}+VM_l)	270.24	kNm/m	380.98	315.87	270.24	270.24
Residual moment at point 'T' (M_{res}=M_r-M_o)	259.35	kNm/m	367.13	303.71	259.35	256.39
Cumulative vertical forces in footing (V_{sum}=V_1+V_2+V_3+DL+LL+V_{sa})	285.81	kN/m	403.08	334.78	285.81	403.08
Location of resultant from 'T' (t = M_{res}/V_{sum})	0.91	m	0.91	0.91	0.91	0.64
Eccentricity from center of footing (e=0.5·B - t)	0.32	m	0.31	0.32	0.32	0.59
Limit of eccentricity (e'=B/4 for Strength , B/6 for Service)	0.61 , 0.41	m	0.61	0.61	0.41	0.61
Fulfillment of eccentricity citeria (e < e')	Yes	-	Yes	Yes	Yes	Yes
Efective width of footing (B'= B-2e)	1.81	m	1.82	1.81	1.81	1.27
Bearing stress from footing (σ_v=V_{sum}/B')	157.48	kPa	221.27	184.51	157.48	316.84
Bearing capacity (factored) (Q_{ru} , Q_{rs} - given in table 3.2)	335 , 192	kPa	335.00	335.00	192.00	335.00
Fulfillment of bearing capacity criteria (Q_{ru} , $Q_{rs} > \sigma_v$)	Yes	-	Yes	Yes	Yes	Yes
Influence depth for 'Ft' L_i= (C+B') · Tan(45+ϕ_r/2)	3.80	m	3.82	3.82	3.80	2.80

Eccentricity check is done again for this case because contribution of live loads is considered while calculating bearing stress. Bearing resistance criteria at critical condition shows marginal factor of safety as shown in Table 3.9. Influence depth as mentioned in the last row of Table 3.9, is calculated so as to observe if the force 'F$_t$' has its influence up to the bottom of the abutment.

3.2 External Stability of the Abutment

Superimposition of loads is assumed for analysing combined effect of loads in this case. Earth surcharge is assumed uniformly above the abutment level and all other dead loads, live loads and live surcharge equivalents are assumed to be superimposed on top of it.

3.2.1 Overturning Resistance and Limiting Eccentricity of the Abutment

Table 3.10: Overturning and eccentricity limiting state analysis of the abutment

Description	Value	Unit	S_{max}	S_{min}	S_{erv}	C_r
Soil weight in block MNOP (W_m=h·(B+C)·γ_r) , as in Figure 3.1	55.08	kN/m	82.62	49.57	55.08	-
Live surcharge in MNOP (W_l=(B+C)·γ_r·h_{eqb})) , as in Figure 3.1	27.54	kN/m	48.20	48.20	27.54	-
Soil weight and surcharge in MNOP (W_s=W_m+W_l)	82.62	kN/m	144.59	144.59	82.62	-
Vertical forces from bridge (no LL) (V_c=V_1+V_2+V_3+DL)	195.13	kN/m	244.39	176.09	195.13	-
Vertical forces from bridge (with LL) (V_c'=V_1+V_2+V_3+DL+LL+V_{sb})	300.21	kN/m	428.28	359.98	300.21	-
Net load from the bridge (no LL) (P_l=V_c - W_m)	140.05	kN/m	175.06	126.04	140.05	-
Net load from the bridge (with LL) (P_l'=V_c'-W_s)	217.59	kN/m	326.38	288.30	217.59	-
Length of moment arm for P_l from 'B' (L_p=t+C)	1.15	m	1.15	1.15	1.15	-
Length of moment arm for P_l' from 'B' (L_p'=t'+C)	1.16	m	1.16	1.16	1.16	-
Resisting moment about 'B' from P_l (MP_l=P_l · L_p)	160.71	kNm/m	200.89	144.64	160.71	144.64
Vertical forces at bottom (no LL) (V_b=P_l+V_o+V_4)	667.05	kN/m	886.51	653.04	667.05	653.04
Resisting moment about 'B' (no LL) (M_{rb}=VM_o+VM_4+MP_l)	1478.21	kNm/m	1979.51	1436.64	1478.21	1436.64
Overturning moment at 'B' (with LL) (M_{ob}=HM_o+HM_2+HM_{sb}+HM_t)	357.11	kNm/m	545.56	355.06	357.11	545.56
Resultant resisting moment about 'B' (M_{resb}=M_{rb} - M_{ob})	1121.10	kNm/m	1433.95	1081.58	1121.10	891.08
Location of resultant force from 'B' (t_b=M_{resb}/V_b)	1.68	m	1.62	1.66	1.68	1.364
Eccentricity at base of the abutment (e_b=L_r/2 - t_b)	0.82	m	0.88	0.84	0.82	1.14
Limit of eccentricity (e_b'=L_r/4 for Strength , L_r/6 for Service)	1.25 , 0.83	m	1.25	1.25	0.83	1.25
Fulfilment of eccentricity criteria (e_b' > e_b)	Yes	-	Yes	Yes	Yes	Yes
Critical condition for strength (C_v)	Yes	-	-	-	-	Yes

As shown in Table 3.10, overturning resistance of the abutment is calculated at point 'B' and eccentricity is analysed at the base of the abutment. Assumptions for derivation of limits of eccentricity are same as that were assumed for spread footing. Overturning moment about 'B' - 'M_{ob}' is considerably lower than resultant residual moment 'M_{resb}' and the analysis focuses more on meeting eccentricity criterion. Serviceability limit state values are almost equal to their limit, and they satisfy the safety conditions.

Net load from the bridge 'P_l' as mentioned in Table 3.10 is obtained as calculation of super-imposed loads and deduction of overlapping loads. Due to which a block 'MNOP' as shown in Figure 3.1 needs to be reduced where footing is placed, for earth surcharge and live equivalent surcharge load considerations. Limit states for strength, serviceability and critical state is same as mentioned for stability of spread footing.

3.2.2 Resistance against Sliding of the Abutment

At the base of the abutment, lateral earth pressure adds a significant amount of load that can provoke sliding at the base. Although effect of 'F_t' does not reach up to the base of the abutment as shown in the last column of Table 3.9 by 'L_f', it is considered in this analysis (as rigid facing is assumed and it can transfer sliding effects from 'F_t' to base - which would depend upon rigidity of the facing).

Table 3.11: Sliding resistance limiting state analysis of the abutment

Description	Value	Unit	S_{max}	S_{min}	S_{erv}	C_r
Sliding forces at abutment base (F_b=F_o+F_1+F_2+F_3+F_{sa}+F_{sb})	137.99	kN/m	205.82	141.80	137.99	205.82
Resisting vertical forces at the base (no LL) (V_b=P_l+V_4+V_o)	667.05	kN/m	886.51	653.04	667.05	653.04
Unfactored sliding resistance (V_{ub}=$V_b \cdot \mathrm{Tan}(\phi_f)$)	433.58	kN/m	576.23	424.48	433.58	424.48
Factored sliding resistance (V_{fb}=$\beta_{sliding} \cdot V_{ub}$)	433.58	kN/m	576.23	424.48	433.58	424.48
Fulfillment of sliding resisatance criteria ($V_{fb} > F_b$)	Yes	-	Yes	Yes	Yes	-
Fulfillment under critical coditions ($V_{fb(min)} > F_{b(max)}$)	Yes	-	-	-	-	Yes

As shown in Table 3.11, factor of resistance 'β' from Table 3.6 is used for sliding, which is unity in this case and it leaves unfactored sliding resistance unaltered from the factored sliding resistance. It is also observed that resisting vertical forces provide considerable factor of safety

against sliding at the base.

3.2.3 Resistance against Bearing Capacity Failure of the Abutment

Eccentricity is calculated again for this case as live loads are included in bearing capacity limit analysis. Bearing stress from the bridge including live loads (P_l') are taken from Table 3.10 - seventh row and divided by effective width (L_r-2e_b).

Table 3.12: Bearing resistance limiting state analysis of the abutment

Description	Value	Unit	S_{max}	S_{min}	S_{erv}	C_r
Bearing stress from net bridge load (P_l') ($\Delta\sigma$=P_l'/B' from Table 3.10)	47.67	kPa	64.35	47.67	47.67	64.35
Vertical forces at base level (with LL) (V_b'=P_l'+V_o+V_4)	744.59	kN/m	1005.19	744.59	744.59	1005.19
Resisting moment about 'B' due to P_l' (MP_l'=P_l' · L_p')	251.84	kNm/m	339.99	251.84	251.84	251.84
Resisting moment about 'B' (with LL) (M_{rb}'=VM_o+VM_4+MP_l')	1569.34	kNm/m	2237.61	1657.49	1657.49	1657.49
Overturning moment about 'B' (with LL) (M_{ob}'=HM_o+HM_2+HM_{sb})	233.75	kNm/m	360.53	244.04	233.75	360.53
Resultant resisting moment about 'B' (M_{resb}'=M_{rb}'-M_{ob}')	1335.59	kNm/m	1877.09	1413.45	1423.74	1296.96
Location of resultant force from 'B' (t_b'=M_{resb}'/V_b')	1.79	m	1.87	1.90	1.91	1.29
Eccentricity at base of the abutment (e_b=L_r/2-t_b')	0.71	m	0.63	0.60	0.59	1.21
Limit of eccentricity (e_b'=L_r/4 for strength , L_r/6 for service)	1.25 , 0.83	m	1.25	1.25	0.83	1.25
Fulfilment of eccentricity criteria (e_b' > e_b)	Yes	-	Yes	Yes	Yes	Yes
Efective width at base (B_b'=L_r-2e_b)	3.59	m	3.73	3.80	3.82	2.58
Bearing stress at base (σ_v=V_b'/B_b')	207.55	kPa	269.14	196.12	194.70	389.53
Total bearing resistance (σ_{tot}=σ_v+$\Delta\sigma$)	255.22	kPa	333.49	243.78	242.37	453.88
Bearing capacity (factored) (Q_{fu},Q_{fs} - given in table 3.2)	718 , 335	kPa	718.00	718.00	335.00	718.00
Fulfillment of bearing capacity criteria (Q_{ru},Q_{rs} > σ_{tot})	Yes	-	Yes	Yes	Yes	Yes

As shown in Table 3.12, total bearing resistance under serviceability comes closer to the limit, but all conditions including critical loading is comfortably fulfilled by external design.

3.3 Internal Stability of the Abutment

Internal stability analysis commences from dimensions provided by the external stability analysis. Tensile strength and pullout resistance required for handling tensile stress at each reinforcement level defines the vertical spacing, length of reinforcement and type of reinforcement required for successful strain mobilization in reinforcements amongst active and reinforced soil zones.

Pullout resistance factor ' F_{pull}' and reinforced lateral coefficient 'K_r' are introduced additionally in the design. Critical failure plane assumed for internal failure is a coherent gravity plane as explained in Chapter 2.3.2. Point of deflection of the critical failure plane in Figure 3.3 is at '$0.2H_t$ = 1 m' from the abutment toe, according to simplified critical failure assumption mentioned in Craig (2004) and Gofar (2008). Dimensions are shown in Figure 3.3 - left.

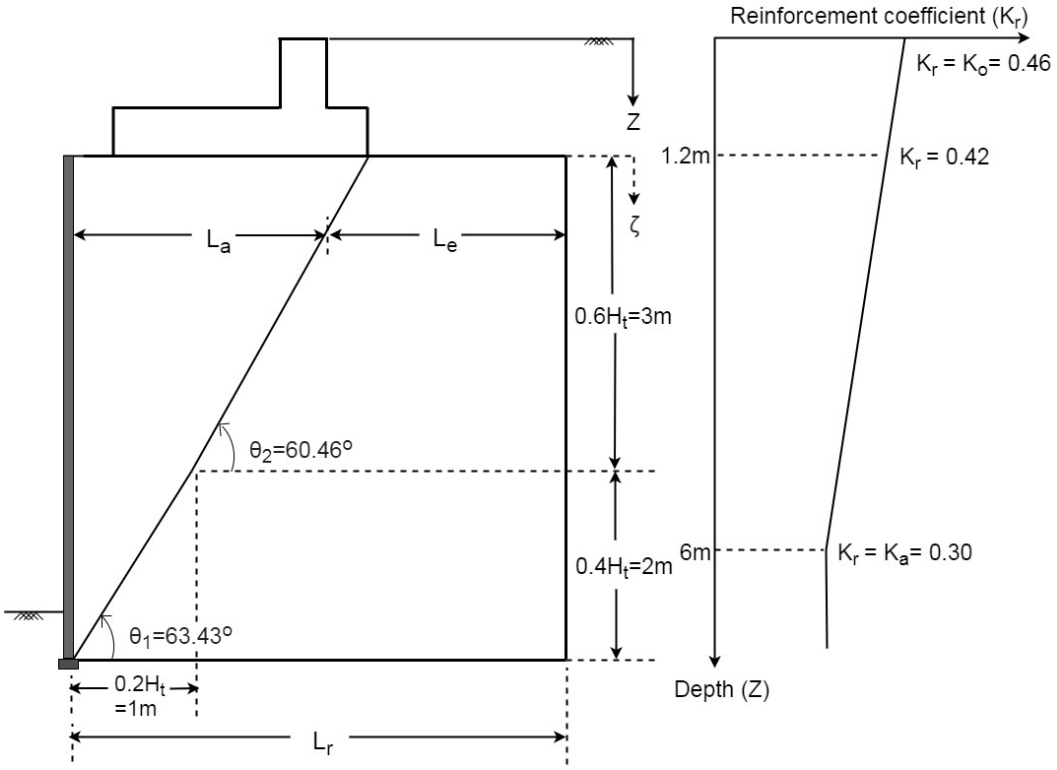

Figure 3.3: Coherent gravity critical failure plane and variation of reinforcement coefficient 'K_r' with depth

Pullout resistance factor 'F_{pull}' is assumed as 'F_{pull}=0.8·tan(ϕ_r)' according to (Holtz et al. (1997), p. 326), which is a conservative assumption and a laboratory test as per ASTMD6706 (2013) standard should be considered for a more realistic value. Also according to (Craig (2004), p. 270), 'K_r' is assumed to vary from coefficient of lateral earth pressure at-rest condition 'K_o'

at top of the footing to active lateral earth pressure 'K_a' at 6 meters depth, varying uniformly. Variation of 'K_r' according to depth is shown in Figure 3.3 - right. Jaky's equation (K_o=1-sin(ϕ_r)) is used for estimating 'K_o'.

'Z' is depth measured from top of the spread footing and 'ζ' is depth measured from top of reinforced section. Total design length of reinforcement is a sum of length of reinforcement in active zone 'L_a' and embedment length 'L_e' as shown in Figure 3.3. Analysis for tensile stress is done at each reinforcement level.

According to (Holtz et al. (1997), p. 218), an initial thickness of 300 mm to 450 mm can be assumed for medium ground pressurizing equipment between 30 kPa and 60 kPa. 400 mm of initial vertical thickness is assumed for this case and is denoted by 'S_v' in Table 3.13. All lengths are in 'meters', stresses in 'kPa' and tensile force 'T_n' in 'kN/m' for Tables 3.13 and 3.14.

Table 3.13: Tensile force 'T_n' at each reinforced layer

Layer (n) (n)	ζ_n (m)	S_v (m)	H_t (m)	K_r -	σ_v (kPa)	σ_h (kPa)	$T_n = S_v \cdot \sigma_h$ (kN/m)
1	0.1	0.2	1.3	0.425	309.59	131.54	26.31
2	0.4	0.4	1.6	0.417	314.69	131.16	52.46
3	0.8	0.4	2	0.406	321.49	130.52	52.21
4	1.2	0.4	2.4	0.395	328.29	129.74	51.90
5	1.6	0.4	2.8	0.384	335.09	128.81	51.52
6	2	0.4	3.2	0.374	341.89	127.73	51.09
7	2.4	0.4	3.6	0.363	348.69	126.50	50.60
8	2.8	0.4	4	0.352	355.49	125.13	50.05
9	3.2	0.4	4.4	0.341	362.29	123.61	49.44
10	3.6	0.4	4.8	0.330	369.09	121.95	48.78
11	4	0.4	5.2	0.320	375.89	120.13	48.05
12	4.4	0.4	5.6	0.309	382.69	118.17	47.27
13	4.8	0.4	6	0.298	389.49	116.07	46.43

As shown in Table 3.13, depth 'ζ_n' is up to the middle of the respective layer 'n'. 'K_r' is according to Figure 3.3 - right and vertical force upon each layer 'σ_v' is calculated as 'σ_v=q+γ_r·H_t'. Similarly, 'q' is cumulative vertical force from the spread footing (including live loads). Thirteen layers are thus obtained and tensile force at each layer is shown by 'T_n' in Table 3.13

At each reinforcement level, embedment length 'L_e' is length of reinforcement beyond critical failure plane, required for resisting pullout force and to maintain internal stability of abutment against active failure. 'L_e' is a function of tensile force, vertical force and pullout resistance as shown in equation 3.2 (Holtz et al. (1997)).

$$L_e = \frac{T_n}{C \cdot \sigma_v \cdot \alpha \cdot F_{pull}} (FS_{int}) \tag{3.2}$$

As in equation 3.2, 'α' is scale correction factor and is assumed to be '1' in this case. 'C' is geometry factor and is '2' for geosynthetics contacting soil from both sides. 'FS_{int}' denotes 'factor of safety' for internal stability, for which a value of '1.5' is adopted. Length of reinforcement at active soil zone 'L_a' is calculated geometrically as shown in Figure 3.3.

Table 3.14: Length of reinforcement 'L_r' at each reinforced layer

Layer (n) (n)	ζ_n (m)	$\mathbf{T_n}$=$\mathbf{S_v} \cdot \sigma_h$ (kN/m)	σ_v (kPa)	$\mathbf{L_e}$ (m)	$\mathbf{L_{e(min)}}$ (m)	$\mathbf{L_a}$ (m)	$\mathbf{L_r}$=$\mathbf{L_a}$+$\mathbf{L_e}$ (m)
1	0.1	26.31	309.59	0.12	0.90	2.65	3.55
2	0.4	52.46	314.69	0.24	0.90	2.48	3.38
3	0.8	52.21	321.49	0.23	0.90	2.25	3.15
4	1.2	51.90	328.29	0.23	0.90	2.02	2.92
5	1.6	51.52	335.09	0.22	0.90	1.79	2.69
6	2	51.09	341.89	0.22	0.90	1.57	2.47
7	2.4	50.60	348.69	0.21	0.90	1.34	2.24
8	2.8	50.05	355.49	0.20	0.90	1.11	2.01
9	3.2	49.44	362.29	0.20	0.90	0.90	1.80
10	3.6	48.78	369.09	0.19	0.90	0.70	1.60
11	4	48.05	375.89	0.18	0.90	0.50	1.40
12	4.4	47.27	382.69	0.18	0.90	0.30	1.20
13	4.8	46.43	389.49	0.17	0.90	0.10	1.00

From values of tensile stress 'T_n' and vertical stress 'σ_v' at each level obtained from Table 3.13, length of embedment is then calculated as shown in Table 3.14. Total length of reinforcement 'L_r' is the sum of reinforcement length in active and embedment zone. Minimum embedment length however is stated as 0.9 meters by Holtz et al. (1997).

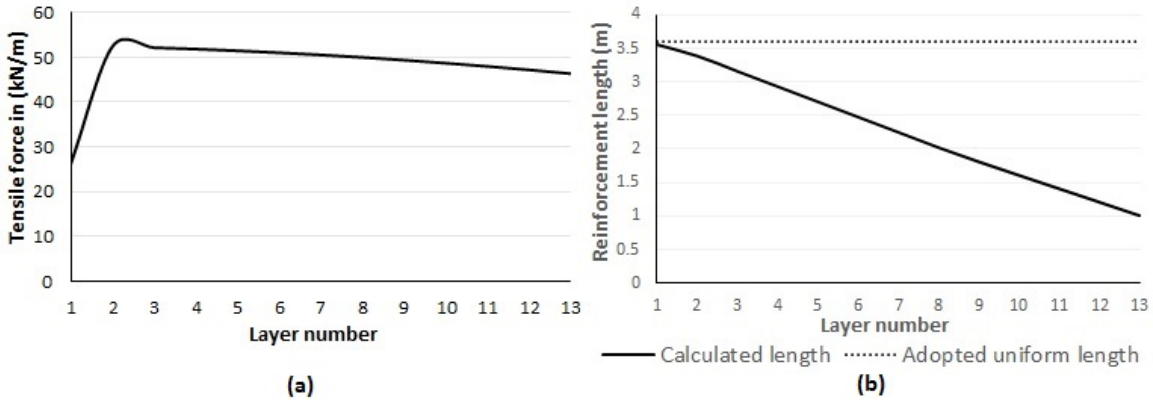

Figure 3.4: (a) Tensile stress in each layer by limit state design as per Table 3.13, (b) Calculated and adopted reinforcement length by limit state design as per Table 3.14

Results from Tables 3.13 and 3.14 are summarized in Figure 3.4. Lower value of tensile force for 'layer 2' as indicated in Figure 3.4 (a), is due to halved vertical spacing of reinforcement at the top layer.

As per Tables 3.13 and 3.14, length of reinforcement at top is 3.55 meters. This is mainly due to assumption that coefficient of lateral earth pressure varies from 'K_o' at road level to 'K_a' at 6 meters depth. For construction simplicity the highest reinforcement length is rounded off to first decimal, and thus a reinforcement length of 3.6 meters is adopted throughout abutment depth as indicated in Figure 3.4 (b).

Dimension of the spread footing and abutment according to internal and external limit state design performed, is shown as a schematic in-scale representation in Figure 2.7. First reinforcement layer lies 0.2 meters below spread footing and final layer lies 0.5 meters below depth of embedment. Design of facing, settlement analysis and seismic analysis (where applicable), are vital part of the design; but is not included in this portion of analysis. As shown in Figure 2.7, spread footing has a total height of 1.2 meters and abutment rises 4.5 meters above depth of embedment. According to the design, 15 layers of reinforcement (additional at top and bottom) for the 13 reinforced layers is achieved.

Working mechanism of the abutment depends upon mobilization of strength due to strain in reinforcement, which results from compaction at each layer (during and after construction). Settlement analysis, facing design and seismic design (whenever relevant) are thus important parts of a complete analysis. Drainage and erosion protection analysis also are vital for achieving strength and performance as per design.

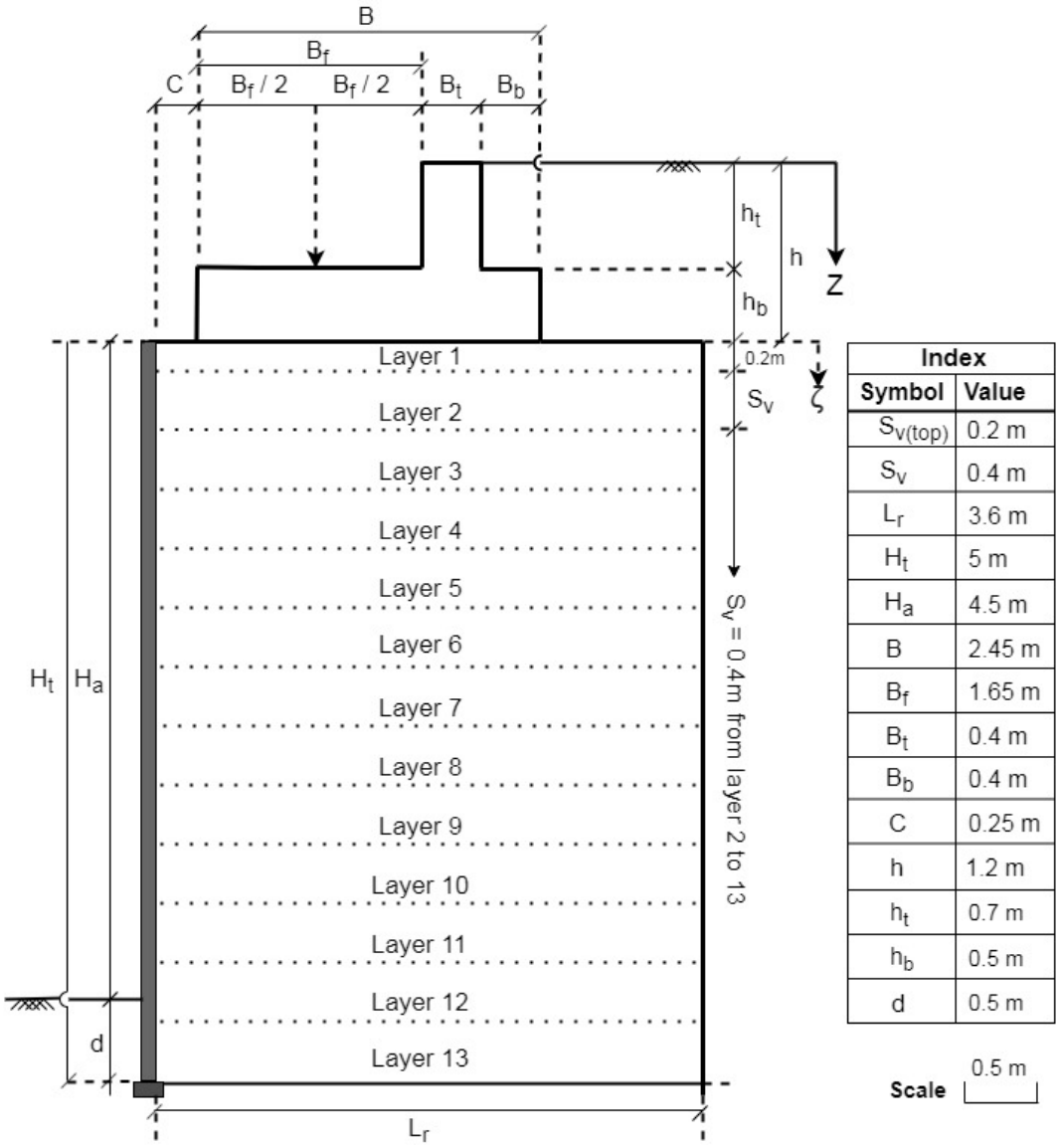

Figure 3.5: Final dimension of the abutment and spread footing by limit state design

Chapter 4

Numerical Modeling and Safety Analysis in PLAXIS 2D

Limit equilibrium design performed, analyzes strength of the abutment based upon pullout and tensile resistance of the reinforcement, abutment geometry and soil properties. Increased load bearing capacity of the abutment however, results from mobilization of strength due to strain in reinforcement and interaction of the reinforcement with soil. It is thus essential to study these behaviour of 'soil-reinforcement' interaction within numerical parameters that incorporate these behaviours. Soil considered in this design is 'gravelly sand' and reinforcement is 'polymeric geosynthetic', with 'cast in place concrete' for facing and spread footing elements.

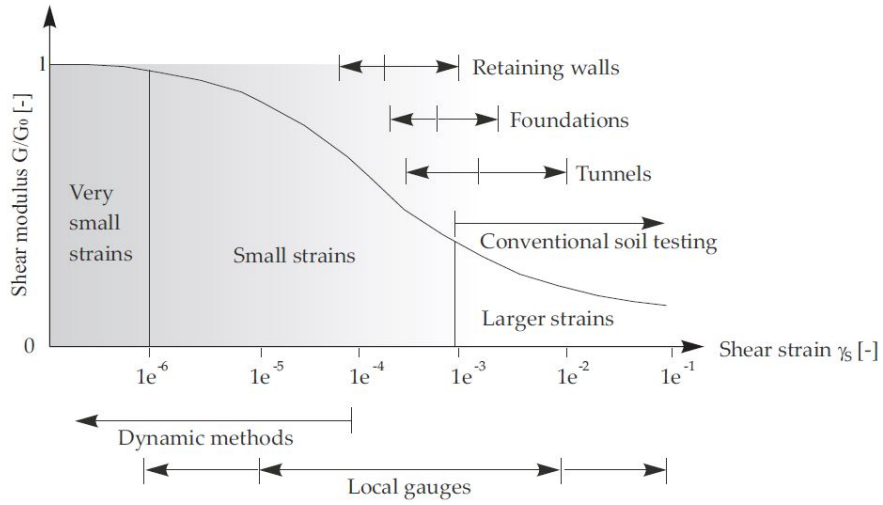

Figure 4.1: Characteristic stiffness-strain behaviour of soil (after Atkinson and Sallfors (1991)),PLAXIS (2019a)

Compression hardening and shear hardening behaviour of sand is most feasibly simulated

by the 'hardening soil model' in PLAXIS 2D. Moreover, stiffness behaviour during unloading and reloading of soil with respect to strain is more reliably emulated by 'hardening soil small' model (PLAXIS (2019b), p. 160), which is the chosen soil model for this design. As shown in Figure 4.1, non-linear dependency of 'small-strain soil stiffness' with strain magnitude is more distinguished in retaining walls. The design of abutment using reinforced soil is based upon principles of reinforced walls and hence the 'hardening soil small' model most accurately depicts its behaviour.

Results obtained from a numerical analysis is an outcome of interaction of the 'numerical soil and material models' with applied parametric conditions. Characteristics of the numerical model is vital to mention before using it in the context of its application. Brief characterization of the HS small model in context of static application and option of geogrid in PLAXIS 2D is abridged in next two sections (section 4.1 and 4.2), continuing with plastic analysis and safety analysis of the designed abutment (in section 3.3 and 3.4) respectively.

4.1 Hardening Soil small (in General/Static Application)

The HS small model builds upon strain dependency of HS model's isotropic elastic stiffness. The model principally conserves the material's small strain stiffness by constricting plastic strains under initial loads. Yield surface for a HS small model for a cohesionless soil is shown in Figure 4.2.

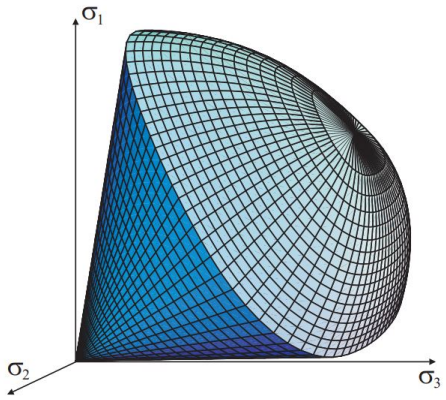

Figure 4.2: Cap and cone type yield surfaces in principal stress space for HS small model of sohesionless soil (Benz, T. (2006), P. 80)

Accurate simulation of non-linear decay of shear stiffness with shear strain at small strain section as shown in Figure 4.1 is the main reason for use of HS small soil model in this case.

Parameters used in 'Hardening soil small' model are similar to that of 'Hardening Soil' model - with additional stiffness parameters 'G_o^{ref}' and '$\gamma_{0.7}$', which represent reference shear modulus at very small strain ($\varepsilon < 10^{-6}$) and shear strain at which secant shear modulus 'G_s=0.72 G_o' as in (PLAXIS (2019b), p. 160). The relationship between 'G_o' and '$\gamma_{0.7}$' from a modified Hardin-Drnevich relationship as proposed by (Santos and Correia (2001)) is stated in equation 4.1.

$$\frac{G_s}{G_o} = \frac{1}{1 + a\left|\frac{\gamma}{\gamma_{0.7}}\right|} \tag{4.1}$$

Where, a = 0.385 and using '$\gamma = \gamma_{0.7}$' gives the aforementioned relationship of 'G_s = 0.72 G_o'. In the function used to reduce the shear modulus with shear strain, the shear strain used is dependent on loading history and can be generalised as mentioned in equation 4.2.

$$\gamma = \frac{3}{2}\epsilon_q \tag{4.2}$$

Where 'ϵ_q' is second deviatoric strain invariant and 'γ' is scalar shear strain parameter used in reduction function of shear modulus for HS small model according to Benz, T. (2006). Shear modulus reduction curve used in HS small model is shown in Figure 4.3.

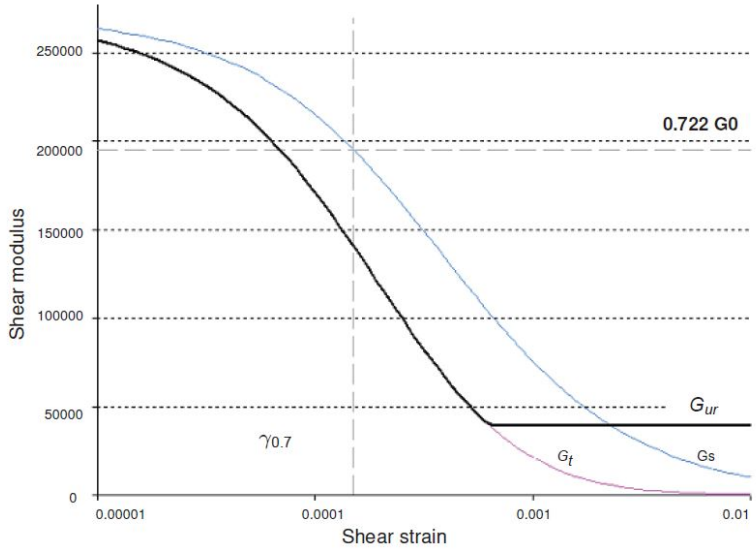

Figure 4.3: Secant and tangent shear modulus reduction curve (PLAXIS (2019a), P. 87)

Secant (G_s), tangent (G_t) and unloading-reloading (G_{ur}) shear modulus reduction curves are represented in Figure 4.3. Integration of secant modulus curve over the incremental shear strain gives the quasi-elastic tangent shear modulus (PLAXIS (2019a) p. 87).

The accumulation of strain in reinforcements after compaction is the mechanism of strength gain for the considered reinforced soil bridge abutment. Since drained condition is assumed to be applicable throughout all analysis and design in this case, the irrevocable strain lead to small but constant ratcheting (Benz, T. (2006)). This behaviour is assumed essential for mobilization of strain and consequently strength for the abutment considered in this case.

4.2 Geogrids in PLAXIS 2D

Another important component of reinforced soil bridge abutment is the soil reinforcement. PLAXIS 2D has 'geogrid' element, which simulates the orthotropic behaviour of soil reinforcement under loading conditions. Parameters to be defined for the geogrid element are 'EA_1' and 'EA_2', where 'E' defines material tension stiffness along cross sections 'A_1' and 'A_2' according to local axes of the geogrids (PLAXIS (2019a), p. 216). Formulation of relationship between tensile force and strain in geogrid, as described in (PLAXIS (2019a), p. 217) is evinced in equation 4.3.

$$\begin{bmatrix} N \\ H \end{bmatrix} = \begin{bmatrix} EA_1 & 0 \\ 0 & EA_2 \end{bmatrix} \begin{bmatrix} \varepsilon \\ \varepsilon_H \end{bmatrix} \tag{4.3}$$

'N' and 'ε' denotes tensile force and strain upon geogrid in equation 4.3. 'H' and 'ε_H' are hoop force and hoop strain respectively. Since plain strain condition is assumed to be applicable in the limit equilibrium design portion , '$H = \varepsilon_H = 0$' in our case. Tensile force and strain relationship for this case can then be written as in equation 4.4.

$$\begin{bmatrix} N \\ 0 \end{bmatrix} = \begin{bmatrix} EA_1 & 0 \\ 0 & EA_2 \end{bmatrix} \begin{bmatrix} \varepsilon \\ 0 \end{bmatrix} \tag{4.4}$$

Cross sectional area along both axes of the geogrid (A_1 and A_2) are assumed to be the same. It results to a singular value for 'EA' governing the 'stress-strain' behaviour in the geogrids. Interface properties are used to simulate the 'pullout resistance' behaviour of the 'soil-geogrid' interface in this case.

4.3 Abutment Model and Plastic Analysis with PLAXIS 2D

Initial ground condition for the construction of abutment is assumed to be a slope of 'backfill soil', at an angle of '$\beta = 29.68^o$' with the horizontal. Top ground elevation of the slope is assumed to be the same as top level of the connecting road, 5.70 meters above the lower ground. Embedment depth of the abutment is assumed to be excavated from the toe of the initial slope. Dimensions of the abutment is according to the limit state design performed previously (as per Figure 3.5), according to which excavated slope commences after a horizontal excavation equal to reinforcement length (L_e=3.6m), at an angle of '$\beta^{'} = 29.61^o$' to the top level.

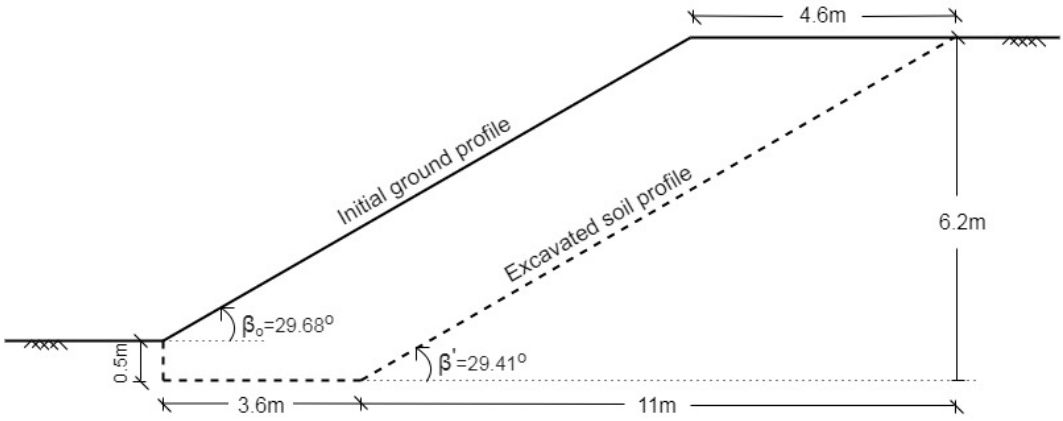

Figure 4.4: Initial and excavated ground profile for abutment construction as per Table 3.14

As shown in Figure 4.4, slope of both initial ground profile and excavated soil profile are assumed to be below 30 degrees with horizontal, so as to ensure stability in initial conditions (as angle of friction for backfill soil is 30 degrees). Parameters according to 'Hardening Soil small' model for reinforced soil and backfill soil are shown in Table 4.1 and Table 4.2 respectively.

Table 4.1: Parameters for reinforced soil (Hardening Soil small' model)

γ (kN/m3)	ϕ' (^{o})	c' (kPa)	v_{ur} -	E_{50}^{ref} (MPa)	E_{oed}^{ref} (MPa)	E_{ur}^{ref} (MPa)	m -	p_{ref} (kPa)	K_o^{nc} -	R_f -	G_o^{ref} (Mpa)	$\gamma_{0.7}$ -
17	33	5	0.2	12	16	60	0.75	100	0.46	0.9	168	0.0001

Table 4.2: Parameters for backfill soil ('Hardening Soil small' model)

γ (kN/m3)	ϕ' (^{o})	c' (kPa)	v_{ur} -	E_{50}^{ref} (MPa)	E_{oed}^{ref} (MPa)	E_{ur}^{ref} (MPa)	m -	p_{ref} (kPa)	K_o^{nc} -	R_f -	G_o^{ref} (Mpa)	$\gamma_{0.7}$ -
16	30	5	0.2	12	16	60	0.75	100	0.46	0.9	168	0.0001

Concrete used for facing element is modelled as a linearly elastic material with modulus of elasticity (E'=50 GPa assuming high strength concrete) and poisson's ratio (v'= 0.15). Material property of geogrid according to maximum tensile stress calculated in Table 3.13, and (Holtz et al. (1997), p. 435) is taken as $EA_1 = EA_2 = 1000$ kN/m.

The model follows the dimensions obtained from the limit state design and starts with an initial stage of stable excavated slope, excavated as per dimensions in Figures 3.5 and 4.4. Working principal behind the model is the use of 'Hardening Soil small model', to simulate mobilization of strength due to small strain. The fact that settlement inevitably occurs during construction and compaction phase of such soil structure is represented in the model - by utilizing large strain and small strain parameters during staged construction. Governing principle behind the design is that, small strain is allowed to accumulate throughout all stages of construction as it is essential for mobilization of strength in reinforcement. It is also noteworthy that the model without small strain parameter (Hardening Soil model) was previously tried for the abutment model, but the soil structure disintegrated before loading stage was reached. It emphasizes the role of small strain behaviour in simulating strength mobilization in the designed abutment. It is also important to state that settlement is inevitable and is in fact expected for construction of this type of structure. Estimated settlement is then incorporated in the design and is achieved by pre-loading the structure with equivalent loading, in field construction.

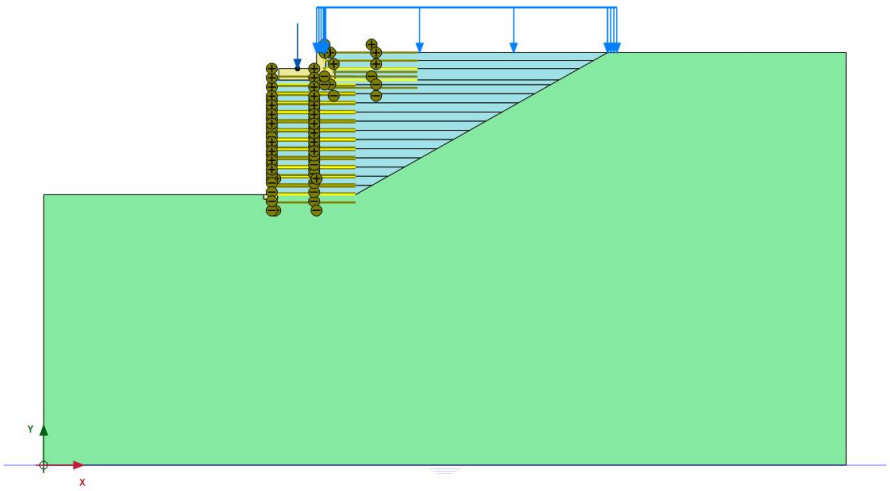

Figure 4.5: Equivalent ladings and model geometry as per limit state design (in PLAXIS 2D)

As shown in Figure 4.5, the 'abutment model' follows the limit state design dimensions as illustrated in Figure 3.5. Initial stage is a depiction of 'after excavation profile' as per Figure 4.4,

and all following phases from 'Phase 1' to 'Phase 13' represent addition of individual reinforced layers as per limit state design. Spread footing and the soil layer behind the spread footing are added sequentially from phases 14 to 16. All bridge loads are activated during 'Phase 17', which is the final calculation phase. Loads added are of same values as considered during limit state design (as per Table 3.3) and action of live loads from bridge are ignored for this model. However, equivalent live loads from connecting road portion are included.

Net dead load from the bridge superstructure is represented by a point dead load of 140 kN/m and equivalent live load in connecting road is represented by a uniformly distributed load of 22 kPa, (as per loads considered in limit state design) in the model. The soil boundary for the model is assumed as a rectangle extending 20 meters vertically and 35 meters horizontally, with the abutment model lying at the top middle portion of the boundary as shown in Figure 4.5. Five nodal points (three below the spread footing and two at the bottom corners of the abutment) are considered for analysing stress-strain behaviour at critical points of the abutment.

Due to equivalent live loads at the connecting road portion of the abutment, additional deformation which was not anticipated in the limit equilibrium design; is observed with the finite element analysis as shown in Figure 4.6. A complex failure geometry is seen to be developed and the geogrids at the top portion show deformation due to this condition. It should also be noted that safety calculations could not be conducted for all 17 phases with this condition as the soil structure failed upon load activation in safety calculation of phase 17 (discussed in section 4.2).

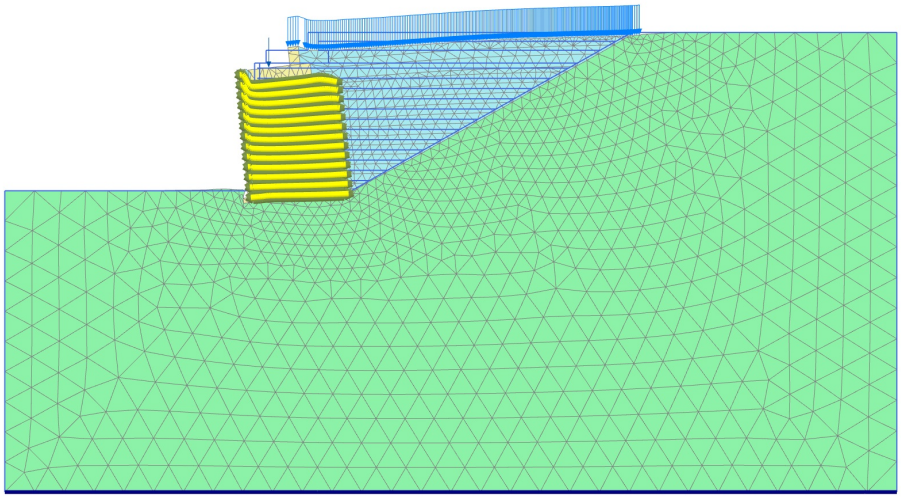

Figure 4.6: Deformed mesh without 'added geogrids at the top' for the final plastic phase (in PLAXIS 2D)

To solve this issue which did not surface in limit state design, additional geogrids at the por-

tion behind the spread footing is added. The length of the lowermost of the three additional geogrids behind the spread footing is same as the rest of the geogrids involved in abutment below it. Uppermost two geogrids are added to equate the length of the added geogrids and are added according to the geometrical shift of the rear portion of the spread footing (i.e. at the corner points of the rear portion) as shown in Figure 4.7.

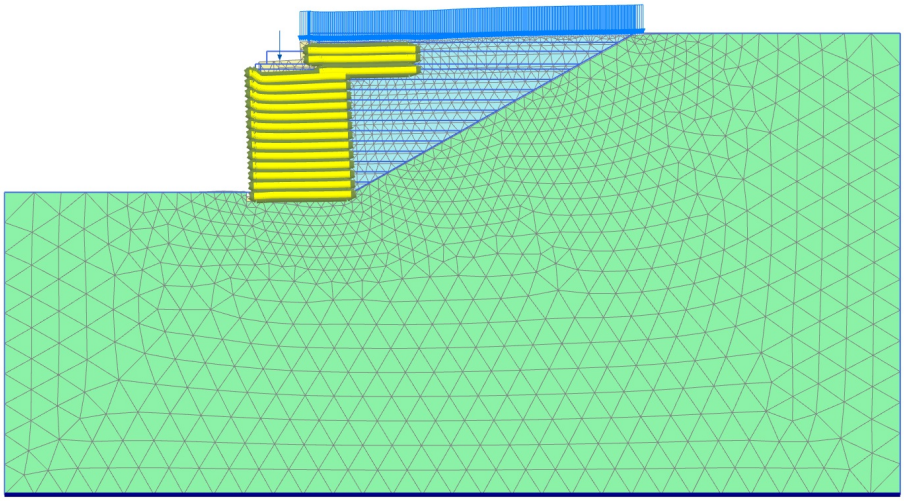

Figure 4.7: Deformed mesh with 'added geogrids at the top' for final plastic phase (in PLAXIS 2D)

Phase parameters for all phases from 'Phase 1' to 'Phase 17' are same, with only difference being activation of structures and loads. For each layer; lower geogrid, interfaces and soil portion are activated before proceeding to the next layer. Undrained behaviour is ignored for all these phases, as water table is considered to be sufficiently below the abutment base. Displacement is reset to zero for each phase, as additional soil material is filled in practical construction for adjusting settlement during construction and compaction. Small strain behaviour is however - not reset to zero and is allowed to accumulate throughout the phases, as it is essential for mobilization of strength in the reinforcements. Similar values for general parameters and deformation parameters as mentioned, is applied for all seventeen phases. Updated mesh and accumulated small strain are important parameters for working mechanism of the model, and are incorporated in deformation parameters for all phases.

Objective of the model from a practical perspective is to gain a value of settlement, so as to use those values for attaining those settlements during pre-loading phase; thereby eliminating difference in elevation between 'connecting road' and 'bridge superstructure' (during actual operation). Stiffness parameters of geogrid (EA_1 and EA_2) controls the tensile failure mode and

interface strength is used to represent 'pullout resistance' behaviour of the geogrids. A rigid interface strength of 'R_{inter}=0.8' is assumed for the model - with all geogrids embedded with the facing (assuming total rigidity in 'geogrid-facing' connection).

Deformed mesh after addition of top additional geogrids and activation of all structures and loads in 'Phase 17 (load activation phase / final phase)', is shown in Figure 4.7. It is observed that the abutment has slightly tilted towards the lower ground. This concurs with the limiting eccentricity calculation during limit state design, where limiting eccentricity had the lowest factor of safety. This is due to the slope action of backfill, rigid connection with facing and force transfer to some extent from reinforced soil layer to the facing. In principle however, facing element is not supposed to resist any lateral load. In practical construction, a granular drainage enhancing material is packed between facing and reinforced layer. Lateral displacements of reinforced soil layer is adjusted with this granular fill during compaction, at each layer in live construction.

Deformation of the topmost geogrid under the spread footing, distinctively has the most deformation after load activation as shown in Figure 4.7. The extent of settlement anticipated after loading, should however be achieved during 'pre-loading and compaction' for attaining a seamless transition between bridge and the connecting road.

While considering settlements occurring at different phases, 'construction completion phase' (Phase 16) and 'load activation phase' (Phase 17) are of higher significance. Maximum deformation at construction completion phase' occurs along the 'rear fill' of spread footing (additional reinforcements are mobilized specifically to serve this purpose). Nodal point with maximum deformation for 'load activation phase' is invariably - 'the toe of spread footing' (considering material stiffness and loading geometry).

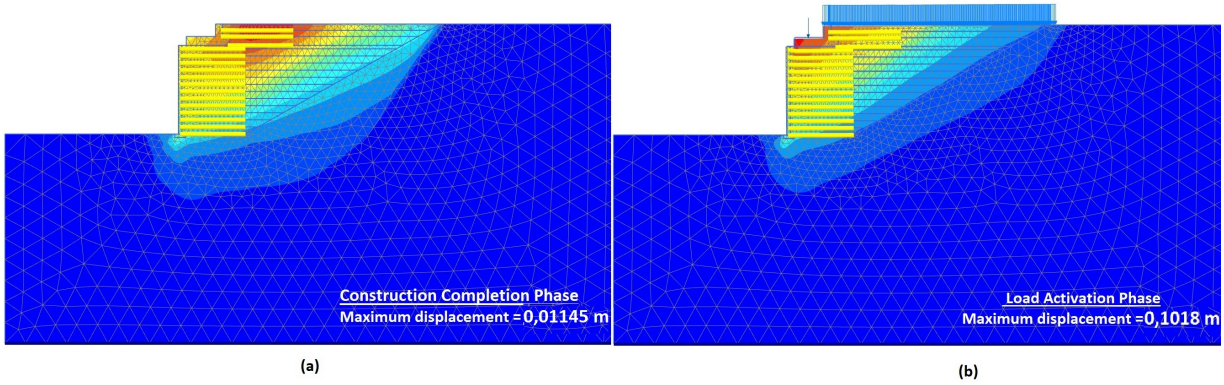

Figure 4.8: (a) Total displacement for construction completion phase 'Phase 16' (b) Total displacement for load activation phase 'Phase 17' (in PLAXIS 2D)

Figure 4.8 (a) and (b) show total displacements for final two stages of the abutment model (construction completion and load activation). A maximum settlement of 0.01145 meters is observed after construction is complete and 0.1018 meters is observed after all bridge loads are activated.

Geogrids in this model are designed according to assumed 'critical failure plane', where maximum tensile force is supposed to occur. Ideally for a geogrid with an infinite length, axial tension upon the geogrid at a certain reinforced layer should have its maximum at the point where it intersects the 'critical failure plane'. In this case however, geogrid is rigidly attached to the facing - which results in maximum tensile force at the connecting point between geogrid and the facing.

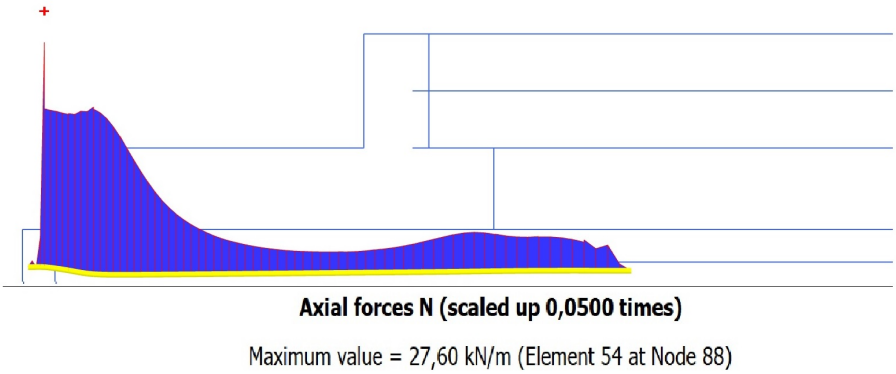

Figure 4.9: Axial force at topmost geogrid in the abutment (in PLAXIS 2D)

Figure 4.9 is an axial force diagram for the geogrid which is 0.2 meters below the spread footing (topmost geogrid). It can be observed from the same diagram that the maximum axial force of 27.60 kN/m occurs at the rigid connection between the geogrid and facing. A subsequent rise is also observable at the rear portion of the geogrid (beyond back corner of spread footing). Which is due to occurrence of maximum tensile zone (critical failure plane) at that region. Tensile stress at each layer of geogrid is also calculated previously in limit state part of the design. It is of peculiar significance that tensile stress at the first geogrid as calculated in Table 3.13 is 'T$_n$= 26.31 kN/m' which is close to the value obtained from the axial force diagram 'N$_{max}$ = 27.6 kN/m' in Figure 4.9.

Since 'Hardening Soil small' model is used as soil model, it is specially advantageous to study the 'cap hardening' and 'shear hardening' behaviour in the abutment model. Shear hardening specifically indicates that shear failure is more prominent along that envelope. Shear hardening

point along with 'failure points' and 'tension cut-off points' are shown in Figure 4.10.

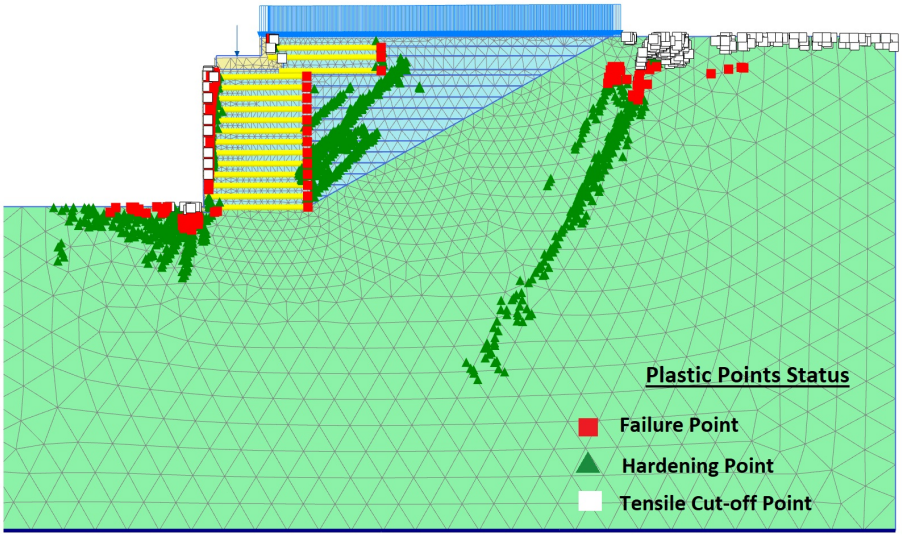

Figure 4.10: Plastic points status in the static abutment model (in PLAXIS 2D)

In Figure 4.10, red squares represent 'failure points', indicating surface failure at that point. In this case, it represents 'pullout failure' or slippage of the geogrid. It can be observed from Figure 4.10 that the geogrid slips at almost every level to a certain extent , and that the mode of failure for geogrids is slippage (and not tensile failure). In the same figure, 'tensile cut-off points' indicated by white squares are seen at the backfill soil surface (behind equivalent live surcharge of the bridge). Tension cut-off points have practical significance during construction, as additional compaction and soil strengthening will be needed in this region to avoid tension cracks and related failures.

A hardening point in HS small model is a point where the stress state has reached the maximum mobilized friction angle (PLAXIS (2019b), p.356) Shear hardening points are shown by green triangles in Figure 4.10. Four distinct groups for shear hardening can be seen in the figure. Shear hardening points along the front face of the abutment and at lower ground level of the abutment are direct results from the activation of bridge loads. Two inclined lines are seen to be formed by the shear hardening points - one at the reinforced soil region (rear to geogrids) and another at backfill soil region (below the accumulated tension cut-off points). It is interesting to observe that geogrids have prevented the formation of shear hardening points in the reinforced region. Shear hardening points have formed a line at an angle of almost 45 degrees with the horizontal in the reinforced soil zone and about 60 degrees at the backfill soil zone. These lines

indicate the weakness plane for a possible slope failure along reinforced and backfill soil zones.

Since abutment modeling was done without added reinforcements at the top in the beginning, it is relevant to study the difference the added reinforcements make in the formation of shear hardening points and other relevant plastic points. Relative depiction of plastic points for cases with and without added reinforcements at the top is illustrated in Figure 4.11.

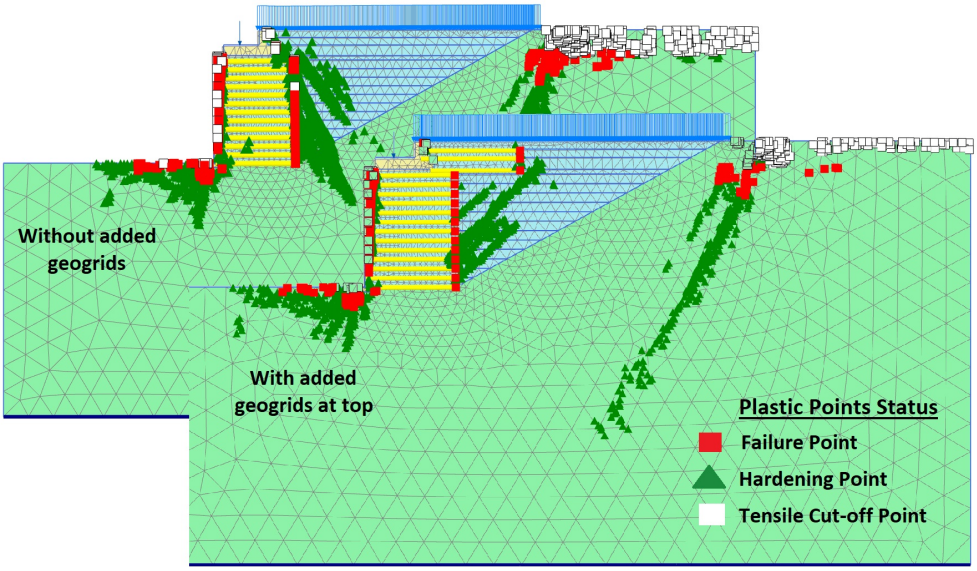

Figure 4.11: Relative depiction of plastic points with and without added reinforcements at the top (in PLAXIS 2D)

It is observed in Figure 4.11 that failure mode with added reinforcements at the top still remains as - slippage, and no failure is observed along the length of the geogrids or in the reinforced block, as seen from both illustrations. It is however distinct that shear hardening points behind the reinforced section has completely altered with added reinforcements at the top. In case without added reinforcements at top, the shear hardening points accumulate at the back corner of the spread footing and progresses downward at an angle less than 45 degrees with the vertical (approximately). In contrary, when added reinforcements at the top, shear hardening points generate at the back corner of the reinforced section of the abutment and develops upwards at approximately 45 degrees. Number of shear hardening points are also significantly reduced with added reinforcements at the top and it manifests the importance of the modified design - altering from what was obtained with limit equilibrium design.

In addition, the tensile cutoff points behind the equivalent traffic loads in backfill soil region shown in Figure 4.11, is significantly reduced with the use of added reinforcements at the top. It asserts the importance of the added reinforcements for tension related failure mechanisms at

the connecting road portion.

4.4 Safety Analysis with PLAXIS 2D

At each construction and loading stage, it is important to analyse the safety aspects of every designed structure. Conventionally, safety analysis involves calculation and analysis of 'driving forces' and 'resisting forces' against failure. How the failure is supposed to occur, and how the forces and failure modes involved in these mechanisms will be approached, depends upon the type of structure being analyzed. Limit equilibrium design performed in the previous chapter, compared failing forces and stresses for each considered failure modes against its limiting values - in differing states of criticality.

Janbu's 'Slope Stability Charts' and 'Generalized Procedure of Slices' as described in (Janbu (1968)), are widely used methods for analysis of slope stability. Force equilibrium and moment equilibrium analyses are also used widely in numerous modified forms depending upon their utility. While performing safety analysis using finite element method, there are two general approaches of analysing safety. First one is by increasing the gravity loads and second one is by reducing the strength parameters of the soil as explained in (Duncan (1996)). Reduction of strength approach is pursued by PLAXIS 2D for safety analysis, which is used for the safety analysis of the designed abutment in this case.

For soil structures, definition of 'Factor of Safety' is more appropriately defined as a ratio of 'maximum available shear strength' to 'shear strength needed for equilibrium'. Using 'c' and 'ϕ' as strength parameters and 'σ_n' as actual normal stress component, factor of safety as defined in (PLAXIS (2019c)) is obtained as mentioned in equation 4.5.

$$FoS = \frac{c - \sigma_n \cdot \tan\phi}{c_r - \sigma_n \cdot \tan\phi_r} \tag{4.5}$$

As per equation 4.5, 'c_r' and 'ϕ_r' are reduced strength parameters that suffice equilibrium state. A total multiplier is introduced for this purpose in PLAXIS which is termed as 'ΣM_{sf}' and is a ratio of actual and reduced 'c' and 'tanϕ' ($\Sigma M_{sf} = c/c_r = \tan\phi/\tan\phi_r$).

For simulating safety analysis in the designed abutment model, a safety phase is added to each of the seventeen phases shown in Figure 4.5. Loading type is set to 'incremental multipliers' with a value of '0.1'. Deformation parameters are similar to that of plastic analysis phases.

Undrained behaviour is ignored and strain is reset to zero at the end of each phase - with small strain allowed to accumulate through all phases. It allows similar 'strength mobilization due to small strain accumulation' principle to remain valid as in plastic analysis. As a result, reduction of strength parameters ('c' and 'tanϕ') is performed from a centralized perspective for both plastic and safety analysis.

Since interfaces are used along the 'soil-geogrid' boundaries, its strength is reduced in the same way as the strength of soil (according to sequential increase of 'ΣM_{sf}' multiplier). Purpose of performing a 'ϕ-c reduction' analysis such as this, is mainly to observe the value of 'M_{sf}' multiplier for each phase and to obtain the most applicable failure mechanism in the form of 'incremental displacement diagram' for the most critical loading phase. A sufficiently fine mesh is required for accurate depiction of safety factors in safety analysis, and 'very fine mesh' is used in this model (for both - plastic and safety analysis) for securing accuracy of the calculations.

In safety calculations done for the abutment model, 'Hardening Soil small' model is used as soil material. But, all advanced soil models behave as a standard 'Mohr-Coulomb' model in safety analysis. A constant stiffness calculated at the beginning of each phase remains unvaried till the end of that phase. Stress dependent stiffness and hardening behaviour of the soil are hence excluded from the calculations as described in (PLAXIS (2019b)).

An incremental displacement diagram ($|\Delta u|$ diagram) for the 'load activation phase' of safety analysis, shows the most applicable failure mechanism for the model. The 'incremental displacement diagram' is shown relative to the 'plastic points status' diagram (during plastic analysis - Figure 4.10) in Figure 4.12. The two figures are shown relative to each other due to their relevance in development of failure mechanism in the reinforced soil region.

Although 'Hardening Soil small' model behaves as a standard 'Mohr-Coulomb' model during safety calculations, it is interesting to observe that the shear hardening points behind the geogrids and at the toe of the abutment (represented by green triangles), matches exactly with the critical failure mechanism presented by the 'incremental displacement diagram' of the final safety calculation phase.

Actual values of the incremental settlements in Figure 4.12 is unimportant and the failure plane is the main object for examination in this case. It is observed that the critical failure mechanism develops along the shear hardening points. A 'bearing capacity type failure' is also observed at the toe region. A somewhat less critical tensile failure mechanism is also deemed

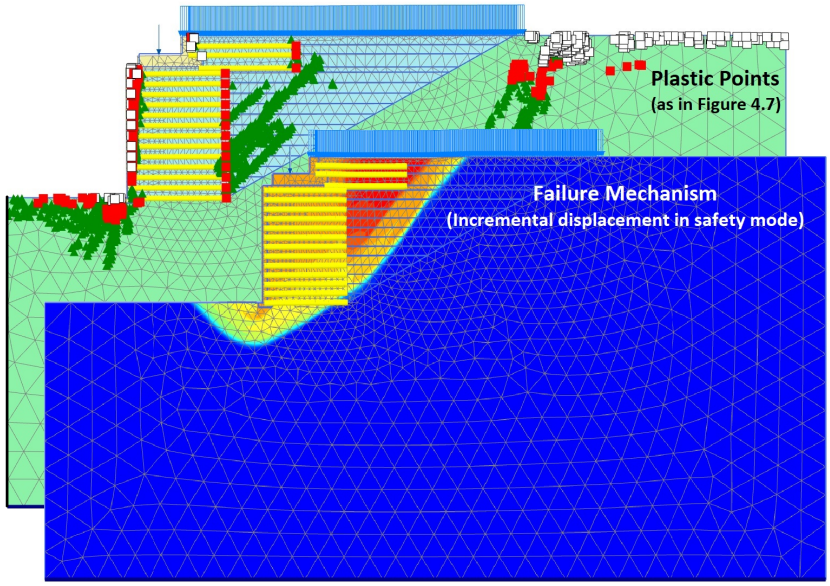

Figure 4.12: Relative depiction of 'most applicable failure mechanism' with 'shear hardening points' (in PLAXIS 2D)

possible along the lowermost four geogrids. From the relative comparison of the shear hardening points and critical failure mechanism, it is however clearly discernible that a failure mechanism along the shear hardening points is applicable, according to the performed calculations.

Determination of factor of safety is another main objective of the safety analysis performed. A stable value of 'ΣM_{sf}' is accepted as a factor of safety for a particular safety phase. A value of factor of safety for each phase can also be acquired from the 'calculaion information' option in "Project' tab of PLAXIS 2D - results window. Safety calculations involve additional steps and it results to additional displacements. These displacements do not have any physical significance and are only used to determine a stable value of 'ΣM_{sf}'.

Figure 4.13 shows a plot of displacements incurred during safety analysis and 'ΣM_{sf}' multiplier. The lowermost red line denotes the 'load activation phase' of the model, which is the final computational phase. It is indicated by the 'red line' that factor of safety for the final stage of the model is '1.3'. Calculation phases occurring before the load activation show a maximum factor of safety up to '2.2'. It is evident that the phase where all bridge loads are activated - is the most critical phase for the structure. But it is also noticeable that construction of 'layer-6' from the top reinforced layer (as per Figure 3.5) is the most safe layer according to the analysis. The 'layer-6' lies almost at the middle depth of the abutment and also implies that the reinforced layers below it aids in stability up to this point in the abutment model.

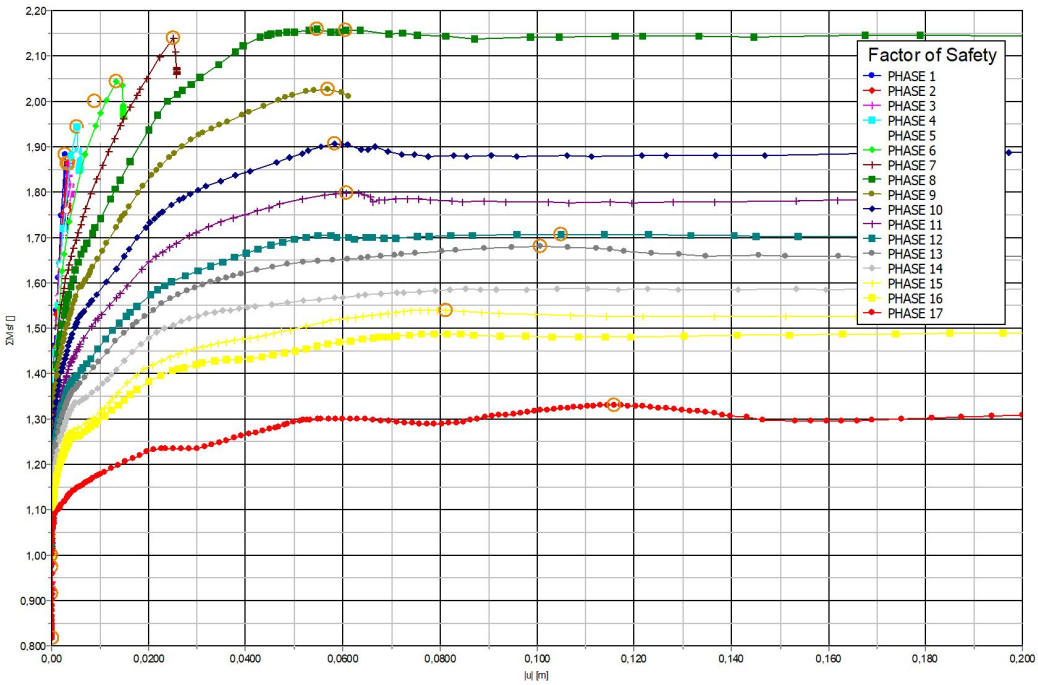

Figure 4.13: Diagram presenting 'Factor of Safety' for all seventeen phases of the model (in PLAXIS 2D)

These values emphasize the importance of compaction up to design level and refilling the settled depth at each layer, as strain is the mechanism by which the abutment gains strength - but only to the designed extent. For case of this abutment model, a settlement of about 10 cm is anticipated during loading actions (as in Figure 4.8) in the abutment. Physical meaning of this value is that, after construction phase is complete and all settlements involved in those phases are rectified, a further pre-loading is necessary for settling the abutment 10 cm more, for bringing its level down to the connecting road level.

Chapter 5

Analytical Seismic Design

Geosynthetically reinforced bridge abutments are deigned for use as sub-structures in a transportation system, and are often used in seismically active areas. Behaviour of the abutment in seismic conditions have vital physical and economic consequences, and are discussed and analysed in this Chapter.

During a seismic activity, additional transient dynamic pressures are induced in addition to the static pressures. Seismic response of a reinforced soil bridge abutment depends upon numerous aspects such as soil properties, nature of input wave motions, inertial and flexural response, interaction of structural components involved in the abutment and environmental conditions around the abutment, among many other variables. Inherent variability and uncertainty of these phenomena makes it a very complex process to analyse all seismic aspects accurately (Kramer (1996)). Simplified analyses that make various assumptions about these parameters are often used for seismic analysis, and a similar combination of simplified approaches is considered for the seismic analysis of the abutment designed in Chapter 3.

It is assumed that the abutment considered in this analysis behaves as a yielding structure and can move sufficiently for developing active and passive conditions. In this specific case however, the backfill soil region of the abutment is assumed to be in active state. A conventional pseudo-static approach as explained in Seed and Whitman (1970) and Kramer (1996) suggest that the total active pressure acting upon a structure in a seismic condition (P_{AE}), is a sum of active static pressure (P_A) and active dynamic pressure (Δ_{PE}) as shown in equation 5.1.

$$P_{AE} = P_A + \Delta P_{AE} \tag{5.1}$$

For a typical analytical seismic design, a maximum ground acceleration is applied to the centre of gravity of the structure, and the design ensures that the structure withstands additional force of this vibration - within a specified factor of safety (Au-Yeung and Ho (1995)). Dynamic forces are maximum near the natural frequency of the structural system (when there is no influence of external forces and wave damping). Increased residual pressures may remain in the structural system after a strong seismic activity and a parameter of uncertainty has to be accounted for in the seismic safety considerations as described in Steedman and Zeng (1990) and Whitman (1990).

The seismic design of the abutment considered in this Chapter is based upon effective stress approach from Geotechnical Division NTNU (2016) and pseudostatic approaches according to Mononobe and Matsuo (1929), Okabe (1926), NS-EN 1998-5:2004+NA:2014 (1998), Kramer (1996) and Christopher et al. (1990). Limit equilibrium design obtained from Chapter 3 and failure criteria obtained from Chapter 4 are also integrated into the design.

5.1 Methods and Code used in the Design

The design is based upon the pseudo-static approach that accounts for inertial forces, dynamic forces and static forces acting at different portions of the abutment. The method of analysing internal and external stability of the abutment separately, is continued in this section. It is assumed as mentioned in Kramer (1996) that the dynamic forces act at the back layer of the reinforced section and inertial forces act within the reinforced zone, in addition to static forces. 'Mononobe-Okabe' method is used for calculating dynamic forces and inertial forces are calculated from Christopher et al. (1990). 'Eurocode 8'(NS-EN 1998-5:2004+NA:2014 (1998)) is followed for parameters required for the design. Equations and parameters involved in the design is discussed before their application.

5.1.1 Mononobe-Okabe Method

A pseudo-static approach developed from works of Okabe (1926) and Mononobe and Matsuo (1929) is popularly known as Mononoke - Okabe (M-O) method. The method is an explicit expansion of static Coulomb theory to pseudo-static conditions Kramer (1996). The method was originally developed for dry and cohesionless soil.

The method assumes that soil involved is a dry and cohesionless material. Maximum shear strength is assumed to be mobilized at the triangular soil wedge behind the wall at the point of failure. It is also assumed that the wall and soil behave as a singular unit and shear waves propagate at infinite speed resulting in uniform acceleration throughout the soil wedge (Au-Yeung and Ho (1995)).

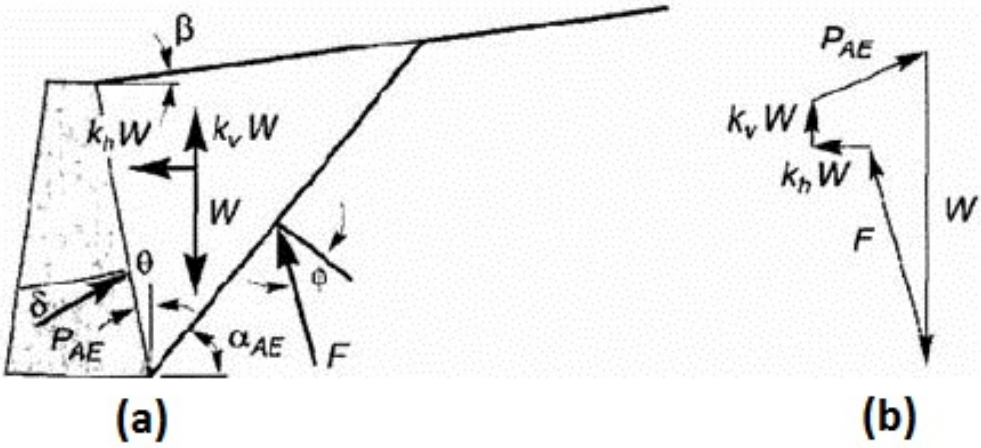

Figure 5.1: (a) Forces acting on active wedge in M-O analysis ,(b) Force polygon on active wedge (Kramer (1996))

As shown in Figure 5.1, acting forces and force polygon on an active wedge for M-O method are depicted for case of a retaining wall. Effect of pseudo-static motion is represented by 'k_h.W' and 'k_v.W' as shown in Figure 5.1 (a) and by pseudo-static accelerations 'a_h = k_h.g' and 'a_v = k_v.g', where 'W' is weight of active soil wedge, 'k_h' and 'k_v' are horizontal and vertical ground acceleration coefficients respectively. Similarly, 'a_h' and 'a_v' are horizontal and vertical ground acceleration respectively. Total active thrust (including static thrust) is then expressed in equation 5.2

$$P_{AE} = \frac{1}{2} \cdot K_{AE} \cdot \gamma \cdot H^2 (1 - k_v) \tag{5.2}$$

Where 'K_{AE}' is dynamic active earth pressure coefficient and is denoted as in equation 5.3.

$$K_{AE} = \frac{\cos^2(\phi - \theta - \psi)}{\cos\psi \cdot \cos^2\theta \cdot \cos(\delta + \theta + \psi)\left[1 + \sqrt{\frac{\sin(\delta+\phi)\sin(\phi-\beta-\psi)}{\cos(\delta+\theta+\psi)\cos(\beta-\theta)}}\right]^2} \tag{5.3}$$

Where $\phi - \beta \geqslant \psi$, $\gamma = \gamma_d$ and ψ = arctan[k_h/(1-k_v)]. Other parameters of equation 5.3 are depicted in Figure 5.1.'α_{AE}' is inclination of static critical failure surface and according to Zarrabi-

Kashani, K. (1979) is according to equation 5.4.

$$\alpha_{AE} = \phi - \psi + \arctan\left[\frac{-\tan(\phi-\psi-\beta)+C_{1E}}{C_{2E}}\right] \tag{5.4}$$

Where 'C_{1E}' and 'C_{2E}' are as shown in equations 5.5 and 5.6 respectively.

$$C_{1E} = \sqrt{\tan(\phi-\psi-\beta)[\tan(\phi-\psi-\beta)+\cot(\phi-\psi-\theta)][1+\tan(\delta+\psi+\theta)+\cot(\phi-\psi-\theta)]} \tag{5.5}$$

$$C_{2E} = 1+\tan(\delta+\psi+\theta)\cdot[\tan(\phi-\psi-\beta)+\cot(\phi-\psi-\theta)] \tag{5.6}$$

As shown in equation 5.1, total active dynamic thrust is a sum of its static and dynamic component. Static component (P_A) acts at 'H/3' above the base and dynamic component (ΔP_{AE}) acts at approximately '0.6H' above the base according to Seed and Whitman (1970). Height of point of action of total thrust (P_{AE}) above the base according to these considerations is given by equation 5.7, where 'h' is height of acting 'P_{AE}' above the base.

$$h = \frac{P_A H/3 + \Delta P_{AE}(0.6H)}{P_{AE}} \tag{5.7}$$

It is often observed that value of 'h' is approximately near '0.5 H' for cases of retaining walls (Kramer (1996)).

5.1.2 Eurocode 8

Parameters used in M-O method are estimated using Eurocode 8 (NS-EN 1998-5:2004+NA:2014 (1998)). 'Part 1' of Eurocode 8 provides general aspects and rules for a seismic design of a structure and 'Part 5' is based on geotechnical aspects of foundation and retaining structure design. Horizontal and vertical ground acceleration coefficients ('k_h' and 'k_v') are estimated according to (EC 8-5, 7.3.2.2, p.(4)) as in equations 5.8 and 5.9.

$$k_h = \alpha \cdot \frac{S}{r} = \frac{a_g}{g}\cdot\frac{S}{r} \tag{5.8}$$

$$k_v = \pm 0.33 k_h \tag{5.9}$$

Where, 'a_g' is design ground acceleration, 'S' is amplification factor (depends upon soil conditions) and 'r' is a factor used for calculating 'k_h'. Design ground acceleration (a_g) is a product of a seismic factor (γ_I) and reference peak ground acceleration for 'Type A' ground (a_{gR}).

Tables and figures extracted from Eurocode 8 (NS-EN 1998-5:2004+NA:2014 (1998)) required for calculating parameters of 'M-O method' are tabulated in Appendix C.

5.2 Seismic Design of the Abutment

Method followed for the seismic design in this section is a modification of seismic analysis of geosynthetically reinforced retaining walls. As with static approach of reinforced soil retaining structural analysis, internal and external stability are analysed separately. Seismic analysis performed in this section also performs separate seismic analysis for external and internal stability, under pseudo-static conditions.

According to Kramer (1996), pseudostatic dynamic thrust (ΔP_{AE}) acts at the back layer of the reinforced zone and inertial force (P_{IR}) acts inside the reinforced zone (for the case of reinforced soil retaining wall), as shown in in Figure 5.2.

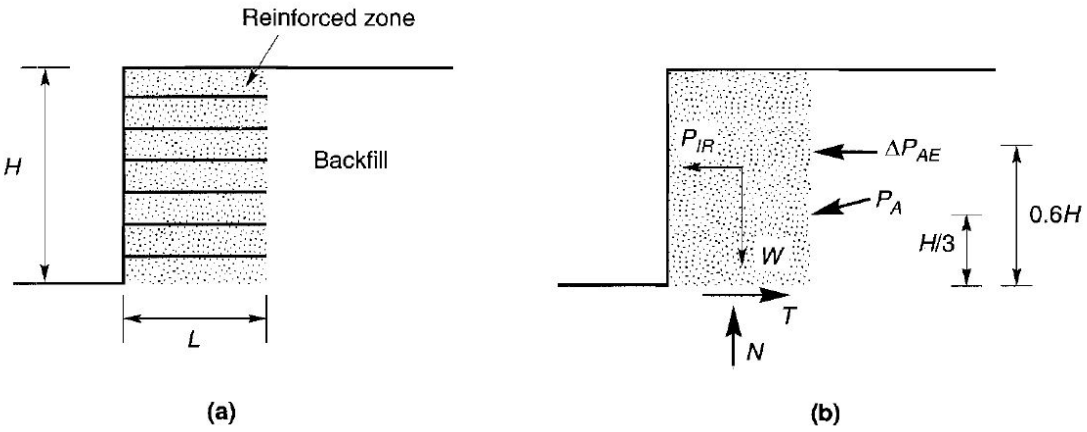

Figure 5.2: (a) Geometry and notation for reinforced soil walls, (b) Static and pseudostatic forces acting on reinforced zone (Kramer (1996))

Approach for reinforced soil wall explained in Figure 5.2 is modified in this case for representing an abutment. Dimensions of the abutment obtained from the limit state design in Figure 3.5 of Chapter 3 is used. The loading conditions are however, simplified for this case. Principle of superimposition of loads is assumed and all loads are converted to uniformly distributed loads (UDL). Assumptions made for the loading conditions are as follows:

- Live loads are ignored and dead loads are assumed to be distributed uniformly along the base of spread footing (loads from Table 3.11).
- The spread footing is assumed to extend throughout the entire reinforced region.
- The simplified loading is represented in Figure 5.3. Effective stress approach is used and pore pressures continue to remain ineffective.

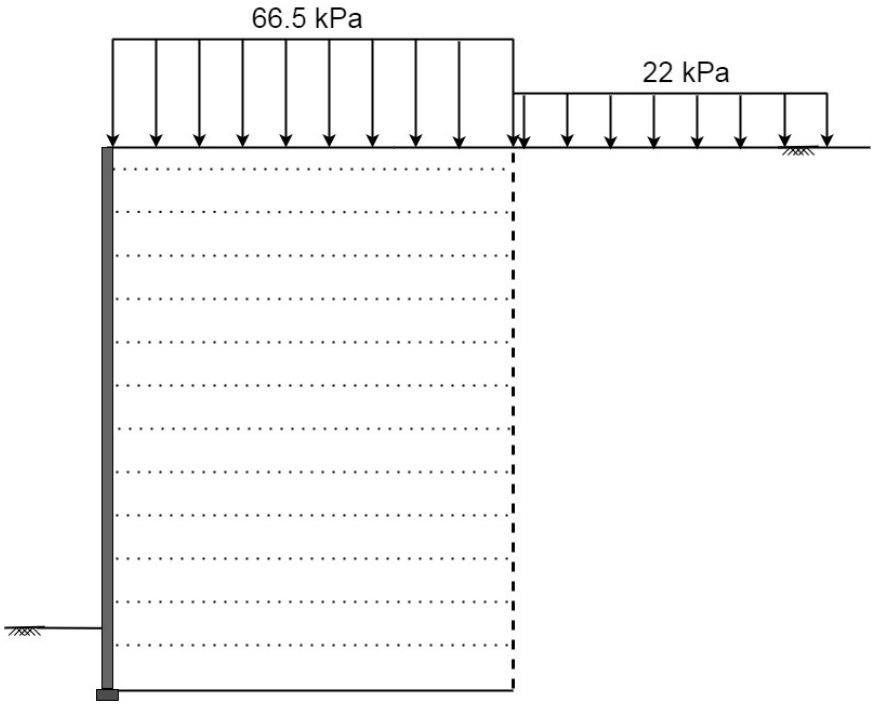

Figure 5.3: Simplified loading conditions for seismic analysis from Figure 3.5 (not to scale)

Interial force (P_{IR}) is calculated as in equation 5.10.

$$P_{IR} = \frac{a_c \gamma_r HL}{g} \tag{5.10}$$

Where, 'γ_r' is unit weight of reinforced soil and 'a_c' is calculated as in equation 5.11. 'a_{max}' in equation 5.11 is peak horizontal ground acceleration and 'g' represents acceleration due to gravity.

$$a_c = \left(1.45 - \frac{a_{max}}{g}\right) a_{max} \tag{5.11}$$

Eurocode 8 (NS-EN 1998-5:2004+NA:2014 (1998)) is used for estimating the seismic parameters of the above mentioned equations.

5.2.1 External Seismic Stability

Reference peak ground acceleration (a_{gR}) for Skedsmo, Trondheim (which is the assumed location for the abutment) is calculated by interpolating from the seismic zonal maps as 'a_{gR} = 0.44 m/s^2'. Design ground acceleration 'a_g' is then estimated as '$a_g = a_{gR} \cdot \gamma_I$ = 0.44 m/s^2', as 'γ_I = 1' for seismic class II from Table C.5. Amplification factor 'S' is estimated as 'S = 1.4' for 'Type C' ground and factor 'r' is estimated as 'r = 1' for bridge abutments from Tables C.3 and C.1 respectively.

Horizontal and vertical ground accelerations are then calculated using equations 5.8 and 5.9 as 'k_h = 0.062' and 'k_v = 0.02'. For estimating convention of angles as in Figure C.2(a), '$\delta = 20^o$' from C.6, '$\phi = 30^o$' from Table 3.2 and '$\beta = \theta = 0$' since backfill is horizontal. These values are tabulated in Table 5.1.

Table 5.1: Parameters fpr calculation using 'M-O ' method from Eurocode 8 (NS-EN 1998-5:2004+NA:2014 (1998))

Parameters for calculation using 'M-O ' method									
a_{gR}	γ_I	a_g	S	r	k_h	k_v	ϕ	ψ	δ
0.44 m/s^2	1	0.44 m/s^2	1.4	1	0.06	0.02	30^o	3.62^o	20^o

Calculation of static active thrust 'P_A', dynamic active thrust 'ΔP_{AE}' and total seismic thrust 'P_{AE}' are shown in results Table 5.2.

Table 5.2: Calculated results for the 'M-O' method

Results table for 'M-O' calculation								
K_A	K_{AE}	γ_b	H	P_A	P_{AE}	ΔP_{AE}	h	M_o
0.3	0.336	16 kN/m^3	5 m	60 kN/m	66.4 kN/m	6.4 kN/m	1.8 m	119.52 kN-m/m

As shown in Table 5.2, 'h' denotes point of action of seismic thrust calculated using equation 5.7. 'P_{AE}' is calculated using equations 5.2 and 5.3. 'M_o' is total seismic moment acting at the bottom of the abutment.

Inertial forces acting at the back of the reinforced zone are also considered for the external stability. Inertial force 'P_{IR}' for this case can be calculated as in equation 5.10 and 5.11.

Maximum value of 'ΔP_{AE}' and 'P_{IR}' is unlikely to occur at the same time and hence total force for checking safety against sliding and overturning is '$F_{dyn} = P_{AE} + 0.5\ P_{IR}$'. Results for these values are shown in Table 5.3.

Table 5.3: Results for total force in seismic condition for external stability

Results for total force in seismic condition 'F$_{dyn}$'							
a$_{max}$	a$_c$	γ_r	H	L	P$_{IR}$	F$_{dyn}$	M$_o$
0.44 m/s^2	0.62 m/s^2	17 kN/m^3	5 m	3.6 m	19.34 kN/m	76.07 kN/m	136.93 kN-m/m

Seismic action of lower magnitude is used for the calculation, and the loading is simplified. Dynamic forces compared to limit equilibrium external stability for sliding and overturning (Tables 3.10 and 3.11), shows that this particular seismic action has a large factor of safety. Specific statement of this specific design is that resisting sliding forces and moments should be at least 75 percent of obtained 'F$_{dyn}$' taking a factor of safety of 0.75 as mentioned in Kramer (1996).

5.2.2 Internal Seismic Stability

Tensile and pullout behaviour of reinforcements are vital in evaluating internal stability of a reinforced soil bridge abutment. Failure surface assumed for the internal failure in this seismic analysis is same as mentioned in limit equilibrium internal design (FIgure 3.3). Static tensile forces calculated are also extracted from Chapter 3, Tables 3.13 and 3.14. Pseudo-static inertial force 'P$_{IR}$' acting on the unstable wedge is considered for the internal instability of the abutment. 'P$_{IR}$' for this case is calculated from equation 5.12 (Kramer (1996)).

$$P_{IR} = \frac{a_c W_A}{g} \tag{5.12}$$

Where 'W$_A$' is the weight of the assumed internal failure wedge. Weight of the assumed failure wedge is calculated as per Figure 3.3, according to which 'P$_{IR}$ = 10.35 kN/m'.

Calculation results are shown in Table 5.4. The dynamic inertial force is distributed to each reinforced layer according to their resistant area (area of reinforcement extending beyond the failure plane) and added with static tensile force obtained from Tables 3.13 and 3.14. In Table 5.4, 'P$_{area}$' is the percentage area of reinforcement that is beyond critical failure line. 'T$_{seismic}$' is sum of static tensile force 'T$_n$' and dynamic component of tensile force 'P$_{IR(dyn)}$'.

According to this design, a higher value of tensile force is observed. In contrary, factor of safety for seismic design is '0.75' in compared to '1.5' used in static condition (Kramer (1996)). Due to this, it is not necessary to increase the length of reinforcement for this design. It is per-

Table 5.4: Results for total force in seismic condition for external stability

Layer (n)	$\mathbf{P_{area}}$ (%)	$\mathbf{T}_n$ (kN/m)	$\mathbf{P_{IR(dyn)}}$ (kN/m)	$\mathbf{T_{seismic}}$ (kN/m)
1	3.85	26.31	0.40	26.71
2	7.7	52.46	0.80	53.26
3	15.4	52.21	1.59	53.80
4	23.1	51.90	2.39	54.28
5	30.8	51.52	3.19	54.71
6	38.5	51.09	3.98	55.07
7	46.2	50.60	4.78	55.38
8	53.9	50.05	5.57	55.63
9	61.6	49.44	6.37	55.82
10	69.3	48.78	7.17	55.94
11	77	48.05	7.96	56.02
12	84.7	47.27	8.76	56.03
13	92.4	46.43	9.56	55.98

tinent to observe the distribution of tensile force from layer 2 to layer 13 for seismic and static conditions, as shown in Figure 5.4.

As shown in Figure 5.4, 'layer 1' is ignored in the chart as it is located at half the vertical reinforcement spacing. For layers 2 to 13, distribution of tensile forces show higher values according to depth for seismic condition, but approximately same when it comes to the surface.

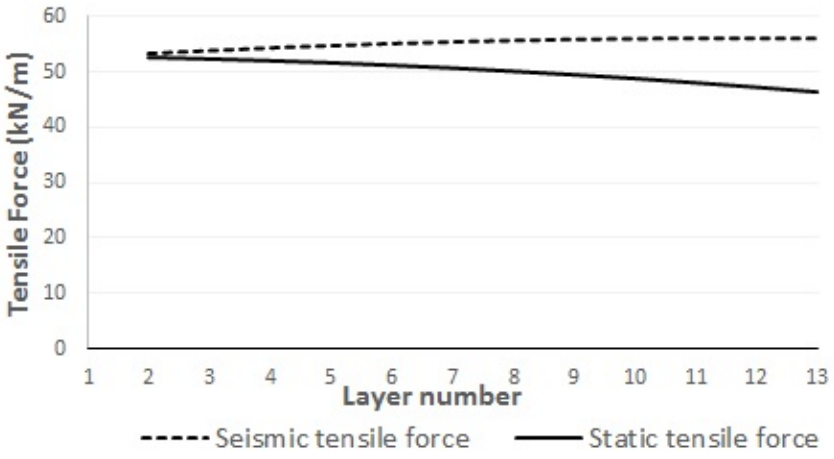

Figure 5.4: Tensile forces in reinforced layers for static and seismic conditions

Acceleration is assumed to be acting at the centroid of the abutment. Higher tensile stress at depth can be contributed to distribution of inertial forces according to depth, and failure mechanism assumed for the calculations in Table 5.4.

Chapter 6

Seismic Modeling and Dynamic Analysis in PLAXIS 2D

Modeling seismic behaviour of a soil structure can be surmised as defining numerical parameters for motion of seismic waves originated at the source of an earthquake, and its propagation to the location of the concerned soil structure. Equation of motion, earthquake excitation, shear wave velocity, shear modulus and wave dampening are hence essential parameters for understanding and defining the modal behaviour. Introductory portion of this Chapter gives a brief mention of the relevant parameters and their interaction with soil, before using those parameters in dynamic analysis of PLAXIS 2D. Equations involved in the introductory part are essential components of the analysis, and are crucial for illustrating wave behaviour and seismic phenomenon discussed in this chapter. The Chapter then proceeds to selection and use of boundary conditions and finally analyzes the simplified version of previously designed abutment model, with selected parameters.

6.1 Shear Waves and their Interaction with Soil

Differential equation describing lateral displacement of a structure with single degree of freedom and no external force or damping is shown in equation 6.1, where overdot denotes differentiation with respect to time, where 'u' is displacement in time. Which means, $\dot{u}$ represents velocity and $\ddot{u}$ denotes acceleration with time. 'm' and 'k' represent the mass and stiffness of the

system respectively.

$$m\ddot{u} + ku = 0 \tag{6.1}$$

Damping of a wave is described as a process by which amplitude of a vibration steadily diminishes (Chopra (2012), p.7). The transformed differential equation of motion, with introduction of damper is shown in equation 6.2, where 'c' is damping coefficient and 'u' is velocity (Magar (2016)). For dynamic analyses, damping can be represented by 'Rayleigh damping parameters' comprising of a damping matrix 'C', constituting mass matrix 'M' and stiffness matrix 'K' (PLAXIS (2019b)); represented in equation 6.3.

$$m\ddot{u} + ku + cu = P \tag{6.2}$$

$$C = \alpha M + \beta K \tag{6.3}$$

In equation 6.3, 'α' and 'β' are rayleigh coefficients representing influence of mass and stiffness in damping of a system. Relaion between α, β and damping ratio 'ζ' is shown in equation 6.4 as per PLAXIS (2019b).

$$\alpha + \beta\omega^2 = 2\omega\zeta \tag{6.4}$$

In equation 6.4, '$\omega = 2\,\pi f$', where 'ω' is circular frequency and 'f' is 'eigen-frequency'. Also as mentioned in Magar (2016) and described in PLAXIS (2019b), the damping coefficients can be found by solving for different target frequencies and corresponding target damping ratios. Eigen-frequency 'f' with respect to shear wave velocity 'v_s' and thickness of soil 'H' is given in equation 6.5.

$$f = \frac{v_s}{4H} \tag{6.5}$$

Amplification is associated with wave energy and for a seismic wave, large amplitude can be seen for seismic waves in soft soil. An amplitude factor is used to compare amplitude at top and bottom of a layer. For a linearly elastic model, amplification factor can be calculated as shown in equation 6.6

$$A = \frac{1}{\sqrt{\cos^2(\frac{\omega H}{v_s}) + (\zeta(\frac{\omega H}{v_s}))^2}} \tag{6.6}$$

Seismic body waves exist mainly in two forms, primary waves 'p-waves' and shear waves 's-waves'. Surface waves result as interaction of these body waves with surface layers of earth (Kramer (1996), p.20). The velocity of primary waves 'v_p' and shear wave velocity 'v_s' on an unbound media depend upon stiffness of material and Poisson's ratio 'ν' as shown in equation 6.7.

$$\frac{v_p}{v_s} = \sqrt{\frac{2-2\nu}{1-2\nu}} \tag{6.7}$$

In general, 'p-wave' velocity is seen to exceed the shear wave velocity for geologic materials. For a Poisson's ratio of 0.3, ratio of 'v_p/v_s' is found to be 1.87 as per (Kramer (1996), p.156).

In real materials, a part of elastic wave energy is always converted to heat energy, resulting in depletion of amplitude of the wave. When assuming the propagation of wave as visco-elastic, Kelvin-Voight model is used as soil strip. Stress-strain loop of a Kelvin-Voight model is found to be elliptical. The energy dissipated in a cycle for this case is given by the area of ellipse or by equation 6.8, indicating the relationship between loading frequency and energy dissipation.

$$\Delta W = \int_{t_o}^{t_o+2\pi/\omega} \tau \frac{\delta\gamma}{\delta t} dt = \pi\eta\omega\gamma_o^2 \tag{6.8}$$

Where, 'τ', 'γ' and 'η' are shear stress, shear strain and viscosity of the material respectively. In case of real soil however, dissipation of elastic energy occurs by slippage of soil grains hysteretically, and energy dissipation is independent of wave frequency. Peak energy and energy dissipated in a cycle for a hysteresis loop is shown in Figure 6.1.

Damping ratio 'ζ' is related to energy dissipated and peak energy as in equation 5.5.

$$\zeta = \frac{1}{4\pi}\frac{\Delta W}{W} \tag{6.9}$$

The dynamic behavior of soil during earthquake is often related to its response to cyclic loading. Soil properties under cyclic loading is dependent upon state of stress in soil before loading, and stress created by the the loading (Kramer (1996), p.184). The hysteresis loop shown in Figure 6.1 depicts the behaviour of soil under cyclic loading, and can be described by the path

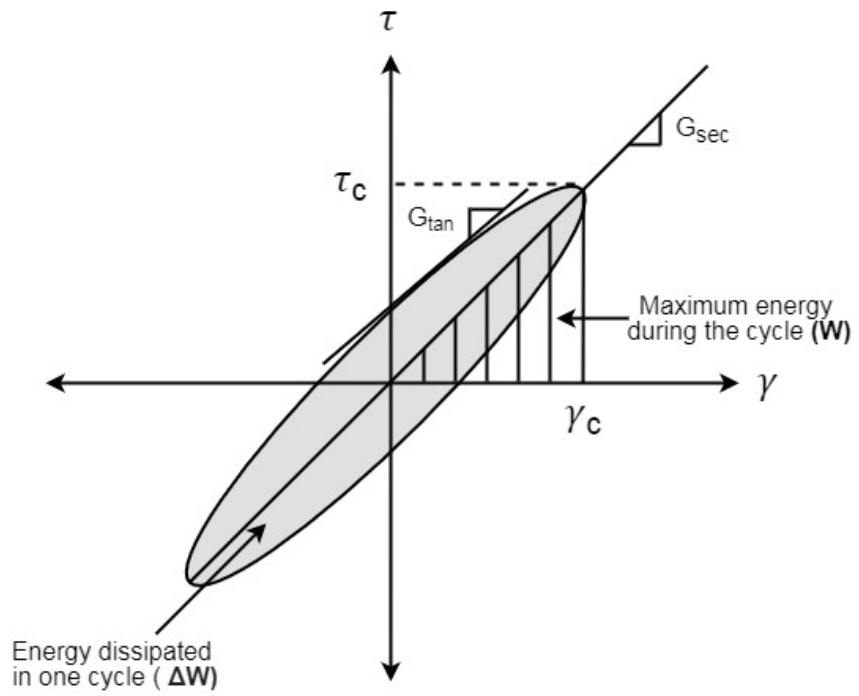

Figure 6.1: Hysteresis loop for shear stress - strain behaviour of soil (after Kramer (1996))

followed by the loop or by parameters defining it as a shape. Mean value of shear modulus over the whole loop can be estimated by secant modulus 'G$_{sec}$' as shown in Figure 6.1 and described in equation 6.10.

$$G_{sec} = \frac{\tau_c}{\gamma_c} \tag{6.10}$$

Where, 'τ_c' and 'γ_c' are amplitudes of shear stress and shear strain respectively. Like in the case of Kelvin-Voight model, area of the hysteresis loop estimates the energy dissipation. Damping ratio for this case is given in equation 6.11.

$$\zeta = \frac{W_D}{4\pi W_S} = \frac{1}{2\pi}\frac{A_{loop}}{G_{sec}\gamma_c^2} \tag{6.11}$$

Where, 'W$_D$' and 'W$_S$' are dissipated energy and peak strain energy respectively, with 'A$_{loop}$' giving area of the hysteresis loop. The locus followed by the tip of the hysteresis loop for different cyclic strain amplitude is called a 'backbone curve' and is shown in Figure 6.2.

In Figure 6.2, slope of the curve at the origin gives maximum value of shear modulus as 'G_{max}'. A modulus ratio described as 'G$_{sec}$/G$_{max}$' is a useful parameter in characterizing stiff-

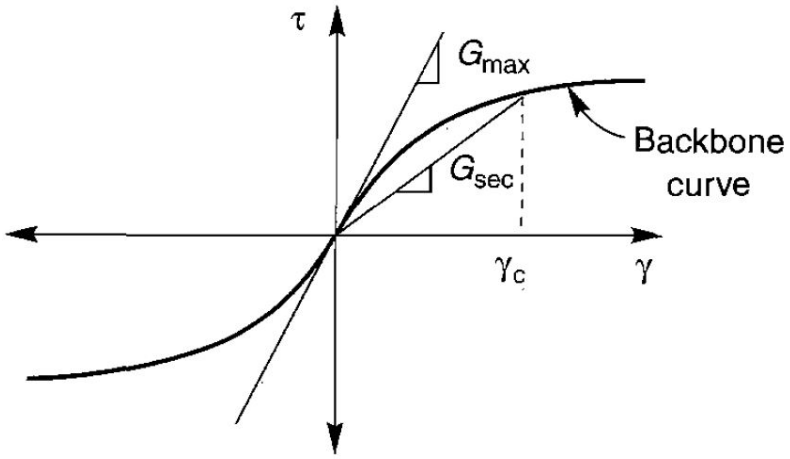

Figure 6.2: Variation of 'G$_{sec}$' with 'γ' in a backbone curve (Kramer (1996), p.232)

ness of a soil element. For shear strains less than '3 X 10^{-4} %', 'G$_{max}$' can be calculated in form of shear wave velocity 'v$_s$' as mentioned in equation 6.12.

$$G_{max} = \rho v_s^2 \tag{6.12}$$

In situations where shear wave velocities are not available, 'G$_{max}$' can be calculated in many different ways including using laboratory data and emperical relationships. Since sand is used as the material used for design of the considered abutment, 'G$_{max}$' for sand is often calculated by an emperical relationship as shown in equation 6.13.

$$G_{max} = 1000 K_{2,max} (\sigma'_m)^{0.5} \tag{6.13}$$

Where '$K_{2,max}$' is calculated from relative density or void ratio in Table 6.1. 'σ'_m' is mean stress in lb/ft^2 (Seed and Idriss (1970)).

Table 6.1: Estimaion of K$_{2,max}$ (Seed and Whitman (1970))

e	**K$_{2,max}$**	**D$_r$**	**K$_{2,max}$**
0.4	70	30	34
0.5	60	40	40
0.6	51	45	43
0.7	44	60	52
0.8	39	75	59
0.9	34	90	70

Various environmental and load conditions play active role in increase or decrease of modulus ratio at a particular strain level (Dobry and Vucetic (1987)).

6.2 Hardening Soil Small (in Dynamic Application)

Hardening soil small is chosen as soil material model for the dynamic analysis, like in the case of static analysis. This is because the model incorporates strain dependent modulus of stiffness resulting from vibrations (PLAXIS (2019b)). The model is also used for the dynamic analysis of the abutment because of its capability of modeling hysteretic damping during cyclic loading and dynamic applications. The formulation of small-strain is a result of degradation of shear stiffness with shear strain. This property in combination with hysteretic behaviour in cyclic loading, is capable of providing damping in dynamic applications (Brinkgreve et al. (2007)). The additional information needed for small-strain stiffness is retrieved from modulus reduction curves. Hysteretic behaviour of Hardening Soil small model under cyclic loading is shown in Figure 6.3.

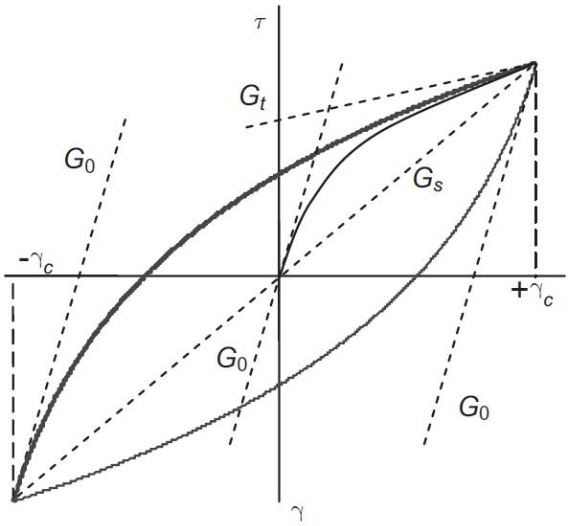

Figure 6.3: Hysteretic behaviour of HSsmall model (Brinkgreve et al. (2007))

In Figure 6.3, 'G$_o$' is small-strain shear stiffness, 'G$_s$' is secant shear modulus and 'G$_t$' is tangent shear modulus. It can be seen in the figure that the actual shear stiffness decreases with increasing shear strain of the model and restarts upon load reversal. The additional parameters used for the 'HS small' model (i.e. $\gamma_{0.7}$ and G_o^{ref}) play significant role in changing damping.

A lower '$\gamma_{0.7}$' is seen to give more more damping and and variation of 'G_o/G_{ur}'gives different maximum damping ratio (independent of $\gamma_{0.7}$)(Benz, T. (2006)). The equation for calculating hysteretic damping ratio (ζ) as per Brinkgreve et al. (2007) is shown in equation 6.14.

$$\zeta = \frac{E_D}{4\pi E_s} \tag{6.14}$$

Where, 'E_D' is dissipated energy in a load cycle and 'E_s' is energy stored at maximum strain respectively.

6.3 Selection of Boundary Condition

Interaction of seismic waves with its boundaries are one of the most important factors determining the behaviour of a numerical seismic model and also has its complexity in modeling. Seismic waves from the source of an earthquake inevitably meets discontinuities and incongruities while travelling towards earth surface. The seismic waves tend to reflect, refract and form new paths due to these discontinuities and variabilities. It is therefore crucial to analyze and understand the behaviour of boundary condition of a model, before applying it.

Relevant assembly of boundary conditions will be discussed and applied to a simplified model of the abutment in consequent sub-sections. The simplified model of abutment for studying boundary condition is an elongated version of original static model, with abutment represented by a section of reinforced soil. Soil parameters are represented with a linearly elastic model. The simplified model is shown in Figure 6.4.

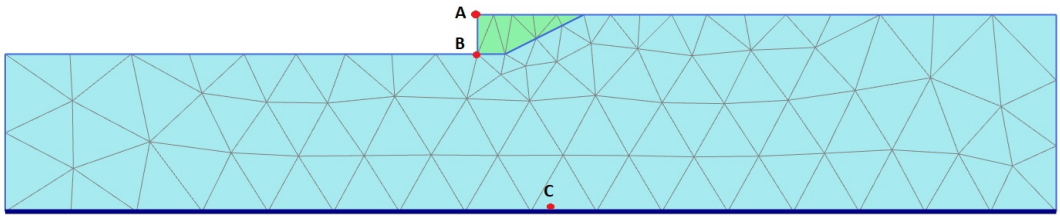

Figure 6.4: Simplified model of abutment for boundary analysis (in PLAXIS 2D)

The simplified model shown in Figure 6.4 is for a medium coarse mesh, and is 130 m wide and 25 m high. It constitutes of two types of linearly elastic material, which are reinforced soil

representing the abutment and backfill soil representing the surrounding. Three points are selected at the top and toe of the model represented by 'A' and 'B' and at the mid bottom of the model represented by 'C' respectively. Parameters used for them are listed in Table 6.2.

Table 6.2: Material parameters for the boundary analysis of simplified model

Parameters	**Reinforced Soil**	**Backfill Soil**
Material model	Linear elastic (drained)	Linear elastic (drained)
Unit Weight (γ)	17 kN/m^3	16 kN/m^3
Rayleigh coefficients (ζ)	α = 0.2856 and β = 0.0029	α = 0.2856 and β = 0.0029
Modulus of elasticity (E)	46.10 MPa	43.38 MPa
Poisson's ratio (ν)	0.33	0.33
Shear wave velocity (v_s)	100 m/s	100 m/s

A condition of resonance is reached when input vibration is of same frequency as eigen-frequency of the system and this results in maximum amplitude (Magar (2016)). Amplitude factor for a linearly elastic model can be calculated analytically from equation 6.6. From parameters of Table 6.2 and equation 6.5, eigen frequency of the model can be calculated as ' $f_1 = \frac{v_s}{4H}$ = 1 Hz'. The tests for boundary conditions are hence carried out using 1 Hz for meeting resonance condition and 0.5 Hz for making comparisons.

A sinusoidal acceleration wave of '0.05g' amplitude and varying frequency (0.5 Hz and 1 Hz) is prescribed at the base. The vibration is applied for 25 seconds with a prescribed displacement of 0.5 meters in horizontal direction and vertical displacement is restrained. A point load of 10 kN/m is applied at the top of the abutment in the direction of prescribed displacement (right).

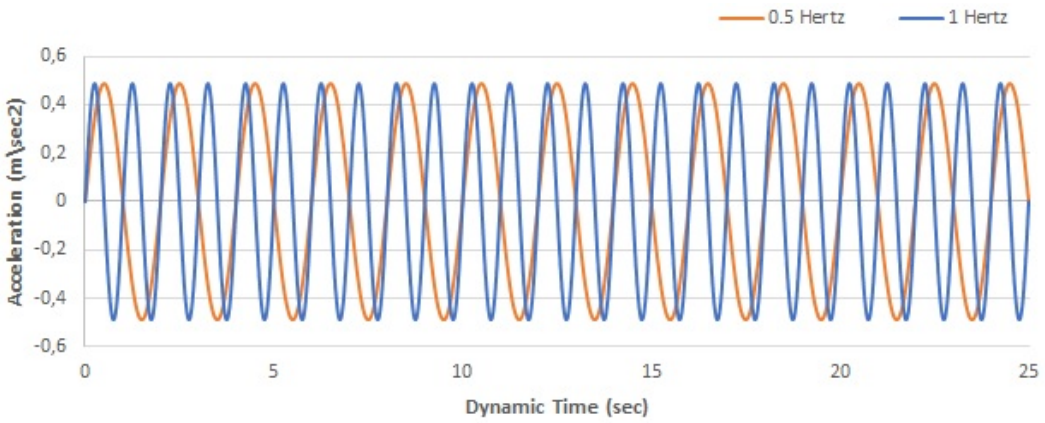

Figure 6.5: Used 0.5 Hz and 1 Hz frequented harmonic waves of amplitude 0.05g and duration 25 seconds

0.5 Hz and 1 Hz wave-forms used in the model are shown in Figure 6.5. The lateral boundaries at the sides are applied for different combination of boundary conditions for analyzing the

resulting behaviour of the model . The water table is placed at the bottom of the boundary for the simplified model, but undrained behaviour is ignored - similar to all design and analysis involved in preceding Chapters.

For all three boundary analysis tests, the calculation stages in PLAXIS 2D were carried out in three stages. An equilibrium stage in plastic calculation mode is added between initial stage and dynamic stage to ensure that only dynamic acceleration is added during dynamic stage. The base of the model is fixed in vertical direction and a fixed base is a completely reflective boundary. A compliant base boundary can also be an option for studying boundary behaviour of the base. But this section focuses on behaviour of lateral boundaries and the base is fixed vertically for all considered lateral boundary combinations illustrated in subsequent analyses.

6.3.1 Viscous Lateral Boundaries

Viscous boundary was introduced by Lysmer and Kuhlemeyer (1969). The boundary conditions represent viscous dampers applied in X and Y direction along the concerned boundary. It absorbs the the wave energy of outgoing waves proportional to material near the boundary (PLAXIS (2019b), p. 343). The boundary is usually considered for vibration source inside the model. Relaxation coefficients 'C_1' and 'C_2' are set to default for this case.

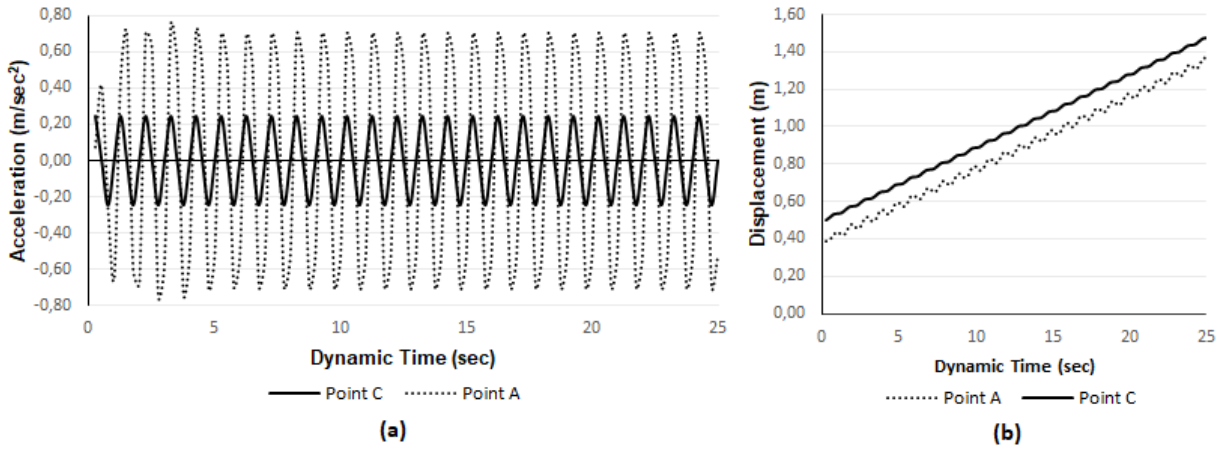

Figure 6.6: (a) Horizontal acceleration of points 'A' and 'C' at 1 Hertz with viscous lateral boundaries (b) Total displacement of points 'A' and 'C' at 1 Hertz with viscous lateral boundaries

Use of interfaces is not mandatory for viscous boundaries and is not applied for this case. Acceleration and dynamic time graph shown in Figure 6.6 (a), shows that applied acceleration of 0.05g (i.e. 0.49 m/s^2) is amplified to an approximate average of 0.75 m/s^2 for top point 'A'

but is reduced to 0.2 m/s^2 for point 'C'. This is attributed to resonance condition caused by equivalent input vibration relative to eigen frequency and a vertically fixed base. Displacement graph shown in Figure 6.6 (b) shows how the prescribed displacement of 0.5 meters escalates to approximately 1.5 meters at the end of 25 seconds of applied vibration.

Horizontal acceleration at point 'C' for 0.5 and 1 Hz as shown in Figure C.3 (a) of Appendix C, shows that there is no difference in amplitude for the differed frequencies but change in path from the initial path can be seen along with the diminished amplitude due to fixed vertical movement. Figure C.3 (b) shows the dominance of resonant frequency.

6.3.2 Free Field Lateral Boundaries

Free field boundaries simulate the propagation of waves far beyond the boundary and is only available for lateral boundaries. Equivalent shear forces and normal forces are applied to simulate transfer of free field motion to the main domain as shown in Figure 6.7.

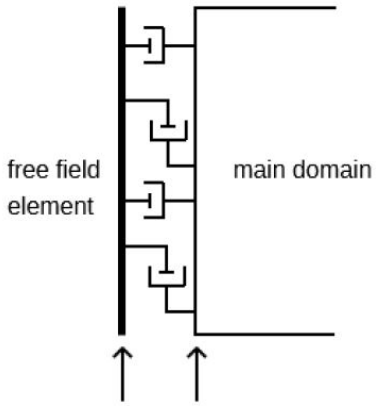

Figure 6.7: Free field lateral boundary (PLAXIS (2019b), p. 144)

Interface inside the mesh is compulsory for using this lateral boundary condition and the simplified model used is modeled in similar way. It can be seen in the horizontal acceleration graph of Figure 6.8 (a), that acceleration at point 'A' reaches almost 2 m/s^2, while acceleration at point 'C' remains at about 0.2 m/s^2. Use of interface element at the bottom has not significantly changed the horizontal acceleration, but the free field condition has further amplified the resonant acceleration of point 'A'. The effect seen in Figure 6.8 (a), can be compared closely to what happens to similar soil structure in actual earthquake. In compared to the viscous boundary, the open field boundaries are showing more than twice increase in amplitude of acceleration. 1 Hz

horizontal acceleration wave also shows slight fluctuation in the first half of vibration, contrary to uniform horizontal acceleration waves of viscous boundaries.

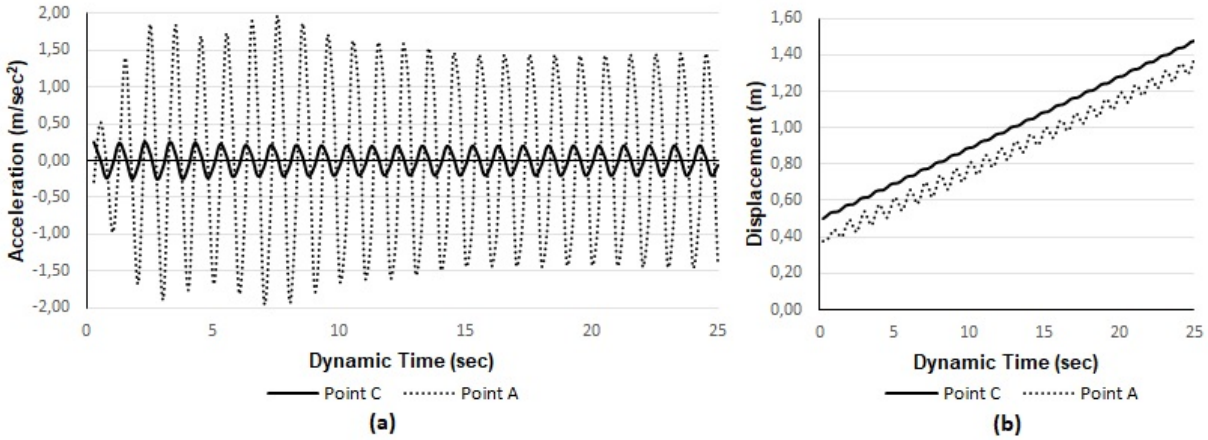

Figure 6.8: (a) Horizontal acceleration of points 'A' and 'C' at 1 Hertz with free field lateral boundaries (b) Total displacement of points 'A' and 'C' at 1 Hertz with free field lateral boundaries

It is observed in Figure C.4 (a) of Appendix C, that a difference in amplitude between 0.5 and 1 Hz horizontal acceleration at point 'C' is observed. A certain shift in phase can also be seen in the resultant waves for point 'C'. Variation of displacement is observed to be same as with viscous boundaries at point 'C', since the base is still fixed in vertical direction like in the case of viscous boundaries - as depicted in Figure C.4 (b).

6.3.3 Laterally Loaded - Open Boundaries

Prior to conducting test for laterally loaded - open boundaries, laterally loaded - free field boundaries were tested in the simplified model. The horizontal acceleration graphs obtained for laterally loaded - free field boundaries were exact match with the free field boundaries test conducted above. It indicated that free field boundaries were not accepting the lateral loads that were being added. It is therefore excluded from the analysis, but the acceleration and displacement graphs for laterally loaded - free field boundaries can be found at Figure C.6.

The third boundary assembly considered for the test is laterally loaded - open boundaries. Open boundaries do not have any additional property of reflection or absorption, and it simply terminates. Laterally loaded - open boundaries are combination of lateral loads at both boundaries with a specific 'K_o' value in combination with no boundary condition. 'K_o' value used for this case is '$K_o = 1$'. Advantage of using such lateral coefficient is that it performs accurate depic-

tion of an earthquake situation with source far from the boundaries. The lateral loads are crucial while considering soil stresses involved at depths, and are often used for dynamic modeling of soil. Interfaces with strength of 0.8 is used at the lateral boundaries and the fixed base, similar to prior tests.

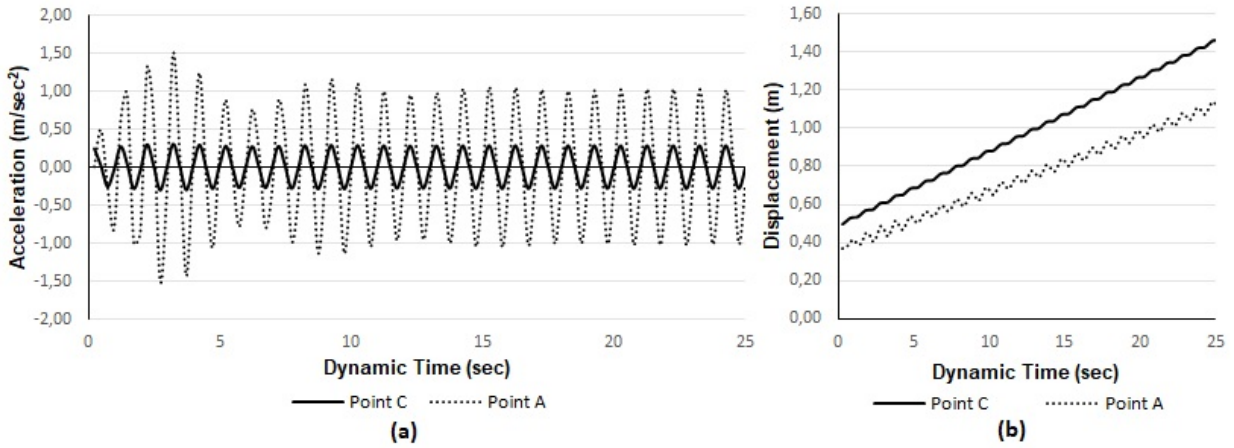

Figure 6.9: (a) Horizontal acceleration of points 'A' and 'C' at 1 Hertz with laterally loaded - open boundaries (b) Total displacement of points 'A' and 'C' at 1 Hertz with laterally loaded - open field boundaries

As shown in Figure 6.9 (a), horizontal acceleration for the point 'C' at the fixed base shows no change since it is fixed vertically in this case too. Horizontal acceleration of point 'A' however shows an amplitude of 1 Hz but with fluctuations reaching up to 1.5 Hz in the first five seconds. In compared to the viscous boundaries and free field boundaries, amplitude of the laterally loaded - open field boundaries lie between those two. The results are however closer to the free field boundaries. As observed in Figure 6.9 (b), displacement and time graph shows difference relative to the previous two tests. Displacement of point 'A' and 'C' with time shows that displacement increment with time is not uniform in this case. This can be attributed to difference in ground level at the left and right lateral boundaries. It can also substantiate a need of specific boundary condition for soil structures with lateral boundaries involving different elevations.

It is observed in Figure C.5 (a) that 0.5 Hz waves show lower amplitude than 1 Hz waves at point 'C'. It is opposite to what was observed for free field boundaries where 0.5 Hz acceleration waves were dominant in point 'C'. The difference however is not very prominent and can be attributed to the change in boundary situation. Similar phase shift of the acceleration waves is observed, as with prior tests.

6.3.4 Comparison of the Boundaries and Displacements

Comparing all the three performed tests of boundary conditions, it is observed that maximum peak horizontal acceleration is produced with free field boundary conditions. Minimum peak horizontal acceleration is observed with use of viscous boundaries and open boundaries with lateral loads lie in between them. Since eigen frequency was used as the frequency of input vibration, it can be derived from the tests that the free field boundaries were better at simulating real earthquake behaviour by giving maximum amplitude. It is also observed that laterally loaded - open boundaries are a good option for soil structures at same elevation, but creates variance in calculation when there is difference in elevation between the lateral boundaries.

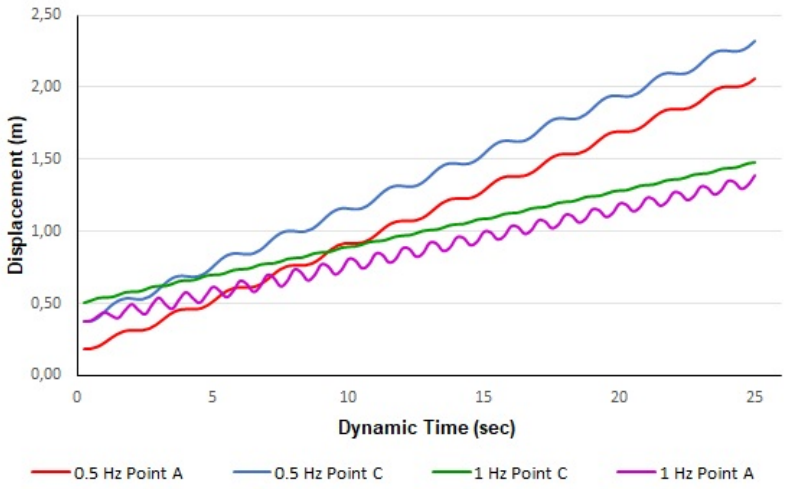

Figure 6.10: Total displacements at points 'A' and 'C' with 0.5 and 1 Hertz

In Figure 6.10, variance in displacement with dynamic time for 0.5 and 1 Hz waves are shown at top and bottom of the model. Higher frequency shows lower total displacement and this is attributed to the nature of ground motion. Acceleration can be interpreted as product of displacement and angular frequency and this makes displacement inversely proportional to angular frequency, for ground motion. From another perspective, the gradation of soil and eigen-frequency also affects displacement for varying frequencies of same amplitudes.

From the tests conducted, free field lateral boundaries seem to be an appropriate lateral boundary considering elevation changes and accurate simulation of earthquake source far from the boundary. Free field lateral boundaries also show good correspondence with resonance condition of input frequency and eigen-frequency in this case.

6.4 Dynamic Analysis of the Abutment model

For this portion, an actual earthquake data is acquired and scaled to prescribed intensities, and applied to the model of abutment with HS small soil model. It is discussed that HS small model has capabilities to simulate shear modulus reduction behaviour along with shear strain increment. This behaviour is crucial for working mechanism of the discussed abutment and is the main object of study in this section.

Earthquake selected for this section is known as 'Konya earthquake' and it occurred near Konya dam of Maharashtra, India in 1967. The earthquake is argued to be induced due to filling of a dam reservoir in that area and is a peculiar example of Reservoir Induced Seismicity (RIS) (Gupta and Rambabu (1993)). The cause of seismicity however is not discussed in this report and the data is used only for studying the behaviour of the abutment model. The acceleration time history acquired for this section is acquired from the national database and has a PGA of 0.3g. It is scaled before being used in PLAXIS 2D and the time step is 0.02 seconds for 20 seconds total time. Which means that '20/0,02 = 1000' time steps would be needed in PLAXIS 2D for the dynamic calculation part.

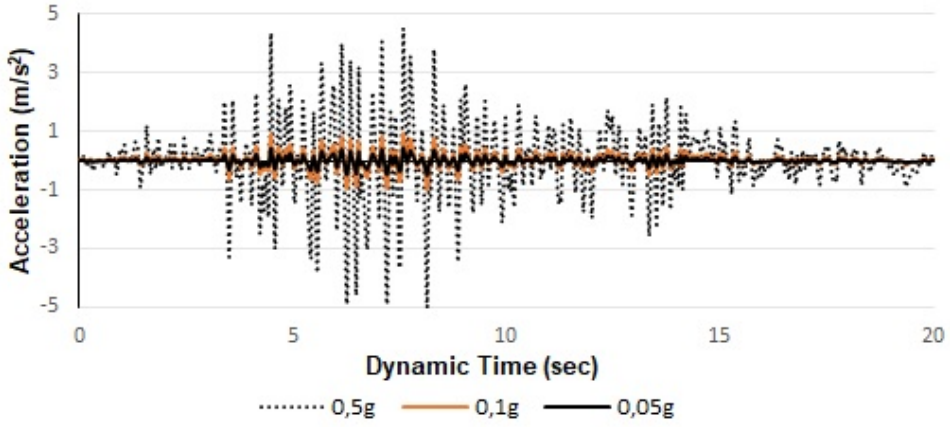

Figure 6.11: Used acceleration time history of 20 seconds scaled to 0.05g, 0.1g and 0.5g

(*Note: It is mentioned here that the acceleration time history is not normalized and is only scaled for the PGA. There are three calculation phases in all analyses involving this earthquake time history. An equilibrium phase is added between the initial and dynamic calculation phase. A prescribed displacement of 0.5 meters is applied in the X-direction for both equilibrium and dynamic phase in addition to the acceleration at the base. Due to this, the acceleration applied is*

scaled by a factor of 0.5 (i.e. effective PGA applied is 0.025g, 0.05g and 0.25g respectively). This is evident in displacement and time plot for the bottom point of the model as shown in Figure 6.16, (b)).

Figure 6.11 shows the scaled acceleration - time history scaled to above mentioned PGAs. Units used for acceleration is m/s^2 for using in PLAXIS 2D. The magnitude of used earthquake is 6.5 in Richter scale and showed a PGA of 0.3g in its in-scaled original accelerogram. Observation of the waveform shows that PGA is reached between 5 and 10 seconds.

Lateral boundary conditions are selected as free field boundaries. Free field boundaries are selected for this case because according to tests conducted in preceding section, free field boundaries simulate the resonance frequency more precisely. It is also chosen because tied degree of freedoms are inapplicable for lateral boundaries at different elevations (Magar (2016)) and laterally loaded open boundaries showed discrepancies in displacement estimation at different elevations previously.

Hardening Soil small model is chosen for the analysis and the model involves interaction between two types of HS small soil models. Parameters for the backfill and reinforced soil section are shown in Table 6.3.

Table 6.3: HS small soil parameters for dynamic model

Parameters	**Reinforced soil**	**Backfill soil**
Model	Hardening Soil small	Hardening Soil small
Drainage type	Drained	Drained
Rayleigh Coefficients (ζ)	$\alpha = 0.2856, \beta = 0.0029$	$\alpha = 0.2856, \beta = 0.0029$
γ	17 kN/m^3	16 kN/m^3
E_{50}^{ref}	12 Mpa	12 Mpa
E_{oed}^{ref}	16 Mpa	16 Mpa
E_{ur}^{ref}	60 Mpa	60 Mpa
c	5 kPa	5 kPa
v'_{ur}	0.2	0.2
ϕ	33^o	30^o
G_o^{ref}	168000 kPa	168000 kPa
$\gamma_{0.7}$	0.0001	0.0001
K_o^{nc}	0.4554	0.5
R_{inter}	0.8	0.8

As shown in Table 6.3, interfaces with relative strength of 0.8 is used along the inside of the lateral and bottom boundary. For model geometry, assumptions are made that no load is incurred upon the structure. A fixed boundary is used at the bottom of the model with a prescribed horizontal displacement. The calculation phases involves an equilibrium plastic phase between

the initial phase and dynamic calculation phase. A prescribed horizontal displacement of 0.5 meters is applied in the equilibrium phase for setting up the displacement multipliers. A dynamic acceleration time history of '0.05g' converted to 'm/s^2' is applied at the fixed base in the dynamic phase. Interactive behaviour of the two HS small soil models in dynamic situation is the specific objective of this case.

The analysis is divided into two sub sections for analysing interaction of HS soil model without geogrids and then with geogrids. The geometry of the model is however the same and the only difference is the 'added geogrids' in the second sub-section. Length and properties added are as per the limit state design performed in Chapter 3.

6.4.1 Dynamic Abutment Model without Geogrids

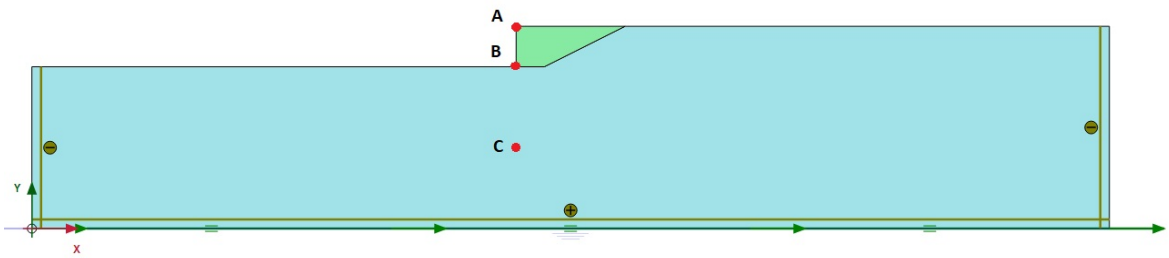

Figure 6.12: Curve points and model geometry for dynamic analysis without geogrids (in PLAXIS 2D)

Geometry of the model is shown in Figure 6.12. The geometry is 25 meters high up to the top of the abutment and 20 meters high to the abutment toe. Width of the abutment is 133.5 meters. The coordinates of origin is shown in the bottom left corner of Figure 6.12 and three points are selected for curves as A(60,25), B(60,20) and C(60,10). The groundwater level is shown at the bottom but undrained behaviour and suction is avoided in the calculation to adhere with calculations performed previously. Medium mesh is used for the calculations.

Two points of major interest for the performed analysis are Point 'A' and Point 'B' (abutment top and toe respectively). Point 'C' is chosen for comparison of abutment toe data. Since reinforcements are not added in this case, point 'A' is bound to suffer the maximum displacement. Observation for a particular PGA input is done in terms of horizontal acceleration against dynamic time and frequency spectrum representation, for the same amplitudes.

For an amplitude of 0.05g, horizontal acceleration variation between point A and B is shown in Figure 6.13. For 0.05g amplitude, dominant frequency of vibration at Point A is observed as

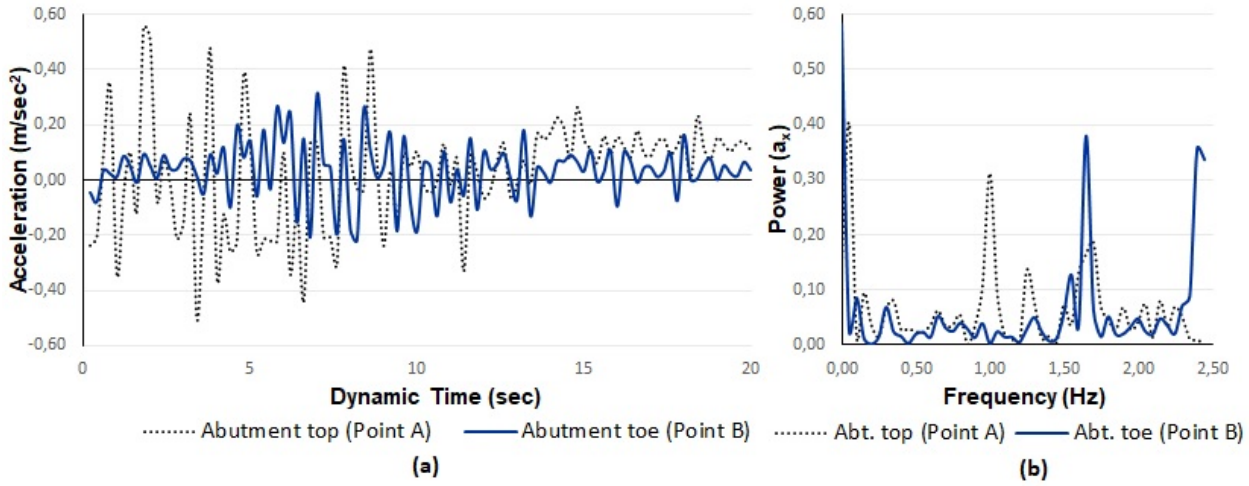

Figure 6.13: (a) Horizontal acceleration variation at abutment top and toe for 0.05g. (b) Frequency variation at abutment top and toe for 0.05g

1 Hz and as approximately 1.7 Hz for Point B. Amplification of horizontal acceleration is observed at Point A and dampening is observed at point B. Resonance behaviours depends upon input frequency, eigen-frequency and height of the point in consideration. The frequency spectrum shown in Figure 6.13 (b) indicates occurrence of resonance condition for point A because in this combination of input frequency and eigen frequency, analytical calculation of eigen frequency with considered value of shear wave velocity is 1 Hz. Nature of the input wave shows peak acceleration between 5 and 10 seconds and point B shows similar pattern. But point A shows maximum acceleration values during first five seconds of vibration indicating significant dynamic changes immediately after application of vibration. This behaviour is due to the geometry of the model and interaction between two types of HS small models, as the reinforced section is placed in top of the backfill soil without any additional support.

Acceleration time history for 0.1g amplitude input vibration for point A and B is shown in Figure 6.14. For 0.1g, dampening of horizontal acceleration at both points A and B is observed. This is because frequency is relatively uniformly distributed across the time history for this amplitude. It is also observed that the high resonance condition in the first five seconds as noted in 0.05g acceleration time history shown in Figure 6.13 (a), is non-existent for this amplitude. The wave-forms shown in Figure 6.14 represent dampened form of the input wave without resonance. Point A is less affected by the input vibration in this case in comparison to 0.05g amplitude. Frequency spectrum shown in Figure 6.14 (b) indicates that there is no particular dom-

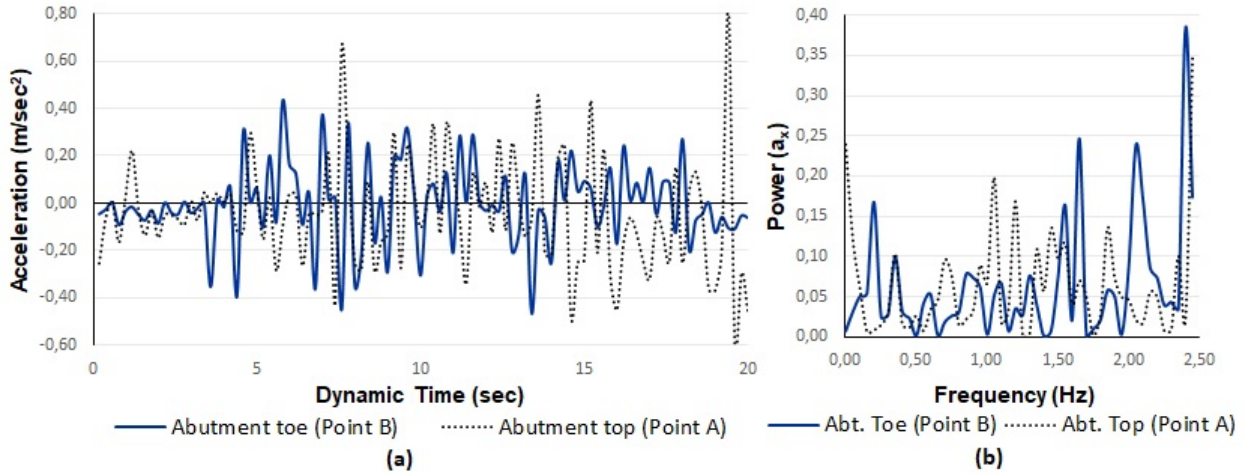

Figure 6.14: (a) Horizontal acceleration variation at abutment top and toe for 0.1g. (b) Frequency variation at abutment top and toe for 0.1g

inant frequency for the resulting curves and especially 1 Hz region is observed to have lower dominance over the time history. This is the reason behind no resonance condition as 1 Hz is the analytically calculated eigen-frequency.

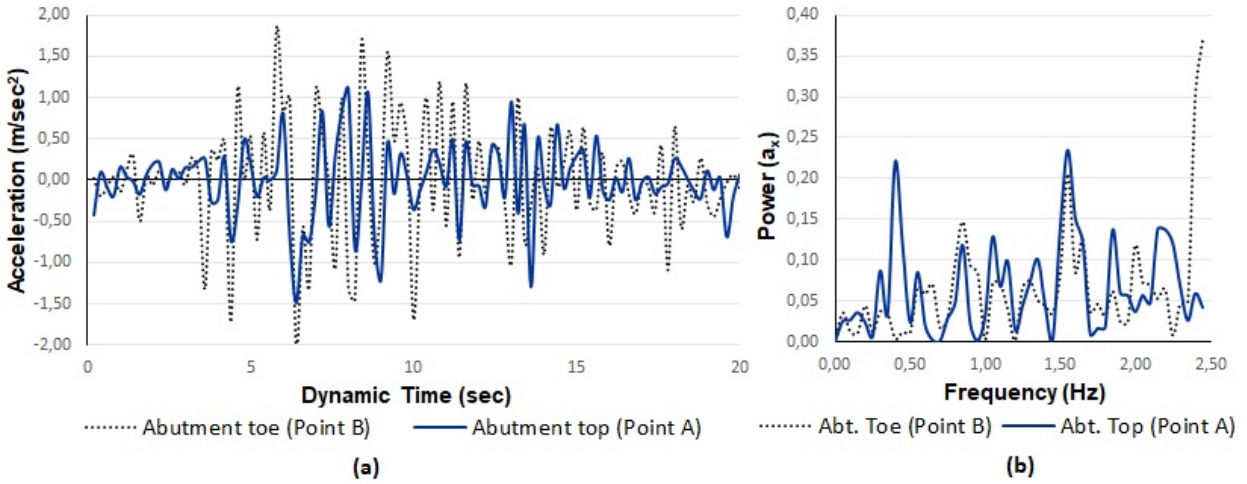

Figure 6.15: (a) Horizontal acceleration variation at abutment top and toe for 0.5g. (b) Frequency variation at abutment top and toe for 0.5g

Horizontal acceleration time history and frequency spectrum for 0.5g amplitude input vibration is shown in Figure 6.15. Most peculiar observation of the wave-form shown in Figure 6.15 (a) is that abutment top has lower resultant horizontal acceleration with time relative to point B - which is opposite to what is observed in 0.05g and 0.1g amplitude cases shown in Figure 6.13 (a) and Figure 6.14 (a) respectively. Dampening of the original amplitude is observed for both

points A and B, but the reason behind higher dampening of resultant acceleration in point A for this input amplitude is attributed to the frequency spectrum shown in Figure 6.15 (b). It is seen that the eigen-frequency is poorly represented in the resultant frequency spectrum indicating high energy loss at this point for this amplitude. Further can be seen in Figure 6.15 (b) that 0.5 Hz and 1.7 Hz have higher dominance over the time series aiding in dampening of 1 Hz resonance condition.

The acceleration time graphs for different input amplitudes show how resultant horizontal acceleration resonates with the input vibration and also the input amplitudes where eigen-frequency shows higher dominance. For the three amplitudes considered in this case, 0.05g amplitude vibration is seen to generate the maximum resonance at point A as depicted in Figure 6.13 (a) and (b).

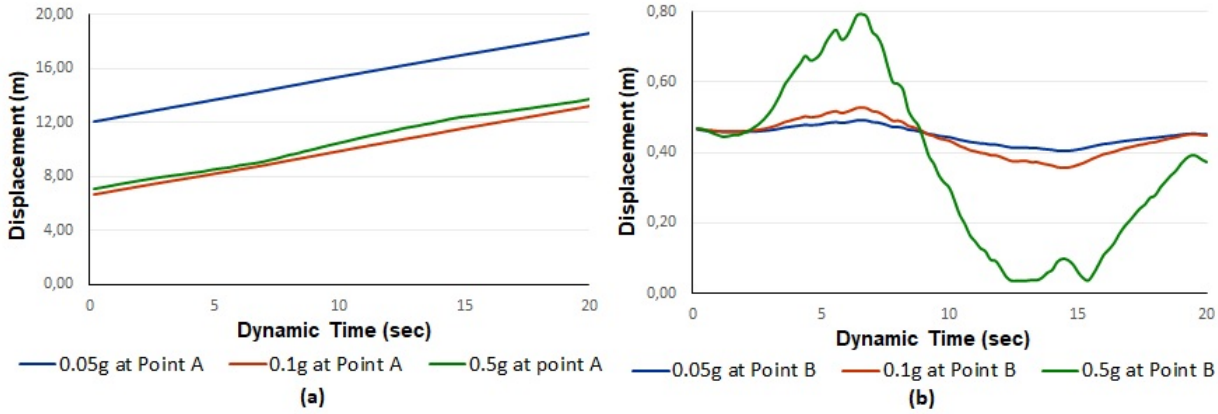

Figure 6.16: (a) Displacements at Point A for various amplitudes. (b) Displacements at Point B for various amplitudes

Displacement due to a vibration upon a structure is an indispensable part of a dynamic analysis. Displacements at Point A and B for all considered input amplitudes are shown in Figures 6.16 (a) and (b). It is known that displacements result from energy dissipation of waves. Interaction of eigen-frequency of a system with input vibration can cause either amplification or dampening of the wave energy. Energy carried by the waves is directly proportional to the frequency. This is the reason behind highest displacement occurring at the condition of highest resonance of 0.05g input amplitude, as shown in Figure 6.13 (a) and Figure 6.16 (a).

It is noticeable from Figure 6.16 (a) that, point A shows maximum displacement at 0.05g amplitude input vibration and shows approximately equal displacements for 0.1g and 0.5g input amplitudes. From Figure 6.16 (b), it is observed that Point B suffers more than ten times lower

deformation in comparison to point A. Variation of displacement is not linear in this case but all three input amplitudes show a displacement of 0.45 meters at ten seconds in the time series for point B (Figure 6.16 (b)). Contrary to point A, point B shows maximum displacement with 0.5g input but shows high fluctuations indicating the influence of depth and geometry along with input and eigen-frequency in motion of ground under vibration. Further, it is reinstated that the need of reinforcement or support for soil at point A is self evident according to the displacement results and is incorporated in next sub-section with added geogrids.

All input frequencies for point A and B are shown in a Fourier power spectrum shown in Figure 6.17 (a) and (b). One of the peculiar observations of the representation is the change of dominant frequency from 1 Hz in Point A to 1.7 Hz in point B for same amplitude input vibration. It can be seen that all three input amplitudes dominate different sections of the time series and the resonance or damping shows direct relevance in the respective displacement.

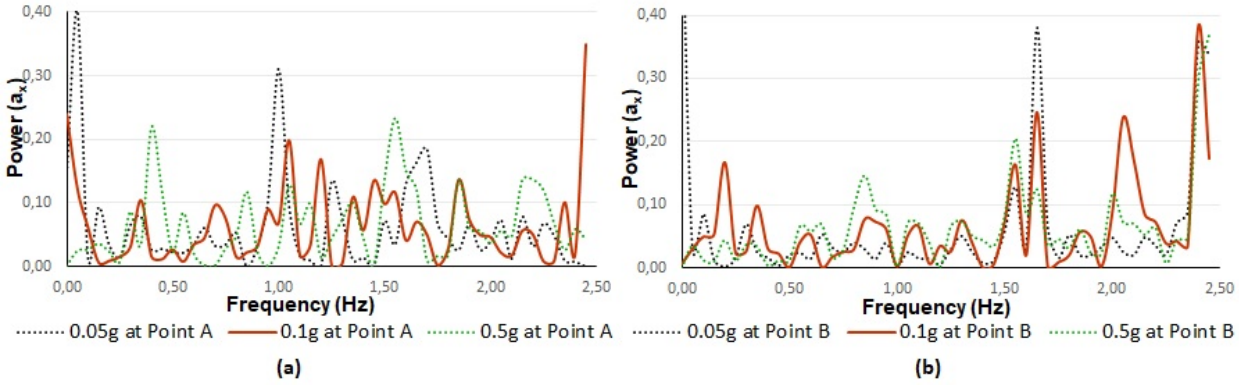

Figure 6.17: (a) Frequencies at Point A for various amplitudes. (b) Frequencies at Point B for various amplitudes

It is concluded from the analysis performed with the dynamic model without geogrids, that behaviour of soil with applied vibration under the model conditions considered - behaves according to its eigen-frequency and geometry. Point A is found to be of peculiar interest, considering its response to different input amplitudes. Behaviour of point A is hence chosen for comparison for dynamic analysis with geogrids in the following sub-section.

6.4.2 Dynamic Abutment Model with Geogrids

Boundary conditions considered for this analysis is according to Figure 6.12 and soil models are HS small model with parameters mentioned in Table 6.3. Behaviour of reinforced section

of the model when geogrid is added and its interaction with HS soil model is the main area of observation of this analysis. Comparison of data are made for point A with 0.5g PGA input vibration used previously in the context without geogrids (see Figure 6.11), as it was found to be critical in the preceding analysis.

Length of geogrid used for the analysis is according to the limit state design (i.e. 3.6 meters) and no external loads are considered for this analysis assuming that the earthquake occurs at the time when no traffic loads occur. The assumption is made for simplicity in calculation and analysis by reducing the number and types of loads and elements involved in the finite element analysis. The model consists of two types of HS small soil elements as mentioned in Table 6.3 and the same type of geogrid is used as in the static analysis with '$EA_1 = EA_2 = 1000$ kN/m'. Vertical spacing of the reinforcements is 0.4 meters as per Figure 3.5 and top vertical spacing is 0.2 meters as per calculations made in limit equilibrium design Chapter 3. Since material for embedding the geogrid is omitted from this model considering simplicity in calculation, an extra length of 0.2 meters geogrid is protruded out from the abutment for resembling the facing conditions. Interfaces are added along top and bottom of the geogrids as per the assumption that it simulates pullout resistance property. Interface strength between the reinforced soil and geogrid is '$R_{inter} = 0.8$'. A zoomed in selected view of the reinforced section with added geogrids for the dynamic analysis is shown in Figure 6.18.

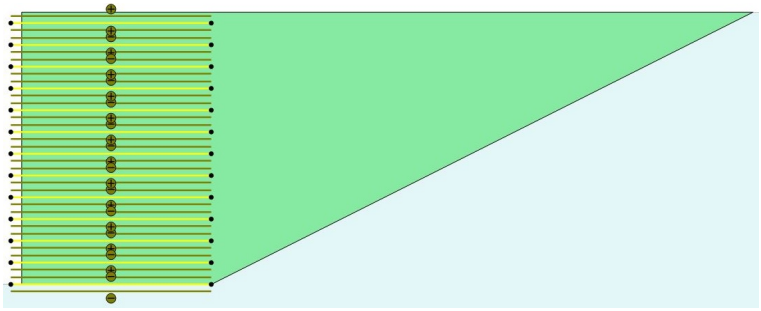

Figure 6.18: Selected view of the reinforced section with added geogrids for dynamic analysis (in PLAXIS 2D)

Stages involved in the calculation are similar to previously followed practice where an equilibrium plastic phase with all elements activated is included between the initial and dynamic phase. A medium mesh is chosen for the calculations. A vertically fixed base with free field lateral boundaries are applied and a prescribed displacement of 0.5 meters is given at the base. A dynamic acceleration time history of 0.5g PGA used previously, is applied along the base in the

dynamic phase. Deformed mesh after calculation is shown in Figure 6.19.

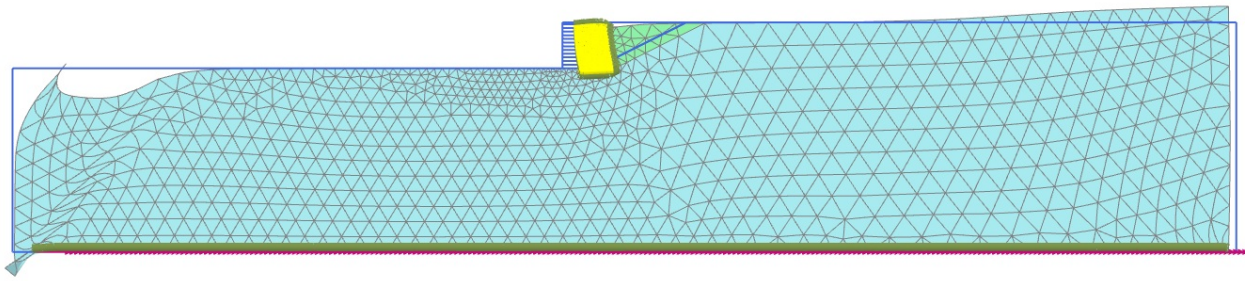

Figure 6.19: Deformed mesh after dynamic calculation involving HS small model and geogrids (in PLAXIS 2D)

It should be noted that a prescribed static horizontal displacement of 0.5 meters is applied at the equilibrium phase and the strain is not reset to zero for dynamic calculations. So the uniform dislocation of the abutment up to 0.5 meters as observed in Figure 6.19 is not a consequence of the 0.5 PGA acceleration applied at the base. It can however be stated from initial observation that the bottom of the abutment suffers less displacement in compared to top of the abutment. It should also be noted that facing element is excluded and layered construction is not followed for this analysis. So, reduction of strain due to compaction at each layer is not corrected in this case. It is also observed that additional length of geogrid that was added at the top behind the spread footing after observation of the static numerical analysis in Chapter 4, is not present in this case. Excessive settlement at the previously extra reinforced region emphasizes the importance of the added reinforcements.

Response of the lateral free field boundaries in dynamic context can be observed in Figure 6.19. Left boundary shows excessive deformation as a result of combined static displacement and dynamic acceleration. Right lateral boundary only bulges at the surface because the static displacement is applied along positive X-axis direction. The displacement of the fixed base matters exceedingly for dynamic ground movement. It can be physically compared to movement of the bed rock creating a crest/fault - where the upper soil sinks with further vibration.

The performance of the abutment model with geogrid is compared with results of abutment without geogrid at point A, which is the top front corner of the abutment. Points selected for calculations are same as for dynamic analysis without geogrid as shown in Figure 6.12. Acceleration time history, displacement and frequency power spectrum for point A is compared with the case of dynamic model without geogrids, for analyzing material model and wave property

interaction - in this dynamic assessment. Points B and C as mentioned in Figure 6.12 are omitted from comparison in this case as they are less critical in terms of stability and much is already compared about them in previous sub-sections.

Figure 6.20 compares horizontal acceleration time history for 'point A' with and without geogrids for a PGA of 0.5g. An increase in amplitude of the waves for model with geogrids is observed. The wave form resembles the original wave geometry of the input wave shown in Figure 6.11, which indicates that less dampening is observed when geogrids are used in the model. This suggests that eigen-frequency of the system has changed and since the geometry remains unchanged, it indicates that use of geogrids has altered the shear wave velocity of the system. From a more general perspective, it can also be stated that a very high displacement is observed at point A in case where geogrids weren't used. When geogrids are used in this case, the amplitude difference represents the energy difference in the system that is not converted to displacement in this case.

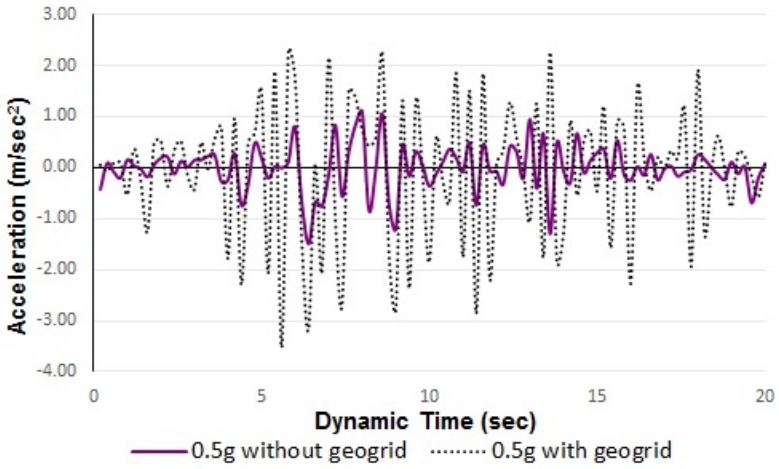

Figure 6.20: Horizontal acceleration with dynamic time for models with and without geogrids under 0.5g PGA

Relationship between displacement and dynamic time is established in Figure 6.21. Displacements with the use of geogrids are almost minuscule in comparison to the case without geogrids, but still are significant from a practical perspective and can be reduced further with the use of additional geogrids and layered construction.

It can be further observed in Figure 6.21 that contrary to the case without geogrid, displacement does not increase with dynamic time when geogrids are used. This is a good substantiation for significance of the reinforced soil structure in a dynamic situation. Nature of displacement

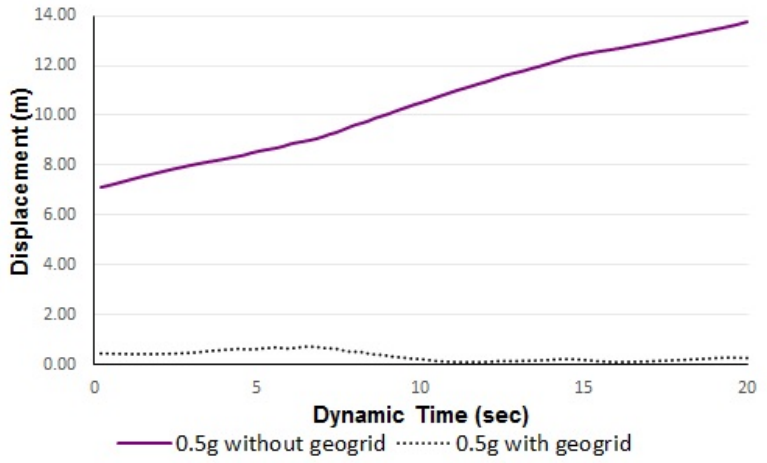

Figure 6.21: Total displacement with dynamic time for models with and without geogrids under 0.5g PGA

curve for the case with geogrid shows a decrease in displacement after 10 seconds which indicates development of strain and grip during the time segment like in the case of static strength gain due to small strain accumulation in geogrids.

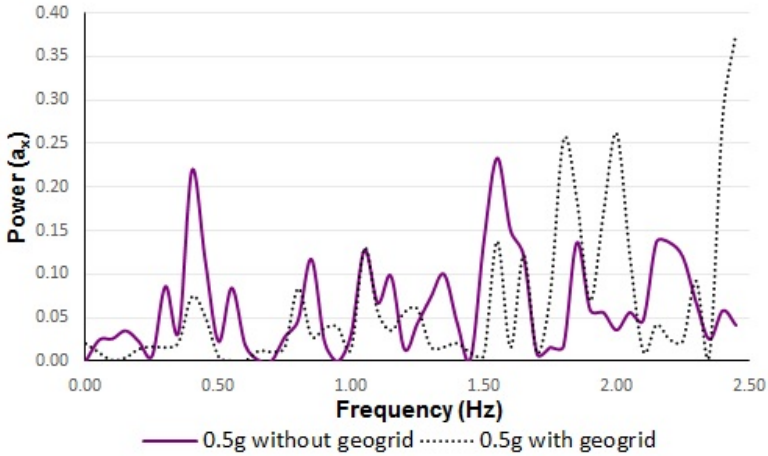

Figure 6.22: Frequency power spectrum for models with and without geogrids under 0.5g PGA

Frequency and power spectrum is shown in Figure 6.22. Peculiar observation of figure 6.22 is that the dominant frequency has shifted in the incremental direction. The shift is attributed to the incremental amplitude of horizontal acceleration previously observed and adheres with the energy conservation principle (i.e. displacement is reduced with geogrids and the resulting waves have less energy loss showing more amplitude and frequency respectively). Behaviour of shear waves and eigen frequency with and without geogrids show peculiar difference in relation to each other.

Chapter 7

Summary and Conclusions

Performance of a designed reinforced soil bridge abutment in static and dynamic conditions is analyzed in this thesis.

The base of this thesis is the abutment design obtained from the limit state method in Chapter 3. All successive analyses use the limit state design as a base, and studies behaviour of the abutment under varying conditions. In limit equilibrium design part of the thesis, it is seen that eccentricity of the abutment towards overturning has the minimum factor safety. This behaviour is substantiated by static numerical analysis in PLAXIS 2D, where tilt of the abutment is the most critical deformation observed. In internal stability part of the limit equilibrium design, it is found that the mode of failure for the reinforcements is pullout failure and not tensile failure. This mechanism is also substantiated in the plastic points diagram of PLAXIS 2D where pullout failure points are indicated.

With static numerical calculations using PLAXIS 2D, it is concluded that additional reinforcements are required behind the spread footing region for stability of the connecting road portion, for anchoring of the reinforced section to the reinforced soil and for overall stability of the bridge abutment. It is also seen that the maximum displacement after activation of bridge loads is 0.1018 meters, which is an important parameter for reaching that level of settlement during practical construction. It is also seen that the maximum tensile force is observed at the topmost geogrid and the value is approximately equal to what was obtained from limit state method. More importantly, shear hardening points were analysed for the modified and pre-modified design and a reversal of shear hardening pattern was observed, which is very significant in substantiating the modified design. Further, safety analysis provides a failure mechanism for the

modified design and it is observed that the failure occurs along the shear hardening points.

In the pseudostatic design portion, internal and external stability are analysed again using Mononobe-Okabe method and Eurocode 8. Variation of moment and tensile force for static and pseudostatic conditions show incremental values proportional to depth but are within the safety requirements.

In the dynamic modeling analysis using PLAXIS 2D, selection of boundary conditions were done and free field boundaries were selected for the main analyses as it showed good correspondence with resonance condition of input frequency and eigen-frequency.

The dynamic analysis is performed with a real time history of 20 seconds of an earthquake in form of acceleration scaled to different PGAs (0.05g, 0.1g, 0.5g). A prescribed displacement of 0.5 m is applied in the X - direction for the dynamic calculation, and this scales the applied acceleration by 0.5. Acceleration, displacement and frequency results obtained for the case without geogrid are analysed for varying PGAs. Analysis including the geogrids show significant improvement in displacement and stability of the simplified abutment model. Dominance of frequency range and amplification/dampening of resultant waves at different conditions indicate the change in overall eigen-frequency of the system and shear velocity with use of geogrids. Variance of frequency dominance and its effect in stability of the reinforced soil bridge abutment show direct relevance with resonance of eigen-frequency and input frequency.

Chapter 8

Recommendation and Further Works

Results from static analysis indicate that the shear hardening points change drastically with additional reinforcements at connecting road section. It should be further studied how this behaviour is promulgated in other soil and loading conditions. Since this thesis deals with a particular case of a designed reinforced soil bridge abutment, different conditions of load and material should be analysed for verifying the results.

Results from dynamic analysis indicate change in shear wave propagation behaviour of the abutment system with the use of geogrids. Further research from the perspective of change in shear wave propagation behaviour with use of geogrids is also recommended from the analyses of this thesis.

Bibliography

AASHTO (2007). *AASHTO LRFD Bridge Design Specifications - SI Units (4th Edition)*. American Association of State Highway and Transportation Officials (AASHTO).

Anderson, P. L., Gladstone, R. A., and Withiam, J. L. (2010). Coherent gravity: The correct design method for steel-reinforced mse walls. In *Earth Retention Conference 3*, pages 512–521. Reston, VA: American Society of Civil Engineers.

ASTMD5321 (2019). In *Standard Test Method for Determining the Shear Strength of Soil-Geosynthetic and Geosynthetic-Geosynthetic Interfaces by Direct Shear*. ASTM International. https://compass.astm.org/download/D5321D5321M.2094.pdf.

ASTMD6706 (2013). In *Standard Test Method for Measuring Geosynthetic Pullout Resistance in Soil*. ASTM International. https://compass.astm.org/download/D6706.30872.pdf.

Atkinson, J. and Sallfors, G. (1991). Experimental determination of soil properties. In *Proc. 10th ECSMFE, 3, 915–956*.

Au-Yeung, Y. and Ho, K. (1995). Geo report no. 45. In *GEO Technical Note No. TN 1/94*. Hong Kong Government.

Bathurst, R. J. and Allen, T. M. (2014). Performance of an 11 m high block-faced geogrid wall designed using the k -stiffness method. *Canadian Geotechnical Journal*, 51(1):16–29.

Bathurst, R. J. and Allen, T. M. (2018). Application of the simplified stiffness method to design of reinforced soil walls. *Journal of Geotechnical and Geoenvironmental Engineering*, 144(5):16–29.

Bathurst, R. J., Allen, T. M., and Walters, D. L. (2005). Reinforcement loads in geosynthetic

walls and the case for a new working stress design method. *Geotextiles and Geomembranes*, 23(4):287–322. https://doi.org/10.1016/j.geotexmem.2005.01.002.

Benz, T. (2006). Ph.D. Thesis . Small-strain stiffness of soils and its numerical consequences, Institut für Geotechnik, Universität Stuttgart.,.

Berg, R., Christopher, B., and Samtani, N. (2001). Mechanically stabilized earth walls and reinforced soil slopes design and construction guidelines. *U. S. Department of Transportation, Federal Highway Administration*, page chapter 6.

Brinkgreve, R., Kappert, M., and Bonnier, P. (2007). Hysteretic damping in a small-strain stiffness model. *Numerical Models in Geomechanics – NUMOG X – Pande and Pietruszczak (eds)*, page p.285.

Chopra, A. (2012). Dynamics of structures : theory and applications to earthquake engineering. In *Prentice-Hall international series in civil engineering and engineering mechanics*. Prentice Hall.

Christopher, B. R., Gill, S. A., Giroud, J. P., Juran, I., Mitchell, J. K., Schlosser, F., and Dunncliff, J. (1990). Reinforced soil structures - design and construction guidelines. *FHWA-RD-89-043*, Vol. 1(1):p.285.

Craig, R. F. (2004). Reinforced soil. In *Craig's Soil Mechanics, seventh edition*, pages 217–226. Chapman and Hall.

Dobie, M. J. D. (2015). Design of reinforced soil structures using a two-part wedge mechanism based on aashto/lrfd. *Geosynthetics*, 2015 issue:1–10.

Dobry, R. and Vucetic, M. (1987). Dynamic properties and seismic response of soft clay deposits. *International Symposium on Geotechnical Engineering of Soft Soils, Mexico City,*, 2:51–87.

Duncan, J. (1996). State of the art: Limit equilibrium and finite-element analysis of slopes. *Journal of Geotechnical Engineering*, 122(7):577–596.

Elias, V., Christopher, B., and Berg, B. (2001). Mechanically stabilized earth walls and reinforced soil slopes design and construction guidelines. *FHWA-NHI-00-043*, pages 15–17.

Fannin, R. and Hermann, S. (1990). Performance data for a sloped reinforced soil wall. *Canadian Geotechnical Journal*, 27:676–686.

Geotechnical Division NTNU (2016). Theoretical Soil Mechanics. Department of Civil and Environmental Engineering, Geotechnical Division, NTNU.

Gofar, N. (2008). Geosynthetics reinforced retaining structures. In *Ground Improvement and Stabilization*, pages 106–132. Penerbit Universiti Teknologi.

Gray, D. and Ohasi, H. (1983). Mechanics of fiber reinforcement in sand. *Journal of Geotechnical Engineering*, 109(3):335–353.

Gupta, I. and Rambabu, V. (1993). Source parameters of some significant earthquakes near koyna dam, india. *Pure and Applied Geophysics*, 140:403–413.

Hausmann, M. (1990). In *Engineering Principles of Ground Modifications*, page 632. McGraw Hill.

Holtz, R. D., christopher, B. R., and Berg, R. R. (1997). Reinforced soil retaining walls and abutments. In *Geosynthetic Engineering*, pages 289–370. BiTech Publishers Ltd.

Ingold, T. (1994). Early development in geotextiles. In *Geotextiles and Geomembranes Manual*. Elsevier Advanced Technology. https://doi.org/10.1016/C2009-0-11264-3.

Janbu, N. (1968). Slope stability computations. *Soil Mechanics and Foundation Engineering Report, The Technical University of Norway, Trondheim*.

Jones, C. (1986). Ancient structures. In *Earth Reinforcement and soil structures*, pages 6–8. Thomas Telford Publishing. https://doi.org/10.1680/erass.34891.

Koerner, R. M. (2005). Overview of geosyntheics. In *Designing with geosynthetics*. Prentice Hall.

Kramer, S. L. (1996). *Geotechnical Earthquake Engineering*. Prentice-Hall, Inc.

Lysmer, J. and Kuhlemeyer, R. L. (1969). Finite dynamic model for infinite media. *Journal of Engineering Mechanics Division*, 95:589–878.

Magar, A. (2016). Earthquake response of different types of retaining walls. In *Masters thesis in geotechnics and geohazards*, pages 1–140. NTNU.

Mannsbart, G. and Kropik, O. (1996). Nonwoven geotextile used for temporary reinforcement of a retaining structure under a railroad track. In *Geosynthetics: Applications, Design and Construction*, pages 121–124. A. A. Balkema Publishers,.

Mononobe, N. and Matsuo, S. (1929). On the determination of earth pressures during earthquakes. In *World Engineering Congress*, page p.9.

Murray, R. (1980). Fabric reinforced earth walls-development of design equations. *Ground Engineering*, 1980 issue:1–7.

NCMA (2012). *National Concrete Masonry Association*, reinforced soil segmental wall design. In *Design Manual For Segmental Retaining Wall Design(third edition, fifth print)*, pages 75–119. NCMA Puclication. https://ncma.org/resource/srw-design-manual.

NS-EN 1998-5:2004+NA:2014 (1998). EN 1998-5. Eurocode 8: Design of Structures for Earthquake Resistance Part 5: Foundations. Retaining Structures and Geotechnical Aspects.

Okabe, S. (1926). General theory of earth pressures. *Journal of the Japan Society of Civil Engineering*, Vol. 12(1).

PLAXIS (2019a). Geogrids. In *PLAXIS 2D Material Models Manual*. PLAXIS bv, Bentley Systems Incorporated. https://www.plaxis.nl.

PLAXIS (2019b). Hardening soil model with small-strain stiffness. In *PLAXIS 2D Reference Manual*. PLAXIS bv, Bentley Systems Incorporated. https://www.plaxis.nl.

PLAXIS (2019c). Safety analysis. In *PLAXIS 2D Tutorial Manual*. PLAXIS bv, Bentley Systems Incorporated. https://www.plaxis.nl.

Quinteros, V. S. (2014). Observations on the mobilization of strength in reinfoeced soil structures. In *Masers Thesis*, pages 5–80. The University of British Columbia.

Santos, J. A. and Correia, A. G. (2001). Reference threshold shear strain of soil - its application to obtain a unique strain-dependent shear modulus curve for soil. In *15^{th} International Conference on Soil Mechanics and Geotechnical Engineering, Istanbul, Turkey*, pages 267–270. Volume 1.

Schlosser, F. and Long, N. T. (1974). Recent results in french research on reinforced earth. In *ASCE Journal of Construction Division 100(C03)*, pages 223–237. ASCE.

Seed, H. B. and Idriss, I. M. (1970). Soil moduli and damping factors for dynamic response analyses. *EERC Report*, 70(10).

Seed, H. B. and Whitman, R. V. (1970). Design of earth retaining structures for dynamic loads. In *ASCE Specialty Conference on Lateral Stresses in the Ground and Design of Earth Retaining Structures*, pages 103–147. ASCE.

Steedman, R. S. and Zeng, X. (1990). The seismic response of waterfront retaining walls. In *ASCE Specialty Conference on Design and Performance of Earth Retaining Structures, Special Technical Publication 25*, pages 872–886. Cornell University, Ithaca, New York.

Steward, J., Williamson, R., and Mohney, J. (1977). *Guidelines for use of fabrics in construction and maintenance of low-volume roads*, USDA, Forest Service, Portland.

Tatsuoka, F., Uchimura, T., Tateyama, M., and Koseki, J. (1997). Geosynthetic reinforcement soil retaining walls as important permanent structures. In *Mechanically Stabilized Backfill*, pages 3–24. A. A. Balkema Publishers, Rotterdam, The Netherlands.

Walters, D. L., Allen, T. M., and Bathurst, R. J. (2002). Conversion of geosynthetic strain to load using reinforcement stiffness. *Geosynthetics International*, 9(5-6):483–523. https://doi.org/10.1680/gein.9.0226.

Whitman, R. V. (1990). Seismic design behavior of gravity retaining walls. In *ASCE Specialty Conference on Design and Performance of Earth Retaining Structures, Geotechnical Specialty Publication 25*, pages 817–842. ASCE, New York.

Won, G., Hull, T., and De Ambrosis, L. (1996). Performance of a geosynthetic segmental block wall structure to support bridge abutments. In *Earth Reinforcement*, pages 5543–548. A. A. Balkema Publishers,.

Wu, J. T. H., Ketchart, K., and Adams, M. T. (2001). *GRS Bridge Piers and Abutments.* In *Report FHWA-RD-00-038*, page 136. FHWA, U.S. DOT.

Wu, J. T. H., Lee, K. Z. Z., Helwany, S. B., and Ketchart, K. (2006). In *Design and Construction Guidelines for Geosynthetic-Reinforced Soil Bridge Abutments with a Flexible Facing*, pages 9–10. The National Academies Press. http://nap.edu/13936.

Xu, P. and Hatami, K. (2019). Sliding stability and lateral displacement analysis of reinforced soil retaining walls. *Geotextiles and Geomembranes*, 2019 issue:1–10. https://doi.org/10.1016/j.geotexmem.2019.03.004.

Zarrabi-Kashani, K. (1979). Sliding of gravity retaining wall during earthquakes considering vertical accelerations and changing inclination of failure surface. M.S. thesis.

Appendix A

Acronyms

MC Mohr - Coulomb

GRS Geosynthetically Reinforced Soil

CRF Creep Reduction Factor

FoS Factor of Safety

HS small Hardening Soil (including small strain)

M-O Mononobe - Okabe

PGA Peak Ground Acceleration

TH Time History

DL Dead Load

LL Live Load

FL Frictional Load

NGI Norwegian Geotechnical Institute

HS Hardening Soil

FEM Finite Element Method

Appendix B

Appendix B : Static Analysis

Table B.1: Equations used for calculating unfactored vertical forces as per Figure 3.1 and Figure 3.2

Vertical forces	Equation used
$\mathbf{V}_0$	$\gamma_r \cdot \mathrm{L}_r \cdot \mathrm{H}_t$
$\mathbf{V}_1$	$\gamma_r \cdot \mathrm{B}_b \cdot \mathrm{h}_t$
$\mathbf{V}_2$	$\gamma_c \cdot \mathrm{B}_t \cdot \mathrm{h}_t$
$\mathbf{V}_3$	$\gamma_c \cdot \mathrm{h}_b \cdot \mathrm{B}$
$\mathbf{V}_{sa}$	$\gamma_b \cdot (\mathrm{B}_t + \mathrm{B}_b) \cdot \mathrm{h}_{sa}$
$\mathbf{V}_{sb}$	$\gamma_b \cdot (\mathrm{L}_r$ - B - C) $\cdot \mathrm{h}_{sb}$

Table B.2: Equations used for calculating moment arns for vertical forces as per Figure 3.1 and Figure 3.2

Vertical Forces	Moment arm about T	Moment arm about B
$\mathbf{V}_0$	-	L_r / 2
$\mathbf{V}_1$	$\mathrm{B}_t + \mathrm{B}_f + \mathrm{B}_b/2$	$\mathrm{B}_t + \mathrm{B}_f + \mathrm{B}_b/2 + \mathrm{C}$
$\mathbf{V}_2$	B_t / 2 + B_f	B_t / 2 + B_f + C
$\mathbf{V}_3$	B/2	B/2 + C
$\mathbf{V}_{sa}$	$\mathrm{B}_f + (\mathrm{B}_t + \mathrm{B}_b)/2$	$\mathrm{B}_f + (\mathrm{B}_t + \mathrm{B}_b)/2 + \mathrm{C}$
$\mathbf{V}_{sb}$	(L_r - B - C)/2 + B	(L_r - B - C)/2 + B + C

Table B.3: Equations used for calculating unfactored horizontal forces as per Figure 3.1 and Figure 3.2

Hoizontal Forces	Equation used
$\mathbf{F}_0$	$0.5 \cdot K_{ab} \cdot \gamma_b \cdot H_t{}^2$
$\mathbf{F}_1$	$0.5 \cdot K_{ar} \cdot \gamma_r \cdot h \cdot V_{sb}$
$\mathbf{F}_2$	$K_{ab} \cdot \gamma_r \cdot H_t \cdot h$
$\mathbf{F}_3$	pre defined
$\mathbf{F}_{sa}$	$K_{ar} \cdot \gamma_b \cdot h \cdot h_{sa}$
$\mathbf{F}_{sb}$	$K_{ab} \cdot \gamma_b \cdot H_t \cdot h_{sb}$
$\mathbf{F}_t$	$F_1 + F_3 + F_{sa}$

Table B.4: Equations used for calculating moment arms for horizontal forces forces as per Figure 3.1 and Figure 3.2

Horizontal Forces	Moment arm about T	Moment arm about B
$\mathbf{F}_0$	-	H_t / 3
$\mathbf{F}_1$	h/3	H_t + (h/3)
$\mathbf{F}_2$	-	H_t /2
$\mathbf{F}_3$	h_b	$h_b + H_t$
$\mathbf{F}_{sa}$	h/2	$h/2 + H_t$
$\mathbf{F}_{sb}$	-	$H_t/2$
$\mathbf{F}_t$	case-wise	case-wise

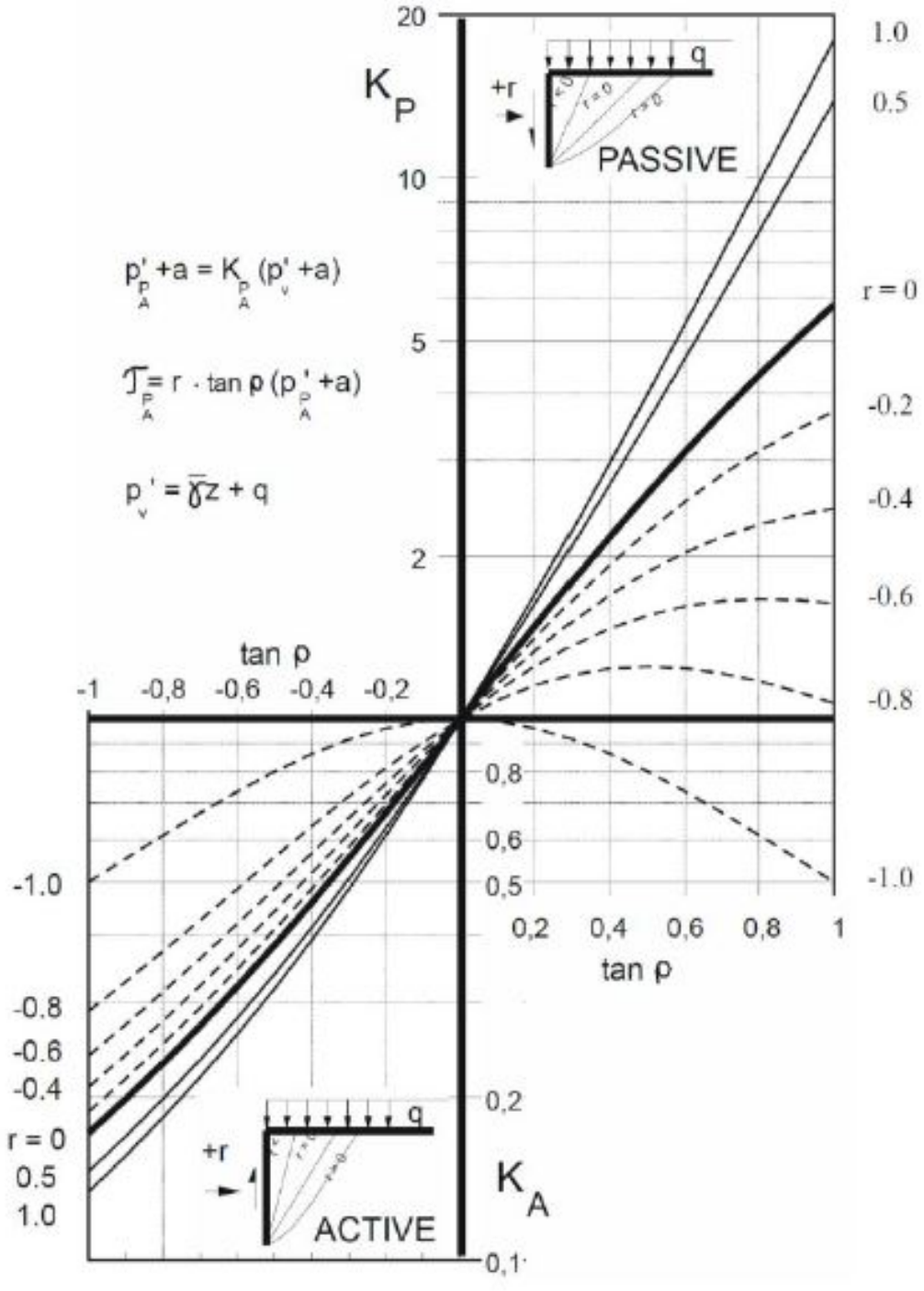

Figure B.1: Earth Pressure coefficients for effective stress analysis (Geotechnical Division NTNU (2016))

Appendix C

Appendix C : Seismic Analysis

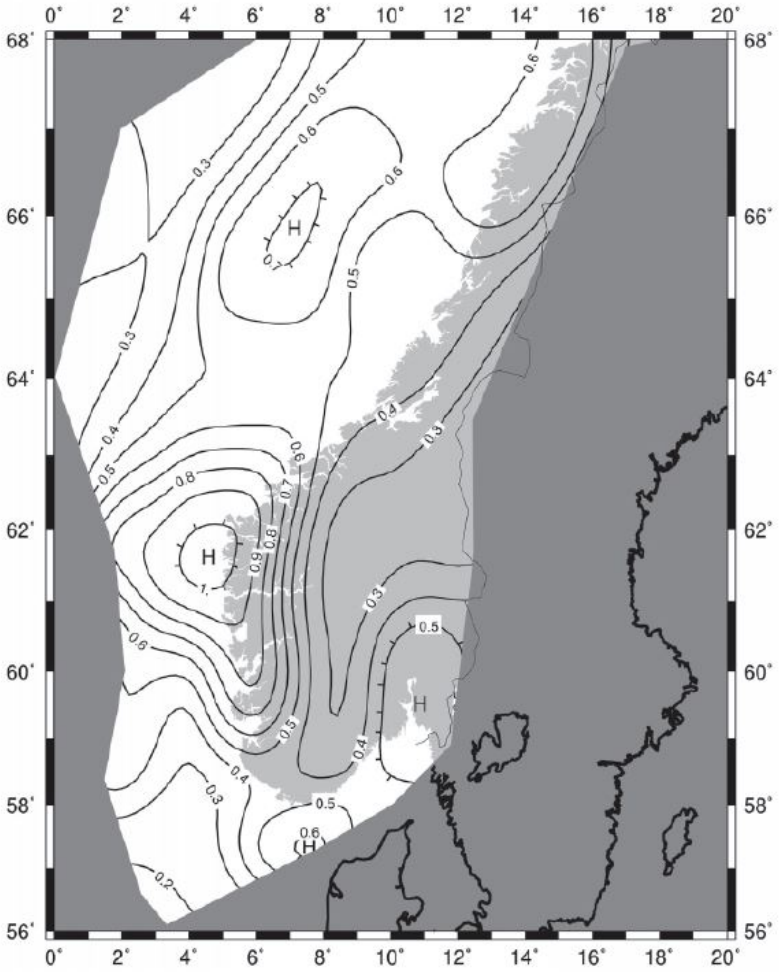

Figure C.1: Seismic zones for southern part of Norway (NA.3(901))

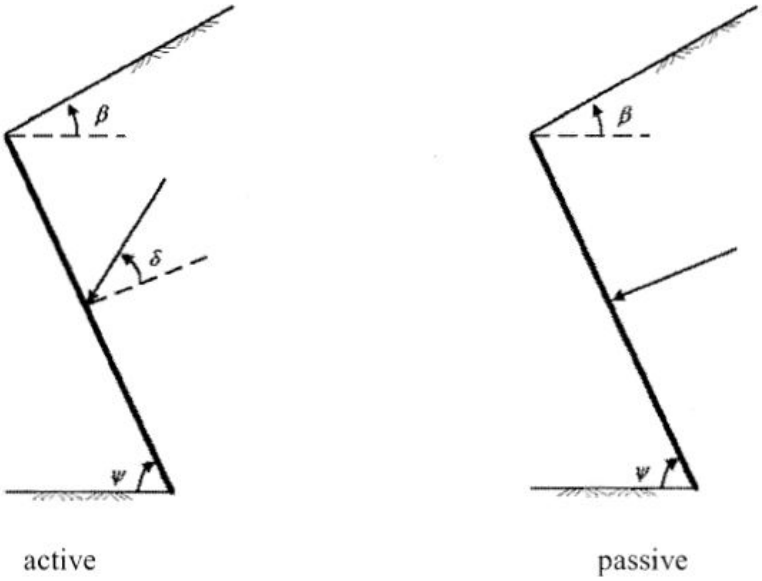

Figure C.2: Convention of angles for pseudo-static earth pressure coefficients (NS-EN 1998-5:2004+NA:2014 (1998))

Table C.1: Factor for calculating horizontal seismic coefficient (Table 7.1 EC 8-5)

Type of retaining structure	r
Free gravity walls that can accept a displacement up to $d_r = 300\ \alpha \cdot S$ (mm)	2
Free gravity walls that can accept a displacement up to $d_r = 200\ \alpha \cdot S$ (mm)	1,5
Flexural reinforced concrete walls, anchored or braced walls, reinforced concrete walls founded on vertical piles, restrained basement walls and bridge abutments	1

Table C.2: Ground types for strati-graphic profiles (Table NA.3.1 EC 8-1)

Ground type	Description of stratigraphic profile	Parameters		
		$v_{s,30}$ (m/s)	N_{SPT} (blows/30cm)	c_u (kPa)
A	Rock or other rock-like geological formation, including at most 5 m of weaker material at the surface.	> 800	–	–
B	Deposits of very dense sand, gravel, or very stiff clay, at least several tens of metres in thickness, characterised by a gradual increase of mechanical properties with depth.	360 – 800	> 50	> 250
C	Deep deposits of dense or medium-dense sand, gravel or stiff clay with thickness from several tens to many hundreds of metres.	180 – 360	15 - 50	70 - 250
D	Deposits of loose-to-medium cohesionless soil (with or without some soft cohesive layers), or of predominantly soft-to-firm cohesive soil.	< 180	< 15	< 70
E	A soil profile consisting of a surface alluvium layer with v_s values of type C or D and thickness varying between about 5 m and 20 m, underlain by stiffer material with v_s > 800 m/s.			
S_1	Deposits consisting, or containing a layer at least 10 m thick, of soft clays/silts with a high plasticity index (PI > 40) and high water content	< 100 (indicative)	–	10 - 20
S_2	Deposits of liquefiable soils, of sensitive clays, or any other soil profile not included in types A – E or S_1			

Table C.3: Amplification factors for ground types in Table C.2 (Table NA.3.3 EC 8-1)

Grunntype	S
A	1,0
B	1,25
C	1,4
D	1,6
E	1,7

Table C.4: Classification of seismic classes (Table NA.4(902) EC 8-1)

Byggverk	I	II	III	IV
Byggverk der konsekvensene av sammenbrudd er særlig store				X[1)]
Viktig infrastruktur: sykehus, brannstasjoner, redningssentraler, kraftforsyning og lignende			(X)	X
Høye bygninger, mer enn 15 etasjer		(X)	X	
Jernbanebruer [2)]			X	(X)
Veg- og gangbruer [2)]		(X)	X	(X)
Byggverk med store ansamlinger av mennesker (tribuner, kinosaler, sportshaller, kjøpesentre, forsamlingslokaler osv.)		(X)	X	
Kaier og havneanlegg		X	(X)	
Tårn, master, skorsteiner, siloer	(X)	X	(X)	
Industrianlegg		X	(X)	
Skoler og institusjonsbygg		(X)	X	
Kontorer, forretningsbygg og boligbygg		X	(X)	
Småhus, rekkehus, bygg i én etasje, mindre lagerhus osv.	X	(X)		
Landbruksbygg	(X)			
Fiskerihavner	(X)			
Kaier og fortøyningsanlegg for sport og fritid	(X)			

[1)] For byggverk der konsekvensene av sammenbrudd er særlig store, for eksempel ved atomreaktorer og lagringsanlegg for radioaktivt avfall, store dammer og marine konstruksjoner bør jordskjelvrisikoen vurderes spesielt, eventuelt basert på en risikoanalyse.

Lagertanker for flytende gass og store hydrokarbonførende rørledninger over land er behandlet i NA til NS-EN 1998-4.

[2)] Se veiledende tabell for valg av seismisk klasse for bruer i NA til NS-EN 1998-2.

Table C.5: Importance factors by seismic classes (Table NA.4(901) EC 8-1)

Seismisk klasse	Seismisk faktor γ_I
I	0,7
II	1,0
III	1,4
IV	2,0

Table C.6: Interface friction angles according to Kramer (1996)

Interface Materials		Interface Friction Angle δ
Mass concrete against:	clean sound rock	25
	clean gravel, gravel–sand mixtures, coarse sand	29–31
	clean fine to medium sand, silty medium to coarse sand, silty or clayey gravel	24–29
	clean fine sand, silty or clayey fine to medium sand	19–24
	fine sandy silt, nonplastic silt	17–19
Formed concrete against:	medium-stiff and stiff clay and silty clay	17–19
	clean gravel, gravel–sand mixture, well-graded rock fill with spalls	22–26
	clean sand, silty sand–gravel mixture, single-size hard rock fill	17–22
Steel sheet piles against:	silty sand, gravel, or sand mixed with silt or clay	17
	fine sandy silt, nonplastic silt	
	clean gravel, gravel–sand mixture, well-graded rock fill with spalls	14 22
	clean sand, silty sand–gravel mixture, single-size hard rock fill	17 14
	silty sand, gravel, or sand mixed with silt or clay	11
	fine sandy silt, nonplastic silt	

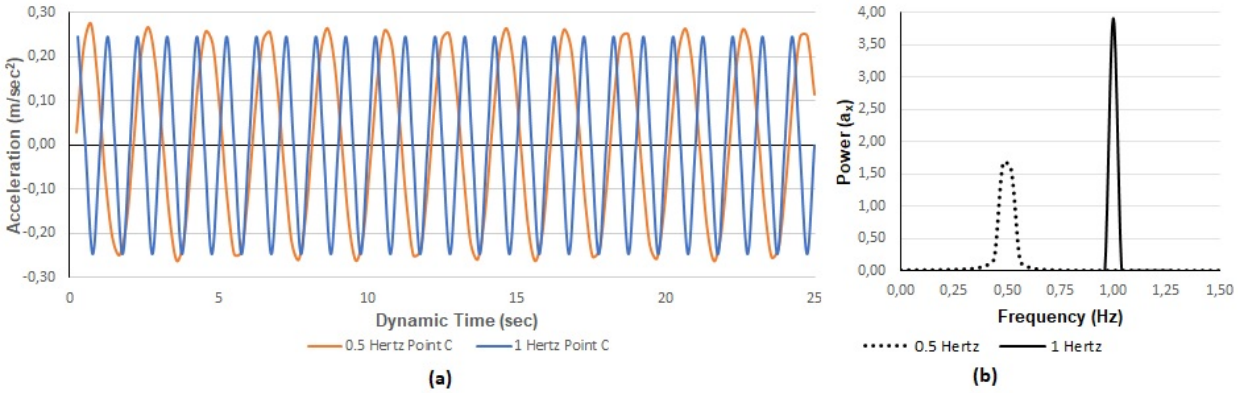

Figure C.3: (a) Horizontal acceleration at point 'C' with 0.5 and 1 Hertz using viscous lateral boundaries (b)Frequency dominance representation at 0.5 and 1 Hertz

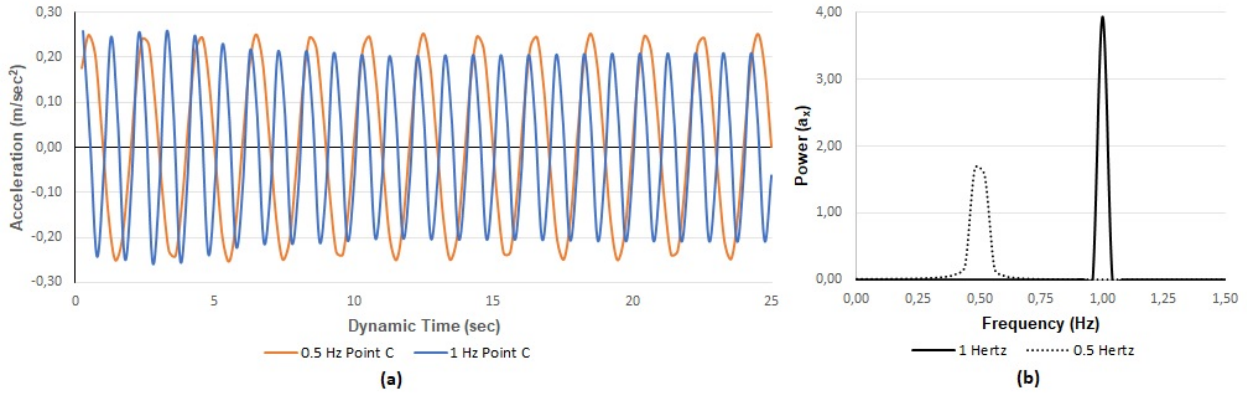

Figure C.4: (a) Horizontal acceleration at point 'C' with 0.5 and 1 Hertz using free field boundaries (b)Frequency dominance representation at 0.5 and 1 Hertz

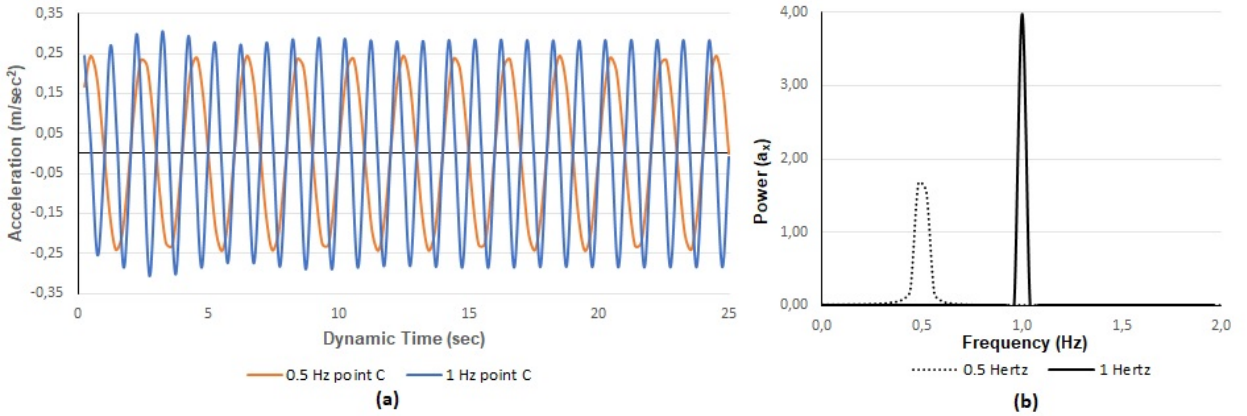

Figure C.5: (a) Horizontal acceleration at point 'C' with 0.5 and 1 Hertz using laterally loaded - open boundaries (b)Frequency dominance representation at 0.5 and 1 Hertz

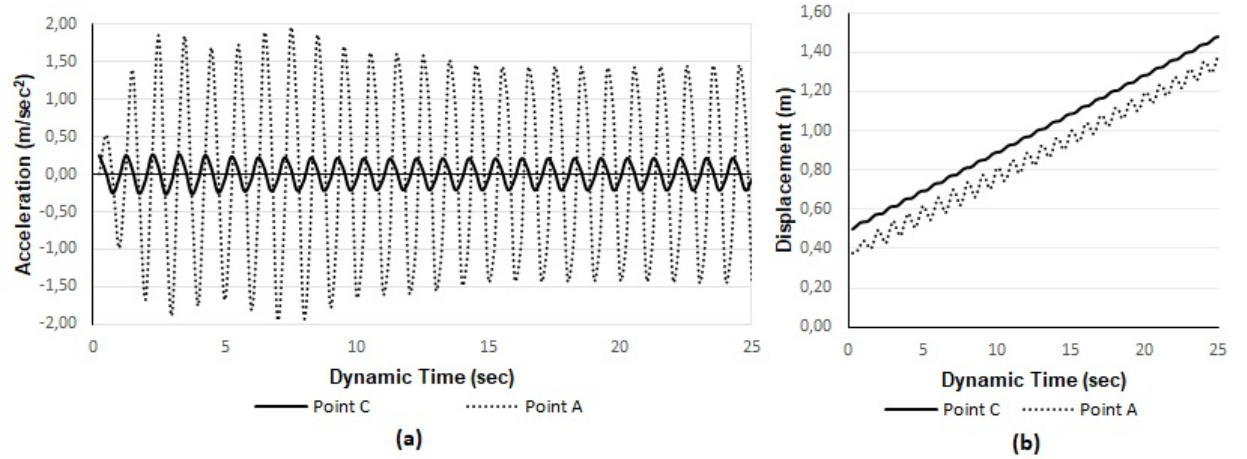

Figure C.6: (a) Horizontal acceleration of points 'A' and 'C' at 1 Hertz with laterally loaded - free field boundaries (b) Total displacement of points 'A' and 'C' at 1 Hertz with laterally loaded - free field boundaries

Parasmani Tripathi

Geosynthetically Reinforced Soil Bridge Abutment

NTNU
Norwegian University of
Science and Technology